

# Mechanics and Dynamics of Micro-cutting Process

by

Xiaoliang Jin

B.Sc., Beihang University, China, 2004

M.A.Sc., Beihang University, China, 2007

A THESIS SUBMITTED IN PARTIAL FULFILLMENT OF  
THE REQUIREMENTS FOR THE DEGREE OF

DOCTOR OF PHILOSOPHY

in

THE FACULTY OF GRADUATE STUDIES

(Mechanical Engineering)

THE UNIVERSITY OF BRITISH COLUMBIA

(Vancouver)

September 2012

© Xiaoliang Jin, 2012

# Abstract

Micro-cutting operations are used to manufacture miniature parts in biomedical, optics, electronics, and sensors industry. Compared to chemical manufacturing processes, micro-cutting has the advantage of producing three-dimensional features with a broad range of materials. Tool geometries and cutting conditions need to be properly selected to achieve desired surface finish and avoid premature wear or breakage of the fragile micro-tools. The mechanics and dynamics of micro-cutting have to be modeled in order to predict the process behavior and plan the operations ahead of costly physical trials.

The chip thickness is comparable to the tool edge radius in micro-cutting, which brings strong size effect to the prediction of cutting force. A generalized analytical model based on slip-line field theory is proposed to predict the stress distribution and cutting force with round tool edge effect. Plastic deformation of workpiece material is modeled considering strain hardening, strain-rate and temperature effects on the flow stress. A numerical model is developed to simulate chip formation and cutting force using finite element method. The simulation results obtained from the numerical and analytical models are compared against experimental measurements to evaluate their predictive accuracy.

The cutting force coefficients are modeled as functions of tool edge radius and uncut chip thickness from a series of slip-line field and finite element simulations. The identified cutting force coefficients are used to simulate micro-milling forces considering the actual tool trajectory, radial tool run-out and the dynamometer dynamics. Micro-milling forces which have sub-Newton amplitude are predicted directly from material constitutive model with experimental proof.

A specially devised piezo-actuator mechanism is developed to identify the frequency response function of the micro-mill up to 120 kHz. The process damping coefficient in the ploughing region is identified from the finite element simulations. Dynamic micro-milling

force with the velocity dependent process damping mechanism is modeled, and the chatter stability is predicted in frequency domain. Chatter tests are conducted to experimentally validate the dynamic model of micro-milling.

The proposed mechanics and dynamic models can be used to simulate micro-cutting operations with various workpiece materials and tool geometries, and provide guidance for micro-cutting planners to select optimum cutting conditions.

# Preface

The papers published or submitted for publications from this thesis originated from the author's Ph.D. research conducted under the supervision of Dr. Yusuf Altintas. The relative contributions of the authors in the publications are clarified in this section.

The content of Chapter 3 has been published in two journal articles: 1. [Jin, X.], Altintas, Y., 2011, Slip-line Field Model of Micro-cutting Process with Round Tool Edge Effect, *Journal of Materials Processing Technology*, vol. 211, 339–355. The proposed slip-line field model of the micro-cutting process was formulated by the author. Micro-turning experiments were conducted to validate the model. 2. Altintas, Y., [Jin, X.], 2011, Mechanics of micro-milling with round edge tools, *Annals of CIRP*, 60/1, 77-80. The author of the thesis extended the slip-line field model to predict the cutting forces in micro-milling. The algorithms of calculating the exact chip thickness and using Kalman filter to compensate dynamometer distortion were based on the previous research work conducted by Dr. Altintas [67][68][69][70]. Dr. Altintas wrote the paper and the author of the thesis assisted.

A version of Chapter 4 has been published in [Jin, X.], Altintas, Y., 2011. Prediction of Micro-milling Forces with Finite Element Method. *Journal of Materials Processing Technology*, vol.212, 542-552. The author developed the finite element model to simulate the chip formation in micro-cutting. Cutting forces from finite element simulations were used to calibrate cutting force coefficient. Micro-milling tests were conducted and compared against the simulation results obtained from the proposed slip-line field and finite element models.

A version of Chapter 5 has been submitted for review. The author developed the measurement device to identify the frequency response function of micro-mill, and identified the process damping coefficient from finite element simulations. The chatter tests

were conducted by the author of the thesis. Dr. Altintas supervised the research and contributed significantly in writing the papers originated from the thesis.

# Table of Contents

Abstract.....	ii
Preface .....	iv
Table of Contents .....	vi
List of Tables.....	ix
List of Figures .....	x
Nomenclature.....	xv
Acknowledgements.....	xxiii
Dedication.....	xxiv
Chapter 1 Introduction .....	1
Chapter 2 Literature Review.....	6
2.1 Overview.....	6
2.2 Modeling of cutting mechanics.....	6
2.2.1 Mechanistic model.....	6
2.2.2 Slip-line field model .....	7
2.2.3 Finite element model .....	12
2.3 Modeling of cutting dynamics .....	14
2.3.1 Identification of FRF at tool tip .....	15
2.3.2 Identification of process damping.....	16
2.3.3 Chatter stability of micro-milling .....	18
Chapter 3 Slip-line Field Modeling of Micro-cutting Process .....	20
3.1 Overview.....	20
3.2 Slip-line field model .....	21
3.3 Determination of slip-line field geometry .....	23
3.3.1 Determination of slip-lines in the secondary shear zone .....	23
3.3.2 Determination of slip-lines in the tertiary and primary zones .....	25
3.4 Stress analysis in the primary shear zone .....	27

3.4.1	Shear strain and strain-rate .....	29
3.4.2	Temperature distribution.....	34
3.4.3	Shear flow stress and hydrostatic pressure .....	34
3.5	Identification of slip-line parameters .....	37
3.6	Prediction of cutting forces.....	39
3.6.1	Stress analysis in the secondary shear zone.....	39
3.6.2	Stress analysis in the tertiary shear zone .....	42
3.7	Experimental validation by micro-turning.....	45
3.7.1	Experimental conditions .....	45
3.7.2	Experimental comparisons.....	48
3.7.3	Simulation results and discussions .....	51
3.7.4	Summary of slip-line field model .....	54
3.8	Cutting forces prediction in micro-milling .....	55
3.8.1	Cutting force coefficient estimation from slip-line field model .....	56
3.8.2	Prediction of micro-milling forces.....	57
3.8.3	Experimental validation in micro-milling.....	58
3.9	Conclusion .....	64
Chapter 4	Finite Element Modeling of Micro-cutting Process.....	65
4.1	Overview.....	65
4.2	FE modeling of orthogonal micro-cutting .....	66
4.2.1	Material properties.....	67
4.2.2	Tool-workpiece contact .....	68
4.2.3	Meshing strategy and chip formation .....	68
4.2.4	Determination of material separation point .....	70
4.3	Prediction of cutting forces with FE model .....	72
4.4	Prediction of micro-milling forces with FE model.....	78
4.5	Microstructure effect on micro-cutting process.....	82
4.6	Conclusion .....	86

Chapter 5	Dynamic Modeling of Micro-milling Process .....	88
5.1	Overview.....	88
5.2	Dynamic cutting force model in micro-milling process .....	88
5.3	Identification of cutting force and process damping coefficients.....	91
5.3.1	Identification of cutting force coefficients.....	91
5.3.2	Identification of process damping coefficients.....	93
5.4	Prediction of chatter stability in micro-milling.....	100
5.5	Experimental validation for micro-milling chatter .....	103
5.5.1	Identification of FRF at micro-mill tip .....	104
5.5.2	Chatter stability tests.....	107
5.6	Conclusion .....	111
Chapter 6	Conclusions and Future Research Directions .....	113
6.1	Conclusions.....	113
6.2	Future research directions.....	116
	Bibliography .....	117
	Appendix A: Determination of Slip-line Geometries .....	125
	Appendix B: Derivation of Stress Distribution in Slip-line Field Model .....	126

# List of Tables

Table 3.1 Cutting conditions of micro-turning experiment. ....	46
Table 3.2 Johnson-Cook parameters for brass 260 [62]. ....	46
Table 3.3 Chip thickness measurement for carbide tool with 20 $\mu\text{m}$ edge radius. ....	47
Table 3.4 Constants for the cutting force coefficients of material brass 260 at cutting speed 25 [m/min]. Units of chip thickness and edge radius are in [mm]. ....	57
Table 3.5 Modal parameters of dynamometer in X and Y directions. ....	62
Table 4.1 Johnson-Cook parameters of brass 260 (Strain-hardening constants in the original Johnson-Cook model [62] are reduced by 20% for the specific tested material as explained in Section 3.7) ....	67
Table 4.2 Physical properties of brass 260.....	68
Table 4.3 Tool-chip contact length.....	76
Table 4.4 Variation of equivalent plastic strain, temperature and Von-Mises stress in the primary shear zone.....	76
Table 4.5 Constants for the cutting force coefficients of material brass 260 at cutting speed 25 m/min. Units of chip thickness and edge radius are in [mm]. ....	79
Table 4.6 Cutting conditions for micro-milling test.....	79
Table 4.7 Johnson-Cook parameters and cutting conditions in FE simulation.....	84
Table 4.8 Cutting condition in the FE model.....	85
Table 5.1 Cutting force coefficients in Equation (3-66) for AISI 1045 steel. ....	92
Table 5.2 Physical parameters of AISI 1045 steel and cutting condition. ....	96
Table 5.3 Modal parameters of micro-mill. ....	105
Table 5.4 Natural frequencies and mode shapes of micro-mill from FE simulation. ...	106

# List of Figures

Figure 1.1 Miniature part produced by micro-cutting operation [1].....	1
Figure 1.2 Comparison of macro-mill and micro-mill. ....	2
Figure 1.3 Material flow in orthogonal micro-cutting.....	3
Figure 1.4 Flow chart of research content. ....	4
Figure 2.1 Slip-line field model proposed by Fang and Jawahir [27]. ....	10
Figure 2.2 Slip-line field model proposed by Fang [28][29]. ....	11
Figure 2.3 Process damping force with round tool edge effect proposed by Sisson and Kegg, reproduced from [47]. ....	17
Figure 3.1 Slip-line field model of orthogonal micro-cutting process with round tool edge: primary shear zone [GJBTNEQ], secondary shear zone [BCDHJK], tertiary zone [BSAUTP]. ....	22
Figure 3.2 Slip-lines in the secondary shear zone. ....	24
Figure 3.3 Slip-lines in the primary and tertiary shear zones. ....	26
Figure 3.4 Stress-strain curve of brass 260 with different strain-rate values ( $T=20^{\circ}\text{C}$ ), obtained from the constitutive parameters identified by Johnson and Cook [61]. ....	28
Figure 3.5 Stress-strain curve of brass 260 with different temperature values ( $\dot{\epsilon}=1\text{s}^{-1}$ ), obtained from the constitutive parameters identified by Johnson and Cook [61]. ....	29
Figure 3.6 Polar coordinate setup in primary shear zone. ....	30
Figure 3.7 Velocity variation along slip-line TB. ....	31
Figure 3.8 Velocity transition along the $\alpha$ slip-lines in primary shear zone. ....	32
Figure 3.9 Calculation of hydrostatic pressure in the primary shear zone. ....	35
Figure 3.10 Identification of parameters in the slip-line field model. ....	37
Figure 3.11 Flow chart of parameter identification and cutting force prediction. ....	39
Figure 3.12 Stress analysis in the secondary shear zone. ....	40
Figure 3.13 Stress analysis in the tertiary shear zone. ....	43
Figure 3.14 (a) Setup for microturning experiment; (b) SEM image of the cutting edge. ....	45

Figure 3.15 SEM image of the material on the cutting edge. ....	47
Figure 3.16 Tangential and feed force with uncut chip thickness; predicted: simulation results when using the Johnson-Cook parameters in Table 3.2; predicted (scaled): simulation results when initial yield strength A and strain-hardening coefficient B in Table 3.2 are reduced by 20%. Cutting edge radius: 20 $\mu\text{m}$ . ....	49
Figure 3.17 Tangential and feed force with cutting speed; predicted: simulation results when using the Johnson-Cook parameters in Table 3.2; predicted (scaled): simulation results when initial yield strength A and strain-hardening coefficient B in Table 3.2 are reduced by 20%. Cutting edge radius: 20 $\mu\text{m}$ . ....	50
Figure 3.18 Cutting force with tool edge radius. (Sim: simulation results; Exp: experimental results).....	51
Figure 3.19 Strain, strain-rate, temperature, and shear flow stress along line GB. ....	52
Figure 3.20 Strain, strain-rate, temperature and shear flow stress along line NJ. ....	53
Figure 3.21 Distribution of normal and friction stress along tool-chip contact.....	54
Figure 3.22 Simulated cutting forces from slip-line field model. Material: brass 260. See Equation (3-15) and Figure 3.16 for material properties. Cutting speed = 25 m/min and tool's primary rake angle = 5 deg. Symbols represent the simulated results from slip-line field model, and the lines are the curved-fitted results. ....	57
Figure 3.23 Micro-milling process. ....	58
Figure 3.24 Set-up for micro-milling tests: Mikrotool CNC micro-machining center, Kistler 9256 mini-dynamometer, brass 260 coupon. ....	59
Figure 3.25 Two-fluted micro-mill with 200 $\mu\text{m}$ diameter and 3.7 $\mu\text{m}$ edge radius.....	59
Figure 3.26 Experimental setup to measure static radial run-out of tool.....	60
Figure 3.27 (a) The edge of first flute is aligned to the reference line, (b) Distance between the edge of second flute and the reference line.....	60
Figure 3.28 FRFs of dynamometer in X and Y directions.....	61
Figure 3.29 Slot micro-milling with 50 $\mu\text{m}$ axial depth of cut. Material: brass 260. Tool: 200 $\mu\text{m}$ diameter. Spindle speed: 20,000 [rev/min]. Feed-rate: 3 $\mu\text{m}/\text{rev}/\text{tooth}$ .....	63

Figure 3.30 Slot micro-milling with 50 $\mu\text{m}$ axial depth of cut. Material: Brass 260. Tool: 200 $\mu\text{m}$ diameter. Spindle speed: 40,000 [rev/min]. Feed-rate: 5 $\mu\text{m}/\text{rev}/\text{tooth}$ .	63
Figure 4.1 Flow chart of cutting force prediction from FE model.	66
Figure 4.2 Finite element model of orthogonal micro-cutting process.	67
Figure 4.3 ALE constraint of the workpiece mesh.	69
Figure 4.4 Initial and machined chip in the FE simulation.	70
Figure 4.5 Material deformation with small uncut chip thickness.	70
Figure 4.6 Vector of workpiece velocity around too edge.	71
Figure 4.7 Spectrum of vertical velocity in the tertiary zone.	72
Figure 4.8 Simulated cutting forces with FE. Uncut chip thickness = 4 $\mu\text{m}$ , cutting speed = 25 m/min, tool edge radius = 8 $\mu\text{m}$ and primary rake angle = 5 deg, material: brass 260.	72
Figure 4.9 Simulated forces with cutting speeds. Cutting speeds: $v_1 = 12$ m/min, $v_2 = 25$ m/min, cutting edge radius = 4 $\mu\text{m}$ .	73
Figure 4.10 Comparison of cutting force prediction from FE model against slip-line field model and experiment. Tool edge radius = 20 $\mu\text{m}$ ; rake angle = 5 deg; clearance angle = 7 deg; cutting velocity = 25 m/min; material: brass 260.	74
Figure 4.11 Tool-chip contact length predicted by FE model. Tool edge radius = 20 $\mu\text{m}$ , rake angle = 5 deg.	75
Figure 4.12 Comparison of predicted strain, temperature and Von-Misses stresses by FE and slip-line field models in the primary shear zone. Tool edge radius = 20 $\mu\text{m}$ ; rake angle = 5 deg; clearance angle = 7 deg; uncut chip thickness = 25 $\mu\text{m}$ , cutting velocity = 25 m/min. Material: brass 260.	77
Figure 4.13 Predicted cutting forces. Material: brass 260. Cutting speed = 25 m/min and tool's primary rake angle = 5 deg. Symbols represent the simulated results from FE and slip-line field models, and the solid and dashed lines are the curved-fitted results.	78
Figure 4.14 Comparison of cutting forces and the frequency spectrums at: $n = 10,000$ rev/min, $c = 3$ $\mu\text{m}/\text{tooth}$ , $a = 50$ $\mu\text{m}$ . Material: brass 260.	80
Figure 4.15 Comparison of cutting forces and the frequency spectrums at: $n = 20,000$ rev/min,	

$c = 3 \mu\text{m/tooth}$ , $a = 50 \mu\text{m}$ . Material: brass 260. ....	81
Figure 4.16 Comparison of cutting forces and the frequency spectrums at: $n = 40,000 \text{ rev/min}$ , $c = 1 \mu\text{m/tooth}$ , $a = 50 \mu\text{m}$ . Material: brass 260. ....	81
Figure 4.17 Comparison of cutting forces and the frequency spectrums at: $n = 40,000 \text{ rev/min}$ , $c = 5 \mu\text{m/tooth}$ , $a = 50 \mu\text{m}$ . Material: brass 260. ....	82
Figure 4.18 Comparison of cutting forces and the frequency spectrums at: $n = 40,000 \text{ rev/min}$ , $c = 7 \mu\text{m/tooth}$ , $a = 50 \mu\text{m}$ . Material: brass 260. ....	82
Figure 4.19 Microstructure of normalized AISI 1045 steel. ....	83
Figure 4.20 Binary image converted from Figure 4.19. ....	83
Figure 4.21 FE model of workpiece material with ferrite and pearlite phases. ....	83
Figure 4.22 Stress-strain curves for various single structure steels [77]. ....	84
Figure 4.23 Chip formation with heterogeneous workpiece material. ....	85
Figure 4.24 Chip formation with homogeneous workpiece material. ....	85
Figure 4.25 Cutting forces with heterogeneous and homogeneous materials. ....	86
Figure 5.1 Dynamic micro-milling system. ....	90
Figure 5.2 Cutting forces predicted by slip-line field model (Material: AISI 1045 steel. $A=553.1\text{MPa}$ , $B=600.8\text{MPa}$ , $C=0.013$ , $n=0.234$ , $m=1$ , $T_m=1460 \text{ }^\circ\text{C}$ and $T_r=25 \text{ }^\circ\text{C}$ ). Symbols represent the simulated results from slip-line field model, and the lines show the curved-fitted results. ....	92
Figure 5.3 Comparison of micro-milling forces predicted by slip-line field model and experiment. ....	93
Figure 5.4 Schematic of single degree of freedom orthogonal cutting. ....	95
Figure 5.5 FE simulation of displacement, velocity and contact force in orthogonal cutting of AISI 1045 with a tool having $80 \mu\text{m}$ flank wear. ....	97
Figure 5.6 Measurement of tool edge geometry under optical microscope. ....	98
Figure 5.7 FE simulations of displacement, velocity and contact force in orthogonal cutting of AISI 1045 with a micro-tool. ....	99
Figure 5.8 Block diagram of chatter dynamics with process damping. ....	100

Figure 5.9 Flowchart of solving chatter stability in micro-milling.....	103
Figure 5.10 Experimental setup to measure the FRF of micro-mill. ....	104
Figure 5.11 Measured and curve-fitted FRF of micro-mill at tool tip. ....	105
Figure 5.12 Experimental setup for micro-milling test.....	108
Figure 5.13 Predicted stability lobes with process damping effect. All four modes of micro-mill are considered. ....	109
Figure 5.14 Predicted and experimentally evaluated chatter stability lobes.....	109
Figure 5.15 Microphone signals from chatter tests.....	110
Figure 5.16 AE signals from chatter tests. ....	111

# Nomenclature

## Symbols

$A$	Plastic equivalent strain in Johnson-Cook constitutive model
$A_m$	Directional matrix for regenerative cutting force
$[A_x, A_y]$	Coordinate of point $A$ in the slip-line field model
$B$	Strain-related constant in Johnson-Cook constitutive model
$B_m$	Directional matrix for process damping force
$C$	Strain-rate sensitivity constant in Johnson-Cook constitutive model
$C_t$	Process damping coefficient in tangential direction
$C_r$	Process damping coefficient in radial direction
$C_{pt1}$	Identified process damping coefficient in tangential direction in macro-cutting
$C_{pr1}$	Identified process damping coefficient in radial direction in macro-cutting
$C_{pt2}$	Identified process damping coefficient in tangential direction in micro-cutting
$C_{pr2}$	Identified process damping coefficient in radial direction in micro-cutting
$Cl_p$	Clearance angle of tool
$E_{pt}$	Energy dissipation caused by process damping force in tangential direction
$E_{pr}$	Energy dissipation caused by process damping force in radial direction
$F$	Dynamic milling force
$F_{dn}$	Dynamic micro-milling force in Laplace domain
$F_f$	Feed force in orthogonal cutting
$F_n$	Normal force in orthogonal cutting
$F_{pd}$	Process damping force

$F_{pt}$	Ploughing force in tangential direction
$F_{pt0}$	Static component of ploughing force in tangential direction
$F_{pr0}$	Static component of ploughing force in radial direction
$F_{pr}$	Ploughing force in feed direction in orthogonal cutting
$F_r$	Radial force in milling
$F_{rc}$	Regenerative force
$F_{st}$	Static cutting force
$F_t$	Tangential force in orthogonal cutting
$F_x$	Cutting force in X-direction
$F_y$	Cutting force in Y-direction
$F_\tau$	Friction force in orthogonal cutting
$F_0$	Static component of ploughing force
$G$	Matrix operator to determine slip-line geometry
$K_t$	Cutting force coefficient in tangential direction in orthogonal cutting
$K_f$	Cutting force coefficient in feed direction in orthogonal cutting
$K_r$	Cutting force coefficient in radial direction in milling
$K_{sp}$	Contact force coefficient
$L$	Matrix operator to determine slip-line geometry
$L_w$	Tool wear length
$N$	Number of flutes for a mill
$N_y$	Y-coordinate of point N in the slip-lien field model
$R$	Matrix operator to determine slip-line geometry

$R_1$	Radius of slip-line EN
$R_2$	Radius of slip-line BJ
$P$	Matrix operator to determine slip-line geometry
$P^*$	Matrix operator to determine slip-line geometry
$Q$	Matrix operator to determine slip-line geometry
$Q^*$	Matrix operator to determine slip-line geometry
$Q_y$	Y-coordinate of point Q in the slip-line field model
$[S_x, S_y]$	Coordinate of point S in the slip-line field model
$T$	Temperature of workpiece material
$T_r$	Initial work material temperature
$T_m$	Melting temperature of workpiece material
$T_p$	Tooth period in micro-milling
$[U_x, U_y]$	Coordinate of point U in the slip-line field model
$V$	Cutting velocity in orthogonal cutting process
$\vec{V}$	Cutting velocity vector in orthogonal cutting process
$\vec{V}_1$	Initial resultant velocity vector of the material in primary shear zone
$\vec{V}_2$	Final resultant velocity vector at point B in primary shear zone
$\vec{V}_3$	Final resultant velocity vector at point J in primary shear zone
$\vec{V}_4$	Final resultant velocity vector at point G in primary shear zone
$V_c$	Cutting velocity in micro-milling
$\vec{V}_{N1}$	Initial normal velocity vector of the material in primary shear zone
$\vec{V}_{N2}$	Final shear velocity vector of the material in primary shear zone
$\vec{V}_{S1}$	Initial shear velocity vector of the material in primary shear zone

$\vec{V}_{s2}$	Final shear velocity vector of the material in primary shear zone
$\vec{V}_t$	Velocity transition vector in the primary shear zone
$\Lambda$	Eigenvalue of characteristic equation in dynamic micro-milling
$\Phi(s)$	Transfer function in s-domain
$\Omega$	Angular speed of the spindle
$a$	Depth of cut in milling
$a'$	Real residue of the transfer function
$b'$	Imaginary residue of the transfer function
$c$	Feed rate in micro-milling test
$c_s$	Specific heat of the workpiece material
$c_t$	Process damping coefficient ratio between tangential and radial direction
$c_x$	Damping coefficient of micro-mill in X-direction
$c_y$	Damping coefficient of micro-mill in Y-direction
$d_{t,f}$	Constants of cutting force coefficients in tangential and feed directions
$d_z$	Differential depth of cut in milling
$e$	Column vector of a unit circle
$f$	Ratio of critical uncut chip thickness to edge radius
$h$	Uncut chip thickness
$h_0$	Intended uncut chip thickness in milling
$j$	Cutting flute number in micro-milling
$k$	Shear flow stress of workpiece material
$k_r$	Ratio of cutting force coefficients between radial and tangential direction
$k_G$	Shear flow stress at point G in the slip-line field model

$k_x$	Stiffness of micro-mill in X-direction
$k_y$	Stiffness of micro-mill in Y-direction
$k'$	Residue for stiffness in the transfer function
$l$	Thickness of the primary shear zone
$l_{GJ}$	Arc length of slip-line GJ
$m$	Thermal softening parameter in Johnson-Cook constitutive model
$m'$	Residue for mass in the transfer function
$n$	Strain-hardening parameter in Johnson-Cook constitutive model
$p$	Hydrostatic pressure of workpiece material
$p_G$	Hydrostatic pressure at point G in the slip-line field model
$p_{t,f}$	Constants of cutting force coefficients in tangential and feed directions
$q$	Index of shear velocity change in the primary shear zone
$q_{t,f}$	Constants of cutting force coefficients in tangential and feed directions
$r$	Tool edge radius
$r'$	Pole of the characteristic polynomial of the transfer function
$s$	Radial coordinate of slip-line in the primary shear zone
$v_s$	Shear velocity in the primary shear zone
$w$	Width of cut
$\dot{y}$	Tool vibration velocity in Y-direction
$\alpha_{t,f}$	Constants of cutting force coefficients in tangential and feed directions
$\alpha_\gamma$	Tool rake angle
$\beta_T$	Fraction of the deformation energy causing temperature increase
$\beta_{t,f}$	Constants of cutting force coefficients in tangential and feed directions

$\gamma$	Shear strain of workpiece material
$\dot{\gamma}$	Shear strain-rate of workpiece material
$\varepsilon$	Effective strain of workpiece material
$\dot{\varepsilon}$	Effective strain rate of workpiece material
$\dot{\varepsilon}_0$	Reference of effective strain rate of workpiece material
$\zeta$	Damping ratio
$\eta$	Intersection angle between slip-line and rake face in the sticking region
$\eta_1$	Angular range of slip-line DH
$\eta_2$	Angular range of slip-line HJ
$\eta_{BJ}$	Angular range of slip-line BJ
$\eta_{CH}$	Angular range of slip-line CH
$\eta_{JK}$	Angular range of slip-line JK
$\eta_{KB}$	Angular range of slip-line KB
$\theta_1$	Inclination angle of slip-line with respect to the x-axis at point Y
$\theta_2$	Inclination angle of slip-line with respect to the x-axis at point Z
$\theta_s$	Material separation angle on the tool's round edge
$\kappa$	Chip ratio
$\lambda$	Intersection angle between GJ and the back surface of the chip
$\mu$	Coulomb friction coefficient in the sliding contact region
$\rho$	Density of the workpiece material
$\sigma_n$	Normal stress on the rake face
$\sigma_y$	Material yield strength

$\sigma$	Effective flow stress of workpiece material
$\tau$	Tool-chip frictional shear stresses in the sticking contact region
$\tau_p$	Vibration period in micro-milling process
$v$	Tool displacement in micro-milling
$\dot{v}$	Tool velocity in micro-milling
$\phi$	Angular coordinate of slip-line in primary zone in slip-line field model Instantaneous immersion angle of the tool in micro-milling process
$\phi_1$	Inclination angle of slip-line EG
$\phi_2$	Inclination angle of slip-line TB
$\phi_3$	Inclination angle of slip-lines $O_1N$ and $O_2J$
$\phi_{st}$	Entrance angle of the cutter
$\phi_{ex}$	Exit angle of the cutter
$\varphi$	Intersection angle between the slip-line and the tool rake face
$\phi_B$	Shear angle at point B
$\chi$	Column vector of the slip-lines
$\psi$	Inclination angle of the slip-lines with respect to X-axis
$\omega_c$	Chatter frequency of micro-milling
$\omega_n$	Natural frequency of micro-mill
$\omega_y$	Natural frequency of orthogonal cutting tool in Y-direction
$\partial \alpha$	Infinitesimal distance along $\alpha$ slip-line
$\partial \beta$	Infinitesimal distance along $\beta$ slip-line
$\angle KCB$	intersection angle between slip-line KC and tool rake face ( $^\circ$ )

## **Acronyms**

FRF	Frequency response function
FE	Finite element
ALE	Arbitrary Lagrangian Eulerian
RP	Reference point
SL	Slip-line field model

# Acknowledgements

I would like to convey my sincere gratitude to my supervisor Dr. Yusuf Altintas for his guidance and support. As a world-class academic, Dr. Altintas always manages to discuss with every student about the research in detail, and gives most valuable and timely feedback. He can be tough sometimes in order to keep high academic standard, but also cares so much about the student's professional and personal development. Dr Altintas' attitude toward work, student, life and his personality will be a life-long inspiration to me.

I would like to express my heartfelt gratitude to my parents. Their encouragement and love have been always the motivation for me to keep making progress during the Ph.D. study.

I am indebted to my beloved wife, Dr. Chao Wang. This thesis could not have been completed without her understanding and support. In the first four years of my Ph.D., Chao was also trying to complete her degree in China, and the total time we spent together was less than four months. However, we compensated the loss by working in the same lab everyday in the fifth year, with the help of Dr. Altintas who hired her as a postdoctoral fellow at the Manufacturing Automation Laboratory (MAL) at UBC.

I also would like to thank all my colleagues in MAL. They are hard-working, friendly, warm and always willing to help. I have been enjoying studying and working at Manufacturing Automation Laboratory.

In the end, I want to thank all the friends in Vancouver, who made my Ph.D. study an enjoyable and fruitful journey.

# Dedication

## **Dedicated to:**

*My Parents Man Jin and Zhen Zhao;*

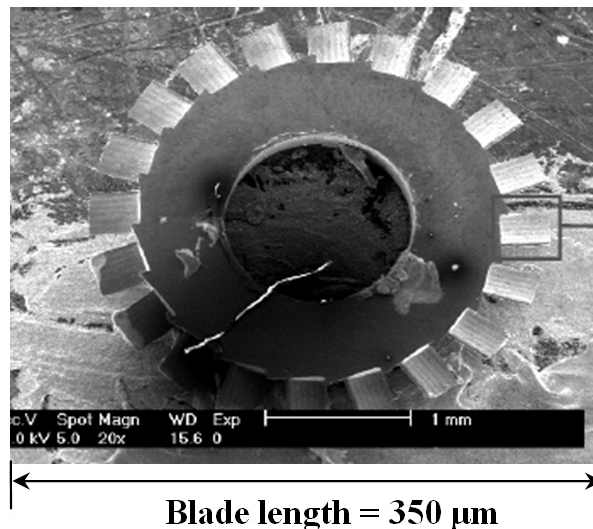
*My Wife Chao Wang;*

*and the Coming Baby Girl !*

# Chapter 1

## Introduction

Advancements in biomedical, optics, electronics, sensors, die and mold industries have led to the increasing demand for high-accuracy miniaturized components. These components usually have complex geometries requiring micron level accuracy. The manufacturing methods commonly used for the production of micro-structured components are photolithography and ion beam etching. However, these methods are time consuming and limited to a few silicon-based materials with planar geometries. Compared to the chemical manufacturing processes, micro-cutting has the advantage of fabricating small components with complex three-dimensional features in a broad range of materials. Figure 1.1 shows a miniature part produced by micro-cutting operation [1].



© Journal of Advanced Manufacturing Technology, 2005, by permission.

Figure 1.1 Miniature part produced by micro-cutting operation [1].

The diameters of micro-end-mills are in the range of 25  $\mu\text{m}$  to 1.0 mm with 2–10 mm long flutes. In comparison to macro-milling, the dimensions of chip loads and tool geometry for micro-milling operations are typically an order of magnitude lower, which present difficulty in modeling and process control. Figure 1.2 shows the comparison of the

size and shape between a macro-mill and micro-mill. Tool geometry, cutting speed, chip load and depth of cut must be properly selected to avoid premature wear and breakage of the micro-mill flute, as well as produce smooth surface finish with desired accuracy on the miniature parts. The prediction of cutting force, stress, temperature and vibration rely on the work material properties, tool geometry and cutting conditions. The cutting mechanics and dynamics of micro-milling have to be modeled in order to predict the process behavior ahead of costly physical trials.

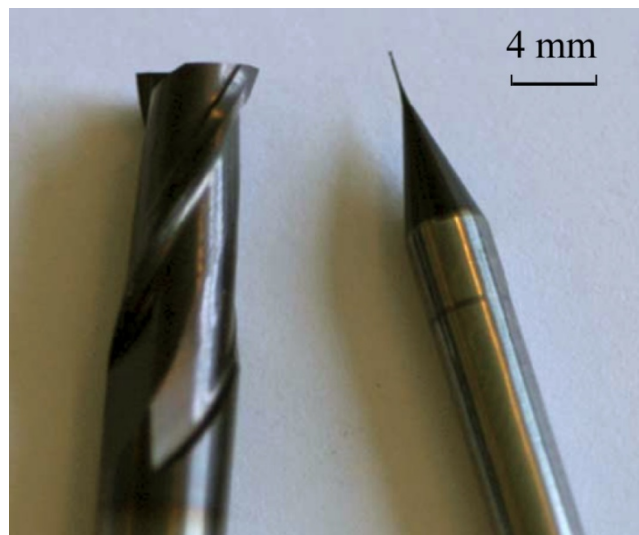


Figure 1.2 Comparison of macro-mill and micro-mill.

Unlike macro-mills for which chip loads reach up to  $300\ \mu\text{m}$  per flute, chip loads for micro-end-mills are typically within the range of  $25\ \mu\text{m}$ . Since the cutting edge is typically ground with a  $2\text{-}20\ \mu\text{m}$  radius, the assumption of having an infinitely sharp cutting edge is not valid in modeling the mechanics of micro-cutting operations. The same argument is valid in finish machining of hardened steel and thermal resistant alloys where the chip loads are comparable to the radius of the cutting edge. Figure 1.3 shows the chip formation and material flow in the orthogonal micro-cutting process with a round tool edge. The material bifurcates upward and downward at the separation point (S). The material that flows under point S is compressed to form the finishing surface, which is defined as the ploughing effect. Negative rake angle in the ploughing region due to round tool edge causes large deformation of workpiece material. The ploughing force component cannot be

neglected in evaluating the total cutting force. The round tool edge effect needs to be considered for the prediction of stress distribution and cutting force. In this thesis, the round tool edge effect is considered using analytical and numerical methods to model the micro-cutting mechanics.

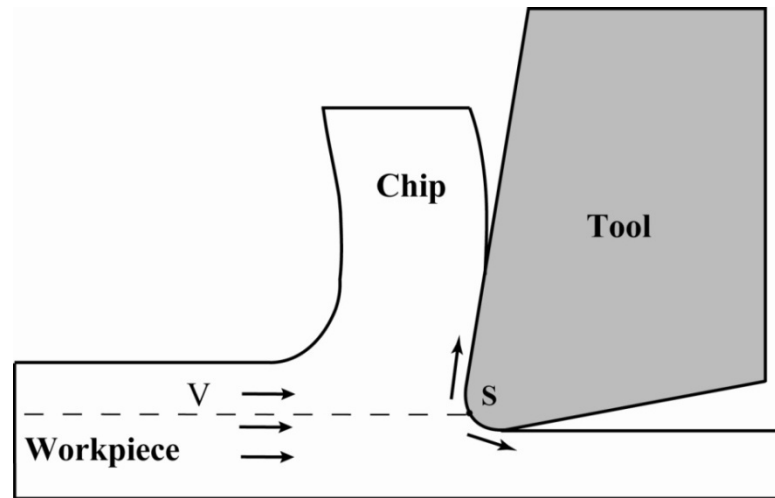


Figure 1.3 Material flow in orthogonal micro-cutting.

One of the fundamental obstacles in improving the surface quality in micro-milling is chatter. Chatter vibration is a result of a self-excitation mechanism in the generation of chip thickness during cutting operations. When the dynamics of the closed-loop cutting system become unstable, the growing chip thickness increases the cutting forces and may break the tool and leave a poor surface finish [2]. Prediction of chatter vibration requires the cutting force model and identification of the frequency response function (FRF) at the tool tip. In conventional cutting operations, the dynamic parameters of an end mill are obtained through impact modal testing, which requires measurement of tool tip vibrations by exciting the tool with an impact hammer. Such testing becomes practically infeasible to apply on micro-mills with extremely small tool tips. Moreover, the impact hammer tests can only be applied in the excitation frequency range below 10 kHz, which is typically less than the natural frequency of a micro-mill tool tip. In this thesis a piezo-actuator is developed to experimentally identify the FRF of micro-mill up to 120 kHz.

The contact between tool cutting edge and work material in the ploughing region generates process damping effect on the cutting process. Tool vibration in feed direction

results in energy dissipation in the ploughing region, adding extra damping on the tool vibration beside the structural damping effect. Process damping increases the stability at low spindle speeds. Process damping coefficient depends on the elastic-plastic properties of the workpiece, tool edge geometry and cutting conditions. Chatter stability is predicted in this thesis including the process damping coefficient identified through finite element simulations.

The objective of this thesis is to model the mechanics and dynamics of micro-cutting process from material constitutive property, tool edge geometry and cutting conditions. Analytical and numerical techniques are applied to model the material deformation mechanism with round tool edge effect. The models are used to simulate strain, temperature and stress distributions in primary, secondary and tertiary shear zones, and predict the cutting forces including shearing and ploughing effects. Cutting force coefficients identified from the orthogonal micro-cutting model are used to predict micro-milling forces. The novel non-linear cutting force model, the frequency response function experimentally identified at micro-mill tip in high frequency range, and the process damping coefficient in the ploughing region identified by finite element model are integrated to predict the chatter stability in micro-milling. The flow chart of the research content in the thesis is shown in Figure 1.4.

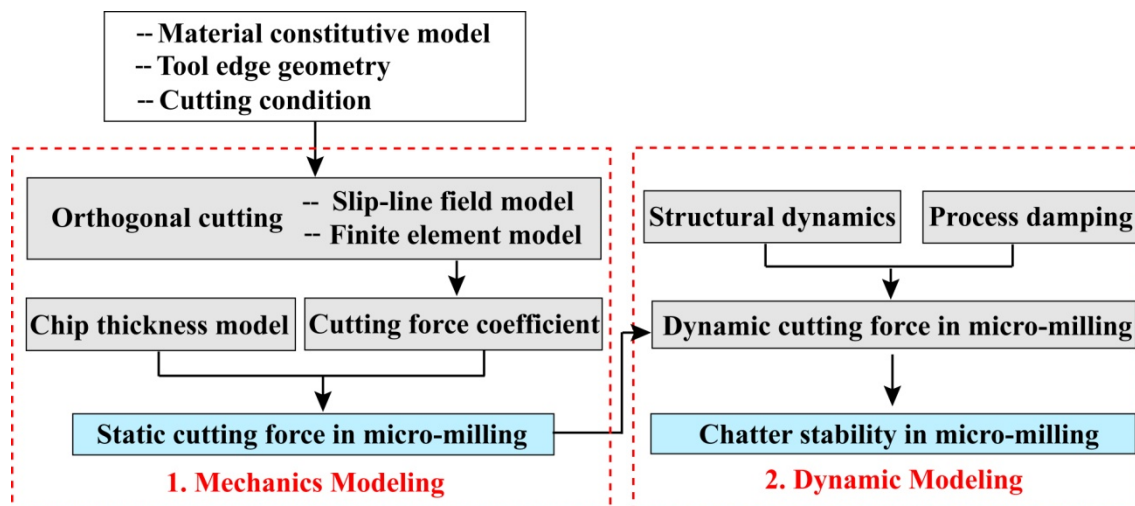


Figure 1.4 Flow chart of research content.

The thesis structure is organized as follows: A detailed review of the literature is presented in Chapter 2. Chapter 3 proposes a slip-line field model of the micro-cutting process with round tool edge effect. Strain, strain-rate, temperature and flow stress in the primary shear zone are modeled from constitutive properties of workpiece material and tool edge radius. Shearing and ploughing effects are included in evaluating the cutting force. Cutting force coefficients are modeled as non-linear functions of chip load and tool edge radius, and applied to predict the cutting forces in micro-milling. The simulated results are compared against experimental measurements in both micro-turning and micro-milling. In Chapter 4, a numerical model of orthogonal micro-cutting with a round cutting edge is developed using finite element (FE) method. Chip formation is simulated and cutting forces are predicted. The simulation results are compared with the slip-line field predictions and the experimental measurements. Micro-cutting process of heterogeneous workpiece material using FE model is presented in the same chapter. Chapter 5 presents the prediction of chatter stability in micro-milling. The cutting force coefficient is obtained based on slip-line field simulations. The frequency response function of micro-mill is experimentally identified through miniature piezoelectric actuator and laser vibrometer. The chatter stability is predicted including the process damping effect due to round cutting edge. The average process damping coefficient is identified from FE simulations considering the energy dissipation in the ploughing region. The simulation results are compared against micro-milling experiments using microphone and acoustic emission sensor. Concluding remarks and future research directions are discussed in Chapter 6.

# Chapter 2

## Literature Review

### 2.1 Overview

This chapter is focused on reviewing the relevant work in the literature. The cutting mechanics modeling with tool edge effect using mechanistic, slip-line field and finite element method is discussed. The review on micro-cutting dynamics includes the identification of micro-mill FRF and chatter stability prediction including the process damping effect.

### 2.2 Modeling of cutting mechanics

#### 2.2.1 Mechanistic model

Mechanistic model is used to predict cutting force, torque and power based on the empirical cutting coefficients identified from experimentally measured cutting forces. Bao and Tansel [3] predicted the micro-milling force from mechanistic model considering the trajectory of the tool tip while the tool rotated and moved ahead simultaneously. Tangential and radial forces were modeled proportional to the cutting area, therefore the ploughing effect was not considered. Kang et al. [4] included the tool edge radius effect and tool-workpiece contact at the flank face in the cutting force model, but several constants related to material property in the cutting force model had to be experimentally calibrated. Bissacco et al. [5] incorporated the ratio between the uncut chip thickness and cutting edge radius on oblique cutting force model. Orthogonal cutting tests were performed to measure the cutting forces and chip ratio in order to identify the shear angle, friction angle, and edge coefficients. Malekin et al. [6] included the shearing and ploughing dominant cutting regimes in the mechanistic model. Tool structural dynamics was considered. The ploughing forces were modeled proportional to the volume of interference between the tool and the workpiece. The ploughing force coefficients were identified through micro-milling

experiments. Lee et al. [7] proposed a model with instantaneous cutting force coefficients independent of cutting conditions. Specific cutting forces in the normal and frictional directions on the rake surface were used. The effective rake angle along the round cutting edge and the minimum chip thickness effect were included. Jun et al. [8] developed the mechanistic models for shearing and ploughing dominant regions separately. The effective rake angles at the round cutting edge and the elastic recovery of workpiece material were considered. Zaman et al. [9] applied the mechanistic model to predict three-dimensional cutting forces. The chip area was obtained considering the tool edge path and tool helix. Vogler et al. [10] used the mechanistic model to predict the micro-milling forces considering multiple phases in the workpiece material. The cutting coefficients for pure ferrite and pearlite materials were experimentally identified. The magnitude and variation of cutting forces in cutting ductile iron showed the material microstructure effects on micro-milling.

The literature shows that the mechanistic model is effective in predicting the cutting forces in micro-milling provided that the cutting force coefficients are accurately identified from experiments. However, understanding the material deformation mechanism influenced by tool edge radius relies on the modeling of the chip formation and flow stress, cannot be explained by the mechanistic models which are empirical. Slip-line field analysis technique and numerical technique such as finite element method are able to predict the plastic flow of workpiece material in the cutting process with round tool edge effect, and model the stress, strain and temperature fields in the primary, secondary and tertiary deformation zones.

### **2.2.2 Slip-line field model**

Slip-line field theory provides an analytical approach to model the plastic deformation of solid material under plane strain conditions. Based on stress equilibrium condition, the slip-lines which represent the directions of maximum shear stress and maximum shear strain-rate are obtained. The distribution of flow stress and hydrostatic pressure are calculated from Hencky's equations along the slip-lines [11].

The cutting mechanics models reveal that the chip formation is due to the shearing of the work material ahead of the tool. Merchant [12] developed an orthogonal cutting model assuming that the continuous chip was formed by plastic deformation in an infinitely thin shear plane. The shear strength of the work material was assumed to be constant along the shear plane.

Lee and Shaffer [13] proposed a triangular slip-line field model of chip formation. The plastic deformation field was assumed to extend above shear plane with slip-lines parallel to and normal to the shear plane. The flow stress in the material deformation zone was assumed to be constant. The chip shape was assumed straight, therefore the tool-chip contact length was not considered.

Kudo [14] and Dewhurst [15] presented the slip-line fields considering the curled chip. Main feature of these models was a curved shear plane resulting into the material velocity gradient across the chip. The contact length between the curled chip and flat tool rake face was considered. Matrix operator technique developed by Dewhurst and Collins [16] were applied to determine the geometric parameters which were used to construct the slip-line fields. Matrix operator method represented the slip-lines by the column vector of coefficients in a series expansion of its radius of curvature. The geometric coordinates of the slip lines were calculated by matrix multiplications.

The slip-line field theory only considers the plastic deformation of the material. Childs [17] incorporated the elastic contact between the tool and chip in the slip-line field model, leading to improved prediction of the process mechanics. The model assumed a constant friction stress in the plastic contact region and the stress decreased parabolically over the elastic contact part. The ratio between the normal pressure and friction stress in the elastic contact region was assumed to be constant.

All the slip-line field models in the literature assumed that the primary shear zone was a line and the flow stress of the work material was constant. However, based on the experimental observations by Palmer and Oxley [18] on the slow orthogonal cutting of mild steel, the primary shear zone was a region with certain width, and the material moved

smoothly from the work to the chip.

Since the cutting process involves large deformation, high speed and high temperature, the effect of strain, strain-rate and temperature on the flow stress of material needs to be included in the cutting force model. Oxley and Welsh [19] proposed a parallel-sided shear zone model of chip formation. The variation of flow stress with strain, strain-rate and temperature was included, and the effects of strain-hardening and strain-rate on shear angle were considered.

Roth and Oxley [20] conducted the slip-line field analysis on orthogonal cutting based on the experimental flow field. It was concluded that flow stress of workpiece material increased from the entry location of plastic zone to the chip zone due to strain-hardening, which should be considered in the mechanics modeling. However, along the tool-chip interface where the material had been severely strained, a constant flow stress condition could be applied on the slip-line field analysis.

Adibi-Sedeh et al. [22] extended Oxley's analysis by applying the Johnson-Cook material model, history-dependent power material model, and the mechanical threshold stress model to represent the mechanical property of workpiece material. The effects of strain-gradient and thermal-gradient were included in the slip-line field model. It was concluded that the model was able to predict the cutting forces and chip thickness as a function of uncut chip thickness and cutting speed. The temperature in the primary and secondary shear zones could be predicted as well.

Several slip-line field models reported in the literature focused on the effect of tool edge geometry on cutting process. Shi and Ramalingam [23] proposed a slip-line field model of orthogonal cutting with a chip breaker and flank wear land. The model included a primary deformation zone with a finite thickness. Two deformation zones along the rake face and flank face of the worn tool were modeled. The normal and shear stresses at the flank wear land were modeled as constant, which was shown consistent with experimental observations. However, the strain-hardening effect was not included.

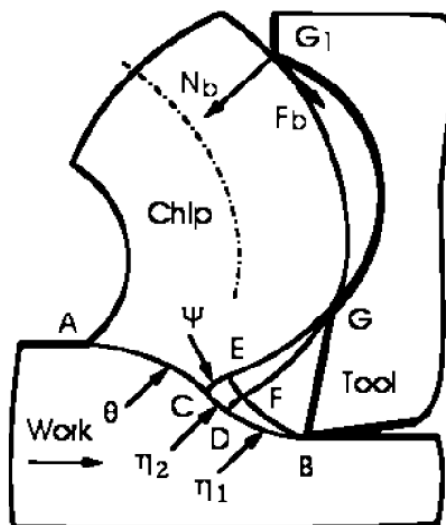
Waldorf et al. [24] proposed a slip-line field model with round tool edge. Ploughing

components of the cutting force were modeled. It was based on the assumption of a stable build-up adhered to the tool edge. Instead of material separating at a stagnation point on the edge, the flow was diverted at the edge of the build-up.

Manjunathaiah and Endres [25] proposed a slip-line model with tool edge effect. Arc of the tool below separation point was approximated by a straight line. Based on the force balance on the lower boundary of the plastic deformation zone, the ploughing force was modeled as a function of tool edge radius. An increase in force due to an increase in edge radius was attributed to the ploughing mechanism.

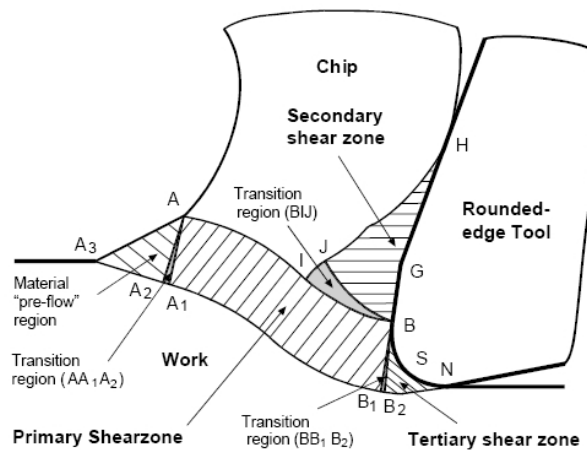
Ren and Altintas [26] presented the slip-line field model of cutting process with chamfered tools. The effects of strain, strain-rate, and temperature on material flow stress were considered. The dead metal zone close to tool edge was modeled as an extrusion process. Cutting forces were predicted based on minimum energy principle.

Fang and Jawahir [27] proposed a slip-line field model of cutting with restricted contact grooved tools. Strain, strain-rates and temperatures effects are included in modeling the flow stress of the workpiece material. However, this model neglected the tool edge effect, and the primary deformation zone was modeled as a thin shear plane AB, shown in Figure 2.1.



@ CIRP Annals-Manufacturing Technology, 2002, by permission  
 Figure 2.1 Slip-line field model proposed by Fang and Jawahir [27].

Fang [28][29] proposed a generalized slip-line field model with a round edge tool shown in Figure 2.2. The material deformation region consists of primary shear zone, secondary shear zone, tertiary shear zone, material pre-flow zone, and three small transition zones. The thickness of primary shear zone was determined by the tool edge radius. The chip up-curling effect was considered. However, the material was considered to be rigidly plastic with constant shear flow stress. The tool-chip frictional shear stress along each section of the rake face was assumed to be constant, which neglected the sliding contact zone.



© Journal of the Mechanics and Physics of Solids, 2003, by permission.

Figure 2.2 Slip-line field model proposed by Fang [28][29].

Wang and Jawahir [30] proposed a slip-line field model for machining with a restricted contact grooved tool having a finite edge radius. The effects of strain, strain-rate, and temperature on the material flow stress were included. However, only average values of strain and strain-rate were modeled, the variation of flow stress inside the primary shear zone was not considered.

The slip-line models in the literature provided analytical solutions for cutting force prediction. The effect of tool edge geometry on the cutting process was included. The shape and size of material deformation zones were determined based on the tool geometry and uncut chip thickness. However, the models assumed a constant material flow stress in the shear zones. The average values of strain and strain-rate were applied to model the effects of strain hardening, speed and temperature. Therefore, the variation of material flow stress

was neglected. This thesis proposes a slip-line field model which simulates the stress distribution inside the deformation zones with the round tool edge effect in orthogonal cutting. The cutting forces are predicted including shearing and ploughing effects. The cutting force coefficients identified from slip-line field simulations are used to predict micro-milling forces.

### **2.2.3 Finite element model**

The effect of the round cutting edge on the cutting process has also been analyzed using Finite Element Method (FEM), which led to the prediction of chip formation, temperature, stress and cutting forces. Moriwaki et al. [31] applied the rigid-plastic FEM to analyze the mechanics of orthogonal micro-cutting process of copper. The roundness of the tool edge was considered. Flow of cutting heat and the temperature distribution in both workpiece and tool were simulated. It was shown that both the specific tangential and feed forces increased with an increase of ratio between tool edge radius and uncut chip thickness.

Kim et al. [32] developed an FE model of orthogonal cutting process with round tool edge effect. The model was based on Eulerian formulation and the workpiece material was assumed rigid-viscoplastic. The chip geometry was initially guessed and later adjusted using free surface and tool-chip contact conditions. The simulation results showed that the increased tool edge radius changed the temperature distribution of the tool, and shifted the location of maximum temperature to the tool edge. However, the shear angle or the chip thickness didn't change.

Movahhedy et al. [33] modeled the cutting process with chamfered and blunt tools based on Arbitrary Lagrangian and Eulerian (ALE) formulation. ALE combined the feature of Lagrangian analysis in which the mesh was attached to the material, and Eulerian analysis where the mesh was fixed in space while the material moved through the mesh in Eulerian region. The mesh moved independently from the material in the ALE mesh domain. The simulation results included the chip formation, stresses, temperature, and cutting forces. It was shown that a dead metal zone existed under the chamfer. Tangential

and feed forces with respect to chamfer angles and cutting speeds were simulated and compared against experimental results.

Liu and Melkote [34] developed a strain gradient plasticity-based finite element model of orthogonal micro-cutting of aluminum. The results showed that the tool edge radius affected the material flow pattern around the tool edge by widening the plastic shear zone, and caused higher energy dissipation due to increased tool–chip contact length at smaller uncut chip thickness values. The specific cutting energy increased nonlinearly with decreased uncut chip thickness which explained the size effect in micro-cutting.

Simoneau et al. [35] included the effects of grain size and orientation in the micro-cutting of AISI 1045 steel. The heterogeneous FE model included two materials which represented ferrite and pearlite grains respectively. Pearlite material was assumed three times harder than ferrite material. Pearlite grains were modeled spreading throughout ferrite matrix with random shape and position. The simulation results showed that material microstructure resulted into extrusion effect in chip formation and generated defects on the machined surface.

Vogler et al. [36] developed cutting force model for micro-milling including the tool edge radius effect. Finite element simulations were performed to calibrate the cutting force parameters for both single-phase ferrite and pearlite materials. The force model was validated by the micro-milling experiments on the single-phase and the multiphase ductile iron workpiece.

Woon et al. [37] investigated the effect of tool edge radius on tool-chip contact and flow stagnation phenomenon around tool edge in micro-cutting of AISI 1045 steel. Based on the spatial velocity results of work material, the position with zero velocity was determined as stagnation point. It was observed that stagnation point angle was not sensitive to the changes of uncut chip thickness in the range of 2-20  $\mu\text{m}$  with 10  $\mu\text{m}$  tool edge radius.

Dhanorker and Ozel [38] developed the FE model of meso/micro scale milling of AL 2024-T6 aluminum and AISI 4340 steel. Chip formation, strain, temperature and cutting

forces were simulated. Ploughing effect was observed from the simulation. Minimum chip thickness was predicted with different tool edge radii and cutting speeds.

Childs [39] conducted FE simulations of continuous chip formation with a range of uncut chip thicknesses and edge radii for medium carbon steel. Ploughing force was expressed as a function of edge radius, uncut chip thickness, chip shear plane angle and flow stress. Nonlinearity of force variation with uncut chip thickness was demonstrated. It was concluded that the size effects in machining of steels were due to the ploughing effect caused by tool round edge. Ductile fracture energy from forming fresh surfaces didn't contribute to the size effect.

Afazov et al. [40] developed an FE model of orthogonal micro-cutting process with round tool edge. The cutting force coefficients were identified as nonlinear functions of uncut chip thickness and cutting velocity from the simulations. The micro-milling forces were predicted considering the trajectory of tool edge and run-out effect, and the simulations were compared against experimental results. The simulated cutting forces from the FE model of orthogonal micro-cutting showed large oscillations, which could affect the identification of cutting force coefficients.

Finite element method provides numerical solutions for micro-cutting simulations considering round tool edge effect. The chip formation in transient and steady-state cutting processes is simulated. The stresses, temperature distribution and cutting forces are predicted based on the constitutive model of workpiece material and tool-workpiece contact property. However, the accuracy of the cutting force prediction from FE model is not fully analyzed. This thesis develops an FE model of orthogonal micro-cutting process, and the simulated cutting forces from both slip-line field and FE models are compared against experimental observations. The prediction results are analyzed by investigating the stress and temperature distributions from the simulations.

## **2.3 Modeling of cutting dynamics**

Cutting dynamics models consider the tool vibrations in the metal cutting processes.

Excessive vibrations generate poor surface finish and cause premature tool wear and damage. Micro-mill experiences both forced and chatter vibrations during machining operations, in which chatter vibrations are the most detrimental for the safety and quality of the machined workpiece. Chatter results from the regeneration of chip thickness during cutting process [2]. One of the structural modes of the machine tool-workpiece system is excited by cutting forces, and a wavy surface finish is left by the cutter teeth. The dynamic chip thickness is affected by the phase shift between the two successive waves. When the dynamics of the cutting system become unstable, the growing chip thickness increases the cutting forces and vibrations which may break the tool and leave a poor surface finish. The prediction of chatter stability requires the modeling of dynamic chip thickness and cutting forces as a function of material properties, cutting tool geometry and vibrations. Frequency response function at the tool tip and process damping caused by the ploughing of a wavy surface finish at the round tool edge also need to be identified.

### **2.3.1 Identification of FRF at tool tip**

The FRF at the tool tip is directly measured through impact modal tests in macro-milling, which is not applicable for fragile micro-mills. Moreover, the impact modal tests can only be applied in the excitation frequency range below 10 kHz, which is less than the typical natural frequency of the micro-mills which may reach beyond 100 KHz. Filiz and Ozdoganlar used Timoshenko beam equation to model the micro-mill dynamics, including the setup errors, the sectioned tool geometry, and the actual cross section of cutter flutes [41]. The model was experimentally validated by measuring the natural frequencies and mode shapes of micro-mills using laser vibrometer coupled with a microscope [42]. Free-free boundary conditions were obtained by suspending the tool using elastic bands. The dynamic excitation was delivered through miniature piezoelectric elements attached to the tool shank.

Mascardelli et al. [43] predicted the FRF of the micro-mill using receptance coupling technique to mathematically couple the spindle/micro-machine and arbitrary micro-tools with different geometries. The FRF of the spindle/micro-machine was measured

experimentally through impact hammer testing. The dynamics of an arbitrary tool substructure were determined through FE analyses. Joint rotational dynamics were determined through experimentally measuring the FRFs of gauge tools.

Jun et al. [44][45] modeled the micro-mill as a rotating Timoshenko beam with varying cross-sectional area. Alignment and manufacturing errors such as tool tilting angle and runout were included, and finite element method was used to obtain the equation of motion. Dynamic cutting forces and tool tip vibrations from simulations were compared with experimental results.

Previous work shows that no direct FRF measurement on micro-mill has been conducted including the clamping dynamics at tool-holder/micro-mill joint. The analytical solutions of FRF prediction require the identification of boundary conditions. However, any errors in identified boundary conditions will lead to inaccurate FRF results. This thesis provides an experimental setup to measure the FRF directly at the tool tip through non-destructive methods. FRF in the frequency range of 0 – 120 kHz at tool tip is measured by a miniature piezoelectric actuator attached to the micro-mill shank when the tool is clamped in the spindle.

### **2.3.2 Identification of process damping**

The contact between cutting edge and work material generates process damping effect in dynamic cutting when the cutting speed is significantly lower than the velocity of tool tip vibrations [46]. Contact force causes energy dissipation and increases stable cutting depths at low spindle speed. Sisson and Kegg [47] proposed that a part of chip thickness proportional to the cutting edge radius was compressed under the tool edge in the ploughing region shown in Figure 2.3.

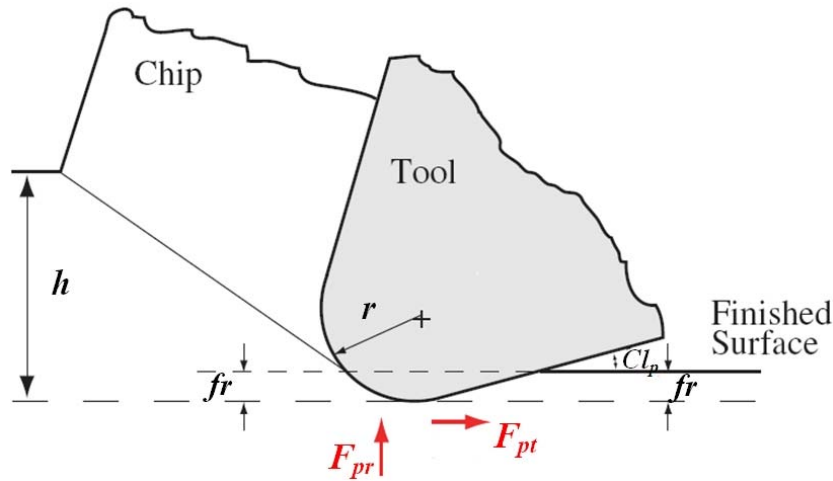


Figure 2.3 Process damping force with round tool edge effect proposed by Sisson and Kegg, reproduced from [47].

The process damping forces are expressed as:

$$F_{pr} = -w\sigma_y \frac{fr}{Cl_p^2} \frac{\dot{y}}{V}, \quad F_{pt} = \mu F_{pr} \quad (2-1)$$

where  $\sigma_y$  is material yield strength,  $Cl_p$  is tool's clearance angle,  $fr$  is the thickness of material which is in contact with tool's clearance face,  $W$  is width of cut. Process damping force is proportional to the vibration speed  $\dot{y}$  and inversely proportional to the cutting speed  $V$ . However, this model assumes a constant material yield strength and neglects strain-hardening and temperature effects on the flow stress of workpiece material.

Chiou and Liang [48] predicted the process damping force as a function of flank wear land. The specific contact force was experimentally identified through indentation test on aluminum workpiece. Altintas et al. [49] identified the process damping coefficients from the dynamic plunge turning tests. The cutting tool was oscillated by a piezo-actuator-driven fast tool servo at desired frequency and amplitude. Dynamic cutting forces and tool displacement were measured to extract the process damping coefficients. Eynian and Altintas identified the contact force coefficient through static indentation test with tool flank wear, and used it in predicting the chatter stability of general turning [50] and milling [51] with process damping. Budak and Tunc [52] identified the process damping coefficient

from the chatter tests using experimental and analytical stability limits. They calibrated the indentation coefficient of the material through energy dissipation method. The indentation volume was calculated including the effects of tool edge radius and clearance angle. Rahnama et al. [53] calculated the process damping coefficient from the experimentally measured cutting forces at low feed rates micro-milling process in which the ploughing effect was dominant.

It is preferred to avoid experimental identification of process damping, and model it directly from the contact mechanics using the material properties and tool geometry. This thesis uses finite element method to simulate the process damping force and tool vibration in orthogonal cutting process, and identify the process damping coefficient from material constitutive property.

### **2.3.3 Chatter stability of micro-milling**

Prediction of chatter stability is based on the identification of cutting force coefficient, structural dynamics of micro-mill and process damping at cutting edge. Park and Rahnama [54] proposed robust chatter stability in micro-milling based on the edge theorem. Variations of micro-mill dynamics and cutting force coefficients were considered. Robust chatter stability lobes showed more conservative values compared to the conventional method. Shi et al. [55] conducted micro-milling tests and analyzed the influences of process damping, clamping conditions, and tool shank length on chatter frequencies. Piezo-actuators were developed for online chatter detection in micro-milling. Broadband excitations were applied on workpiece by the piezo-actuator during milling process, and laser vibrometer was used to measure the vibration velocity at tool shank. The measurement results showed that the chatter frequencies were able to be detected in stable cutting region. Afazov et al. [56] simulated the micro-milling chatter numerically by considering the nonlinear cutting force coefficients which were identified from FE model. The effects of uncut chip thickness and velocity on cutting forces were considered. However, process damping effect was not included in the model.

This thesis predicts the chatter stability in micro-milling by considering the process

damping caused by round cutting edge and the micro-mill dynamics in high frequency range. The cutting force coefficients are identified based on the slip-line field simulations. Chatter stability lobes are predicted in frequency domain by using the process damping coefficients obtained from the constitutive model of the material, and directly measured FRF of the micro-mill. The simulation results are compared with the experimental measurements using a microphone and an acoustic emission sensor.

# Chapter 3

## Slip-line Field Modeling of Micro-cutting Process<sup>1</sup>

### 3.1 Overview

This chapter presents an analytical mechanics model of orthogonal micro-cutting process with a round edge cutting tool. Slip-line field theory is used to model the stress distribution of workpiece material under plastic deformation. Material deformation region is divided into the primary, secondary and tertiary zones. The Johnson–Cook constitutive model is applied to obtain the shear flow stress and hydrostatic pressure as functions of strain, strain-rate, and temperature. The chip curling, sticking and sliding contact along the tool rake face, and the ploughing effect under the material separation point are considered. The total cutting forces are evaluated by integrating the normal and frictional stresses along the entire chip-rake face contact zone and the ploughing region caused by the round tool edge. The proposed model is experimentally verified by a series of cutting force measurements conducted during micro-turning tests on brass 260.

The cutting force coefficients are modeled as nonlinear functions of tool edge radius and uncut chip thickness from a series of slip-line field simulations. The identified cutting force coefficients are used to simulate micro-milling forces considering the actual tool tip trajectory, radial tool run-out and the dynamometer dynamics. The proposed chain of predictive micro-milling model is experimentally validated by conducting brass cutting tests with a 200  $\mu\text{m}$  diameter helical end mill.

The content of this chapter is arranged as follows. Section 3.2 gives a brief introduction to the slip-line field model of orthogonal micro-cutting with round tool edge

---

1. The content of Chapter 3 has been published in two journal articles: (1) Jin, X., Altintas, Y., 2011, Slip-line Field Model of Micro-cutting Process with Round Tool Edge Effect, *Journal of Materials Processing Technology*, vol.211, 339–355. (2) Altintas, Y., Jin, X., 2011, Mechanics of micro-milling with round edge tools, *Annals of CIRP*, 60/1, 77-80.

effect. Section 3.3 illustrates the procedure to determine the slip-line field geometry in each deformation zone. Detailed modeling of the shear flow stress and the hydrostatic pressure from strain, strain-rate and temperature distributions is laid out in Section 3.4. Section 3.5 shows the identification of geometric parameters for the slip-line field model. Cutting forces prediction from the stress modeling in the secondary and tertiary shear zones is presented in Section 3.6. Section 3.7 explains the experimental validation of the slip-line field model by micro-turning tests. In Section 3.8, the cutting forces prediction for micro-milling based on the slip-line field simulations are presented. Concluding remarks are given in the last section.

## **3.2 Slip-line field model**

The material deformation region in the cutting process is divided into three zones: the primary shear zone, secondary shear zone, and tertiary zone. The shape of the slip-line field with tool's round edge effect was originally proposed by Fang [28][29]. The thickness of the primary shear zone was influenced by the tool edge radius in his model. However, the material was considered to be rigid plastic with constant shear flow stress, and the tool-chip frictional shear stress along the entire tool rake face was assumed to be constant. Due to the high cutting speed and large deformation of the material in the micro-cutting process, the effects of strain, strain-rate, and temperature on the material flow stress are considered in the proposed model, the sticking and sliding contact regions between the tool and workpiece are included.

The slip-line field model of orthogonal micro-cutting process with a round edge tool is shown in Figure 3.1. Plane strain deformation and steady state cutting conditions are assumed. The primary shear zone consists of three regions: triangular region QEG is due to the pre-flow effect reported by Armarego and Brown [57]. Since line QG is a stress-free boundary, all of the slip-lines in QEG intersect with QG at a 45° angle. Green [58] proved that region GJNE is convex upward because of the curling-back effect of the chip; region JBNT is concave downward due to the friction between the chip and the tool rake face.

Slip-lines in region GJNE and region JBTN are simplified as circular arcs and straight radial lines;  $O_1$  is the center of the circular arcs in region GJNE, and  $O_2$  is the center of the circular arcs in region JBTN. The shear flow stress and hydrostatic stress are modeled by including the effects of strain, strain-rate, and temperature of the material.

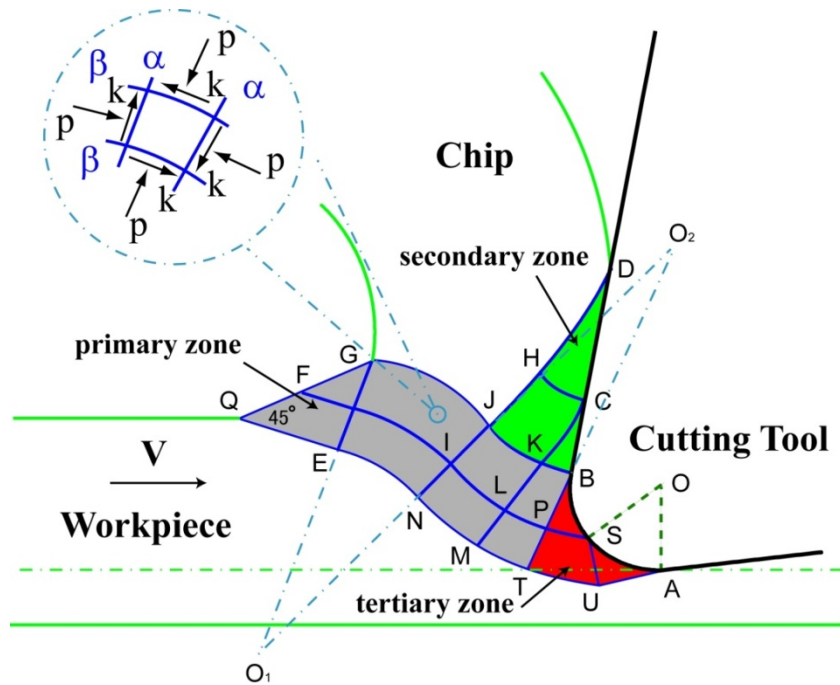


Figure 3.1 Slip-line field model of orthogonal micro-cutting process with round tool edge: primary shear zone [GJBTNEQ], secondary shear zone [BCDHJK], tertiary zone [BSAUTP].

The shape of the secondary shear zone is a curvilinear triangle bounded by BJD as shown in Figure 3.1. It is assumed that the material is already strain-hardened; therefore the shear flow stress along each  $\alpha$  slip-line is constant in the secondary shear zone. Zorev [59] proposed that the tool–chip contact consisted of a sticking region and a sliding region. The sticking region is shown as BC and the sliding region is shown as CD in Figure 3.1. The chip sticks to the rake face due to high normal pressure, and the ratio between frictional stress and shear flow stress remains constant in the sticking zone. The chip slides with a constant Coulomb friction coefficient in the sliding zone. The sticking shear stress and friction coefficient are influenced by temperature, tool/work material, and the surface roughness of the rake face. In the tertiary shear zone, S is the separation point with the

material bifurcating upward and downward. The material under point S is compressed to form the finishing surface, which is defined as the ploughing effect. The friction between the workpiece and the tool's round edge AB is assumed to be dominated by sticking contact because of the excessive deformation of material.

The three deformation zones are composed of two families of slip-lines:  $\alpha$  and  $\beta$  lines which are orthogonal to each other. The slip-lines are tangential to the directions of shear stress  $k$  and normal to the directions of hydrostatic pressure  $p$ . The stress Mohr circle at each point in the deformation zone is completely specified if the distributions of  $p$  and  $k$  are obtained. In order to distinguish between  $\alpha$  and  $\beta$  lines, it is defined that the shear stress along the  $\beta$  slip-lines exerts a counter-clockwise couple on the material element bounded by the slip-lines, and the shear stress along the  $\alpha$  slip-lines exerts a clockwise couple on the bounded element, as shown in Figure 3.1. The velocity field in the shear zones is the same as that proposed by Fang [28].

### **3.3 Determination of slip-line field geometry**

Similar to Fang's approach, the slip-line field in the secondary shear zone is solved first by using the matrix operator method developed by Dewhurst and Collins [16] and Dewhurst [60], followed by the slip-lines in the primary and tertiary shear zones which are determined based on the tool edge radius and uncut chip thickness.

#### **3.3.1 Determination of slip-lines in the secondary shear zone**

Figure 3.2 shows the slip-lines of the secondary shear zone BJD. Three geometric parameters determine the shape of the slip-line field: angular range of DH ( $\eta_1$ ), angular range of HJ ( $\eta_2$ ) and the radius ( $R_2$ ) of circular arc BJ with a center  $O_2$ .

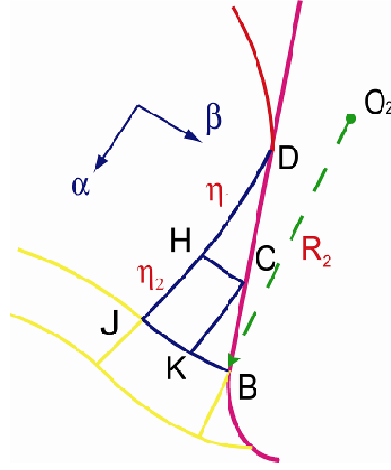


Figure 3.2 Slip-lines in the secondary shear zone.

The angular ranges of the slip-lines in the secondary shear zone are obtained from  $\eta_1$  and  $\eta_2$  based on Hencky's First Theorem [11]. The angular range of BK and KC is equal to  $\eta_2$  because region BKC is formed along the sticking contact boundary BC, and region JHCK is a regular net constructed by four slip-lines KC, KJ, JH, CH. Since region HCD is along the sliding contact boundary CD, the angular range of HC is derived by Dewhurst [60] as:

$$\eta_{CH} = \frac{1+\mu}{1-\mu} \eta_1 \quad (3-1)$$

where  $\mu$  is the coefficient of coulomb friction along CD.

In the regular net JHCK, the angular range of line JK is equal to  $\eta_{CH}$ , therefore, the angular range of line BJ is calculated as:

$$\eta_{BJ} = \eta_{JK} + \eta_{KB} = \frac{1+\mu}{1-\mu} \eta_1 + \eta_2 \quad (3-2)$$

The column vector of line BK and KJ is represented by:

$$\chi_{BK} = \chi_{KJ} = R_2 \cdot e \quad (3-3)$$

where  $e$  represents the column vector of a unit circle and is expressed as:

$$e = [1 \ 0 \ 0 \ \dots]^T \quad (3-4)$$

In region BKC, the column vector of line KC is evaluated as:

$$\chi_{CK} = G_{\angle KCB}^{-1} \cdot \chi_{BK} \quad (3-5)$$

$$\chi_{KC} = R_{\eta_2} \cdot \chi_{CK} \quad (3-6)$$

where

$$\angle KCB = \eta = 0.5 \cos^{-1}(\tau/k) \quad (3-7)$$

$\eta$  is the intersection angle between the slip-line and the rake face in the sticking region, and is determined by the frictional shear stress ( $\tau$ ) along the boundary BC and the material flow stress ( $k$ ) along the  $\alpha$  slip-lines.

The column vectors of slip-lines JH and CH in the region KCHJ are calculated as:

$$\begin{cases} \chi_{CH} = R_{\eta_{CH}} \cdot \chi_{HC} = R_{\eta_{CH}} \cdot (P_{\eta_{KJ}\eta_2} \cdot \chi_{KJ} - Q_{\eta_2\eta_{KJ}} \cdot \chi_{KC}) \\ \chi_{JH} = R_{\eta_2} \cdot \chi_{HJ} = R_{\eta_2} \cdot (P_{\eta_2\eta_{KJ}} \cdot \chi_{KC} - Q_{\eta_{KJ}\eta_2} \cdot \chi_{KJ}) \end{cases} \quad (3-8)$$

where

$$\begin{cases} P_{\eta_{KJ}\eta_2} = R_{\eta_{CH}} P_{\eta_2}^*, & Q_{\eta_2\eta_{KJ}} = R_{\eta_{CH}} Q_{\eta_2}^* \\ P_{\eta_2\eta_{KJ}} = R_{\eta_2} P_{\eta_{KJ}}^*, & Q_{\eta_{KJ}\eta_2} = R_{\eta_2} Q_{\eta_{KJ}}^* \end{cases}$$

In the sliding zone CDH, the column vector of slip-line HD is calculated as:

$$\chi_{HD} = R_{\eta_1} \cdot \chi_{DH} = R_{\eta_1} \cdot L^{-1} \cdot \chi_{CH} \quad (3-9)$$

$G, R, P, P^*, Q, Q^*, L$  in Equations (3-5), (3-6), (3-8) and (3-9) are the matrix operators defined by Dewhurst and Collins [16] and Dewhurst [60].

### 3.3.2 Determination of slip-lines in the tertiary and primary zones

Figure 3.3 shows the slip-lines in the primary and tertiary shear zones. In the region ASU of the tertiary shear zone, line AU is simplified as a straight line. Since sticking contact between the workpiece and the tool is defined along the tool edge ASB due to the large deformation of the material, the intersection angle between line AU and the x-axis is equal to  $\eta$  determined by Equation (3-7). Slip-line SU is perpendicular to line AU due to the orthogonality between  $\alpha$  and  $\beta$  slip-lines.

Coordinate of point S is determined by the material separation angle  $\theta_s$  and position of point A ( $A_x, A_y$ ):

$$\begin{cases} S_x = A_x - r \sin \theta_s \\ S_y = A_y + r \cos \theta_s \end{cases} \quad (3-10)$$

where  $r$  is the tool edge radius.

Then the coordinate of point U ( $U_x, U_y$ ) is calculated from the positions of points A and S shown as:

$$\begin{cases} U_x = \frac{A_x \tan \eta + S_x \cot \eta - A_y + S_y}{\tan \eta + \cot \eta} \\ U_y = \frac{A_y \cot \eta + S_y \tan \eta - A_x + S_x}{\tan \eta + \cot \eta} \end{cases} \quad (3-11)$$

Derivation of point U coordinate is shown in Appendix A (1).

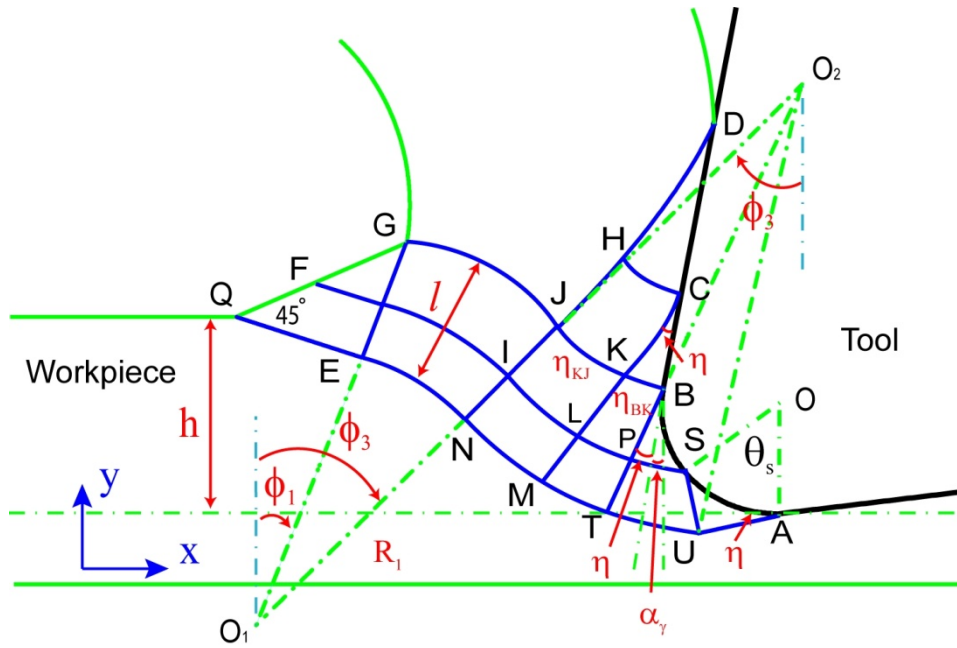


Figure 3.3 Slip-lines in the primary and tertiary shear zones.

Slip-line NU is determined as a circular arc with the radius  $|O_2U|$  and the center  $O_2$ . The inclination angle  $\phi_3$  of  $O_2N$  with respect to the y-axis is calculated from the inclination angle of  $O_2J$  in the secondary shear zone as:

$$\phi_3 = \alpha_\gamma + \eta + \eta_{BK} + \eta_{KJ} \quad (3-12)$$

where  $\alpha_\gamma$  is the rake angle of the tool,  $\eta_{BK}$  and  $\eta_{KJ}$  are the angular ranges of slip-lines BK and KJ calculated in the secondary shear zone.

In the convex region GJNE of the primary shear zone, the inclination angle of EG with respect to the y-axis is given as  $\phi_1$ . The length of line EG represents the thickness of the primary shear zone ( $l$ ) and is equal to the length of line BT which is obtained from the geometry of the tertiary zone. In the pre-flow region QEG, line QE intersects with line QG at an angle of  $45^\circ$ . Lines QE and EG are orthogonal and the lengths are equal to each other. Based on the position of point Q and N, the radius of EN is calculated as:

$$R_1 = \frac{Q_y - N_y - l \sin \phi_1}{\cos \phi_1 - \cos \phi_3} \quad (3-13)$$

where  $Q_y$  and  $N_y$  are the y-coordinates of points Q and N.  $Q_y$  is determined by the uncut chip thickness  $h$ . The detailed procedure to calculate  $R_1$  is shown in Appendix A (2).

Based on the coordinate of point N and the radius of NE, the position of the center point  $O_1$  and the circular arc NE are determined. Point Q is the intersection point between line QE and the upper surface of the workpiece, therefore the x-coordinate of point Q is determined by the inclination angle  $\phi_1$  of line QE with respect to the y-axis as:

$$Q_x = E_x - l \sin \phi_1 \quad (3-14)$$

The circular arc GJ is determined by the position of center point  $O_1$  and the radius  $|O_1J|=R_1+l$ .

After the position of the lower boundary QENMTUA and upper boundary GJKB are obtained in the primary shear zone and tertiary zone, the slip-lines inside all of the zones can be obtained given that the slip-lines in the convex and concave parts are composed of the circular arcs and radial lines with the center points  $O_1$  and  $O_2$ , and the slip-lines in the pre-flow region are straight lines which are parallel to lines QE and EG, respectively.

### 3.4 Stress analysis in the primary shear zone

The stress distribution in the primary shear zone is determined by the geometry of the slip-lines, the material constitutive model, and the cutting conditions. The constitutive model developed by Johnson and Cook [61] is applied to include the strain-hardening,

strain-rate, and thermal softening effects on the flow stress of the material in the primary shear zone, which is expressed as:

$$\sigma = (A + B\varepsilon^n) \left( 1 + C \ln \frac{\dot{\varepsilon}}{\dot{\varepsilon}_0} \right) \left[ 1 - \left( \frac{T - T_r}{T_m - T_r} \right)^m \right] \quad (3-15)$$

where  $A$ ,  $B$  and  $C$  represent the yield strength, strain and strain-rate sensitivities of the material,  $\varepsilon$  is the equivalent plastic strain,  $\dot{\varepsilon}$  and  $\dot{\varepsilon}_0$  are the equivalent and reference plastic strain-rates,  $T$ ,  $T_m$  and  $T_r$  are the material's cutting zone, melting and room temperature, respectively,  $n$  is the strain hardening index, and  $m$  is the thermal softening index.

Figure 3.4 shows the stress-strain curves of brass with different strain-rate values. Effective stress increases significantly with higher strain. Strain-rate has additional hardening effect on the stress. Figure 3.5 shows the stress-strain curves at different temperature values. Effective stress decreases at elevated temperature, indicating the thermal softening effect. Cutting process involves large material deformation in a very short time, and Johnson-Cook constitutive equation is able to explicitly include the strain-hardening, strain-rate and temperature effects in predicting the stress distributions in the material deformation zone.

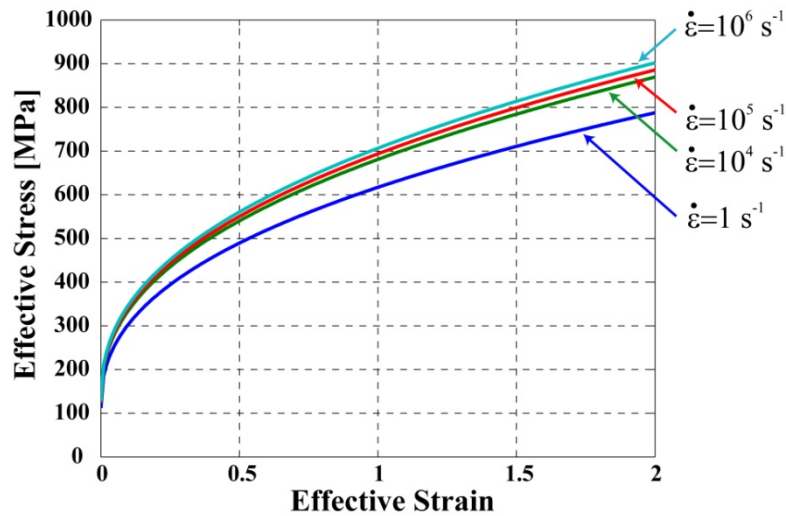


Figure 3.4 Stress-strain curve of brass 260 with different strain-rate values ( $T=20^\circ\text{C}$ ), obtained from the constitutive parameters identified by Johnson and Cook [61].

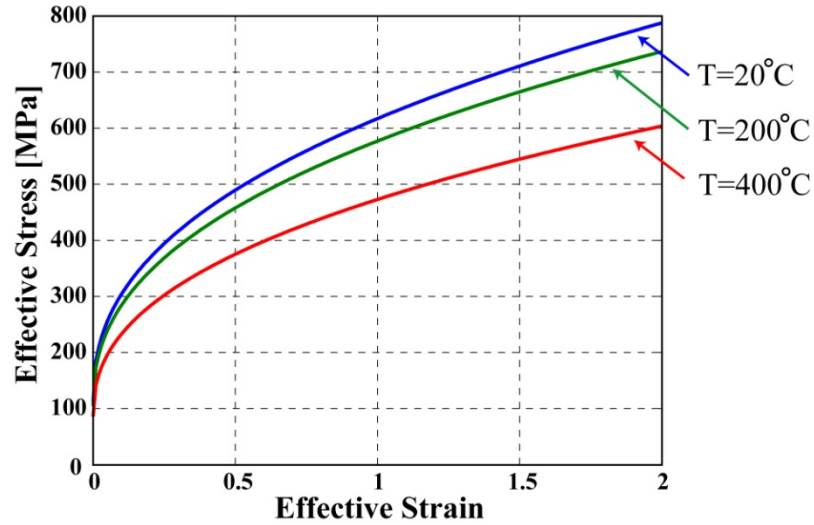


Figure 3.5 Stress-strain curve of brass 260 with different temperature values ( $\dot{\epsilon}=1s^{-1}$ ), obtained from the constitutive parameters identified by Johnson and Cook [61].

The relationships between the effective stress ( $\sigma$ ), strain ( $\epsilon$ ), strain-rate ( $\dot{\epsilon}$ ), shear flow stress ( $k$ ), shear strain ( $\gamma$ ), and shear strain-rate ( $\dot{\gamma}$ ) are given as:

$$\sigma = \sqrt{3}k; \quad \epsilon = \gamma / \sqrt{3}; \quad \dot{\epsilon} = \dot{\gamma} / \sqrt{3} \quad (3-16)$$

Therefore, the distribution of shear strain ( $\gamma$ ), shear strain-rate ( $\dot{\gamma}$ ) and temperature ( $T$ ) in the primary shear zone needs to be modeled in order to show the stress distribution.

### 3.4.1 Shear strain and strain-rate

The polar coordinate  $(\phi, s)$  is set up in the convex and concave regions of the primary shear zone shown in Figure 3.6.  $\phi$  is the inclination angle of each radial line with respect to the y-axis.  $\phi$  increases from  $\phi_1$  to  $\phi_3$  from EG to NJ in the convex region GJNE, and decreases from  $\phi_3$  to  $\phi_2$  from NJ to TB in the concave region NJBT.  $s$  is the radial distance from point  $O_1$  to the point in GJNE of the convex region and from  $O_2$  to the point in NJBT of the concave region.

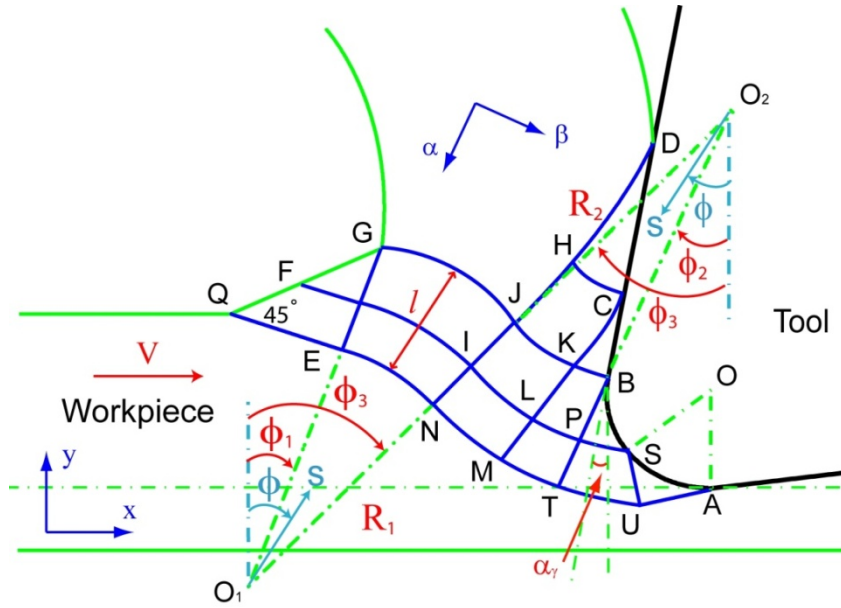


Figure 3.6 Polar coordinate setup in primary shear zone.

The work material enters into the primary shear zone with the velocity  $V$  in the  $x$ -axis direction. Figure 3.7 shows the material velocity vectors at point T and B on the slip-line TB. The resultant velocity at point T is represented by  $\vec{V}_1$ , and the velocity at point B is represented by  $\vec{V}_2$ . The magnitude of  $\vec{V}_1$  is equal to the material velocity  $V$  and can be resolved into two velocity vectors:

$$\vec{V}_1 = \vec{V}_{N1} + \vec{V}_{S1} \quad (3-17)$$

where  $\vec{V}_{S1}$  is the shear velocity with the direction perpendicular to line TB, and  $\vec{V}_{N1}$  is the normal velocity along line TB.

At point B, the velocity of the material is along the tool rake face; therefore, the intersection angle between  $\vec{V}_2$  and the  $y$ -axis is equal to the tool rake angle  $\alpha_\gamma$ .  $\vec{V}_2$  is also resolved into two vectors as shown in Figure 3.7:

$$\vec{V}_2 = \vec{V}_{N2} + \vec{V}_{S2} \quad (3-18)$$

where  $\vec{V}_{S2}$  is perpendicular to line TB and  $\vec{V}_{N2}$  is along line TB.

The shearing of the material takes place in the tangential direction of the  $\beta$  slip-line. Therefore along line TB, the shear velocity changes while the normal velocity remains

constant and is expressed as:

$$\vec{V}_{N1} = \vec{V}_{N2} \quad (3-19)$$

Then the velocity transition from point T to point B is derived as:

$$\vec{V}_t = \vec{V}_2 - \vec{V}_1 = \vec{V}_{S2} - \vec{V}_{S1} \quad (3-20)$$

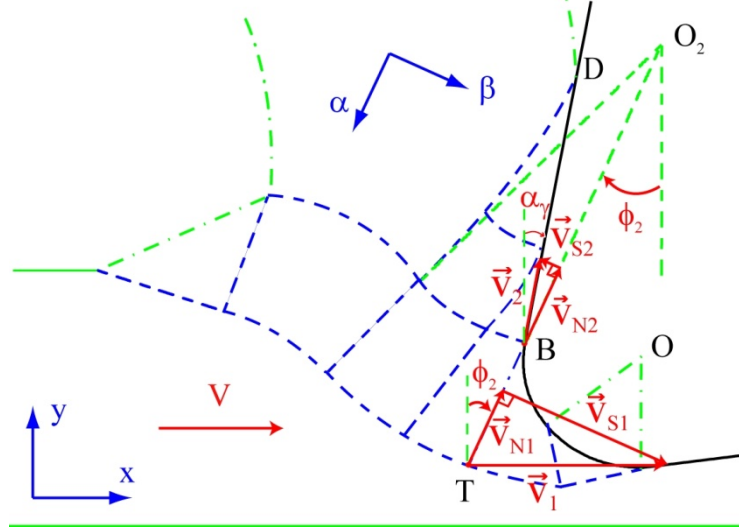


Figure 3.7 Velocity variation along slip-line TB.

It can be obtained from Figure 3.7 that:

$$\begin{cases} |\vec{V}_{S1}| = V \cos \phi_2 \\ |\vec{V}_{N1}| = V \sin \phi_2 \\ |\vec{V}_{S2}| = |\vec{V}_{N2}| \tan(\phi_2 - \alpha_\gamma) = V \sin \phi_2 \tan(\phi_2 - \alpha_\gamma) \end{cases} \quad (3-21)$$

The magnitude of the velocity transition  $\vec{V}_t$  in (3-20) is calculated as:

$$V_t = |\vec{V}_{S1}| + |\vec{V}_{S2}| = V \cos \phi_2 + V \sin \phi_2 \tan(\phi_2 - \alpha_\gamma) \quad (3-22)$$

where  $\alpha_\gamma$  is the tool rake angle,  $\phi_2$  is the inclination angle of slip-line TB with respect to the y-axis, which is calculated as:

$$\phi_2 = \eta + \alpha_\gamma \quad (3-23)$$

where  $\eta$  is calculated in the sticking region BC from Equation (3-7).

The magnitude of total velocity transition along each  $\alpha$  slip-line in primary shear zone is the same as line TB. However, the directions of velocity transition change gradually from

line TB to line EG because they are always perpendicular to the  $\alpha$  slip-lines. In Figure 3.8, the vector  $\vec{V}$  is the resultant velocity at point T, N, E, and  $\vec{V}_1, \vec{V}_2, \vec{V}_3,$  are the resultant velocities at point G, B, J. The velocity transition vectors  $\vec{V}_{t1}, \vec{V}_{t2}, \vec{V}_{t3}$  along slip-lines EG, TB, NJ have the same magnitude  $V_t$ . However, the vectors are in different directions.

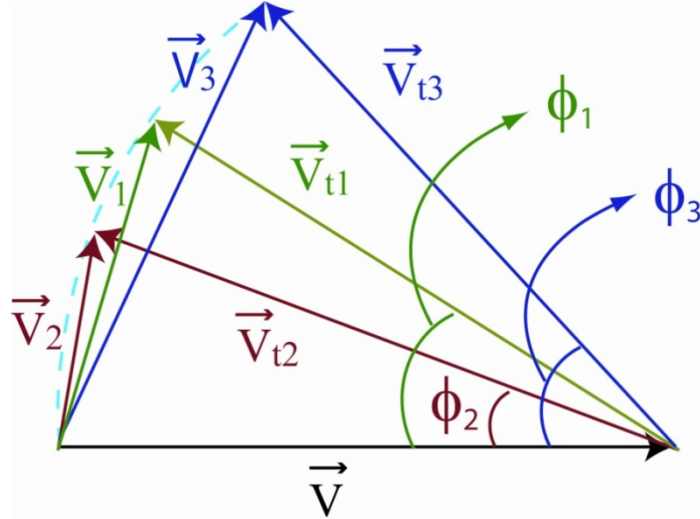


Figure 3.8 Velocity transition along the  $\alpha$  slip-lines in primary shear zone.

Along each  $\alpha$  slip-line with the angular coordinate of  $\phi$  in the convex and concave regions, the normal velocity is parallel to the  $\alpha$  slip-line and the magnitude is calculated from Figure 3.7 as:

$$|\vec{V}_N| = V \sin \phi \quad (3-24)$$

The initial shear velocity at the lower boundary QENMT in Figure 3.6 is perpendicular to the  $\alpha$  slip-line and the magnitude is:

$$|\vec{V}_S| = V \cos \phi \quad (3-25)$$

Based on the investigation of Kushnir [62] and Astakhov [63], the shear velocity variation along the  $\alpha$  slip-lines can be calculated by the initial shear velocity  $|\vec{V}_S|$  and magnitude of the velocity transition  $V_t$ , and is expressed as a power function with respect to the radial coordinate  $S$ :

$$\begin{cases} V_s(\phi, s) = V \cdot \cos \phi - V_t \cdot \left( \frac{s - R_1}{l} \right)^q & \text{(Convex Region) } (R_1 \leq s \leq R_1 + l) \\ V_s(\phi, s) = V \cdot \cos \phi - V_t \cdot \left( \frac{R_2 + l - s}{l} \right)^q & \text{(Concave Region) } (R_2 \leq s \leq R_2 + l) \end{cases} \quad (3-26)$$

where  $R_1$  is the radius of the slip-line EN in the convex region,  $R_2$  is the radius of the slip-line JB in the concave region,  $l$  is the thickness of the primary shear zone, index  $q$  determines the characterization of the distribution of the shear velocity along the  $\alpha$  slip-lines.

Based on the shear and normal velocity distribution, the shear strain-rate in the direction of the  $\beta$  slip-line is obtained by the differentiation of shear velocity  $V_s$  with respect to the distance traveled in the normal direction. Therefore, the shear strain-rate in the shear zone is derived as:

$$\begin{cases} \dot{\gamma}(\phi, s) = \left| \frac{dV_s}{ds} \right| = V_t \frac{q}{l} \left( \frac{s - R_1}{l} \right)^{q-1} & \text{(Convex Region) } (R_1 \leq s \leq R_1 + l) \\ \dot{\gamma}(\phi, s) = \left| \frac{dV_s}{ds} \right| = V_t \frac{q}{l} \left( \frac{R_2 + l - s}{l} \right)^{q-1} & \text{(Concave Region) } (R_2 \leq s \leq R_2 + l) \end{cases} \quad (3-27)$$

The shear strain of the material is zero at the lower boundary slip-line QENMT in the primary shear zone, and accumulates along the  $\alpha$  slip-lines toward the upper boundary GJKB. By integrating the shear strain-rate along the  $\alpha$  slip-line, the shear strain in the primary shear zone is derived as:

$$\begin{cases} \gamma(\phi, s) = \int_{R_1}^s \dot{\gamma}(\phi, s) \frac{ds}{V_N(\phi, s)} = \frac{V_t}{V \sin \phi} \left( \frac{s - R_1}{l} \right)^q & \text{(Convex Region) } (R_1 \leq s \leq R_1 + l) \\ \gamma(\phi, s) = \int_{R_2+l}^s \dot{\gamma}(\phi, s) \frac{ds}{V_N(\phi, s)} = \frac{V_t}{V \sin \phi} \left( \frac{R_2 + l - s}{l} \right)^q & \text{(Concave Region) } (R_2 \leq s \leq R_2 + l) \end{cases} \quad (3-28)$$

Equations (3-27) and (3-28) show that the magnitude of the shear strain-rate and shear strain is affected by the cutting velocity ( $V$ ), the tool-chip contact condition in the secondary shear zone ( $\eta$ ), and the thickness of the primary shear zone ( $l$ ).

In the pre-flow region QEG, all of the  $\alpha$  slip-lines have the same inclination angle as line EG, therefore, the shear strain-rate and strain remain constant along each  $\beta$  slip-line in

region QEG.

### 3.4.2 Temperature distribution

The temperature distribution in the shear zone is determined by the shear-strain and shear strain-rate distribution. At each point in the primary shear zone, the plastic work contributed by an infinitesimal strain increase  $d\varepsilon$  is:

$$\beta_T \sigma d\varepsilon = \rho c_s dT \quad (3-29)$$

where  $c_s$  is the specific heat,  $\rho$  is the specific density, and  $\beta_T$  is the fraction of the plastic work contributing to the temperature increase and assumed to be 0.9 in the model. By substituting the Johnson-Cook model (Equation (3-15)) into Equation (3-29), the thermal energy which results in the temperature increase is:

$$\beta_T \left( 1 + C \ln \frac{\dot{\varepsilon}}{\dot{\varepsilon}_0} \right) (A + B\varepsilon^n) d\varepsilon = \frac{\rho c_s}{1 - \left( \frac{T - T_r}{T_m - T_r} \right)^m} dT \quad (3-30)$$

By integrating both sides of the Equation (3-30), and imposing the room temperature  $T_r$  as the boundary condition, it is derived that:

$$\int_{T_r}^T \frac{\rho c_s}{1 - \left( \frac{T - T_r}{T_m - T_r} \right)^m} dT = \beta_T \left( 1 + C \ln \frac{\dot{\varepsilon}}{\dot{\varepsilon}_0} \right) \left( A\varepsilon + \frac{1}{n+1} B\varepsilon^{n+1} \right) \quad (3-31)$$

The integration is carried out numerically to calculate the temperature since there is no explicit expression for the left side of Equation (3-31).

### 3.4.3 Shear flow stress and hydrostatic pressure

The shear flow stress is evaluated from Equations (3-15) and (3-16) based on the shear strain, strain-rate, and temperature distribution:

$$k = \sigma / \sqrt{3} = \frac{1}{\sqrt{3}} \left[ A + B \left( \gamma / \sqrt{3} \right)^n \right] \left[ 1 + C \ln \left( \dot{\gamma} / \sqrt{3} \right) \right] \left[ 1 - \left( \frac{T - T_r}{T_m - T_r} \right)^m \right] \quad (3-32)$$

Based on the equilibrium equations in the absence of body forces under plane strain condition, the relationship between the hydrostatic pressure and the shear flow stress is expressed as:

$$\begin{cases} \frac{\partial p}{\partial \alpha} + 2k \frac{\partial \psi}{\partial \alpha} - \frac{\partial k}{\partial \beta} = 0 & \text{(Along } \alpha \text{ slip-line)} \\ \frac{\partial p}{\partial \beta} - 2k \frac{\partial \psi}{\partial \beta} - \frac{\partial k}{\partial \alpha} = 0 & \text{(Along } \beta \text{ slip-line)} \end{cases} \quad (3-33)$$

where  $\partial \alpha$  and  $\partial \beta$  are the infinitesimal distances along slip-lines  $\alpha$  and  $\beta$ , respectively,  $\psi$  is the inclination angle of  $\alpha$  slip-line with respect to the x-axis.

Figure 3.9 shows the Cartesian coordinate of any point W in the convex and concave regions, the polar coordinate  $(\phi, s)$  and the directions of  $\alpha$  and  $\beta$  slip-lines. The infinitesimal distance along  $\alpha$  and  $\beta$  slip-lines and the rotation angle of  $\alpha$  slip-line are expressed as:

$$\begin{cases} \partial \alpha = -\partial s; & \partial \beta = s \cdot \partial \phi; & \partial \phi = -\partial \psi & \text{(Convex Region)} \\ \partial \alpha = \partial s; & \partial \beta = -s \cdot \partial \phi; & \partial \phi = -\partial \psi & \text{(Concave Region)} \end{cases} \quad (3-34)$$

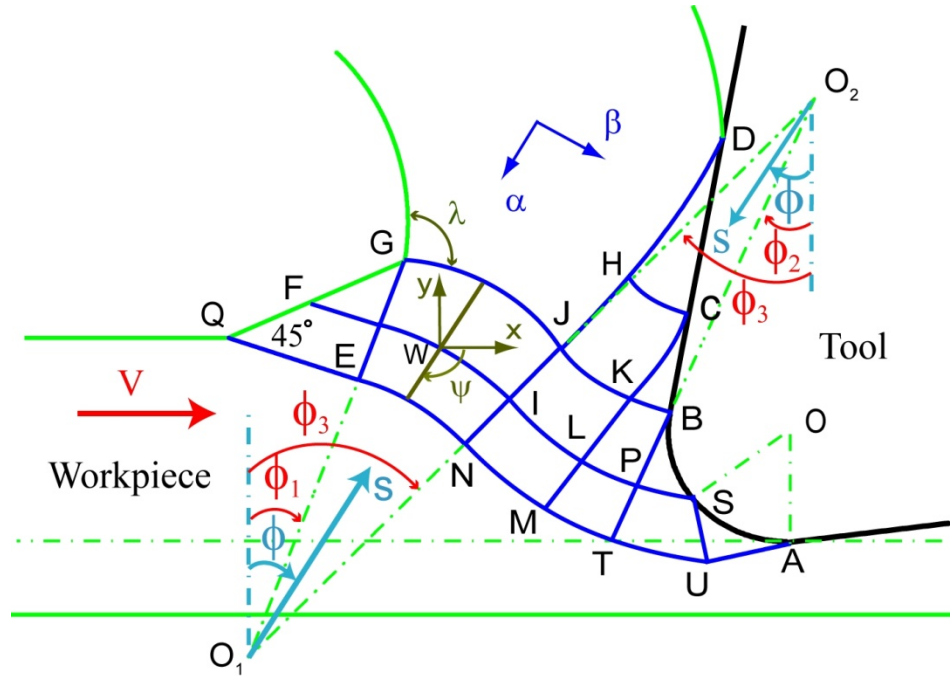


Figure 3.9 Calculation of hydrostatic pressure in the primary shear zone.

From Equations (3-33) and (3-34), the stress equilibrium equation is derived as:

$$\frac{\partial p(\phi, s)}{\partial \phi} = -2k(\phi, s) - s \cdot \frac{\partial k(\phi, s)}{\partial s} \quad (3-35)$$

for both the convex and concave regions. Equation (3-35) indicates that the distribution of

hydrostatic pressure in the shear zone is influenced by the variation of shear flow stress along the direction of the  $\alpha$  slip-line.

Based on the overstressing theory developed by Hill [64], the rigid vertex G between the slip-line field and the free chip surface should not be overstressed, which is expressed mathematically as:

$$1+2(\lambda-\pi/4) \geq p_G/k_G \geq -1+2\cos(\lambda-\pi/4) \quad (3-36)$$

where  $\lambda$  is the angle between the slip-line GJ and the back surface of the chip in Figure 3.9, and  $\lambda$  satisfies the condition that:

$$3\pi/4 \geq \lambda \geq \pi/4 \quad (3-37)$$

The convex and concave regions are divided into small elements in order to calculate the distribution of the hydrostatic pressure. In the model, the radial lines are divided into 100 elements and the circular arcs are divided into 500 elements uniformly. The stress distribution along EG is calculated by applying Equation (3-33) along line EG:

$$\left. \frac{\partial p}{\partial s} + \frac{\partial k}{\partial \phi} \right|_{\phi_2} \cdot \frac{1}{s} = 0 \quad (3-38)$$

The partial differentiation of the equation is approximated as:

$$\frac{\Delta p}{\Delta s} + \left. \frac{\partial k}{\partial \phi} \right|_{\phi_2} \cdot \frac{1}{s} = 0 \quad (3-39)$$

where the radial increment  $\Delta s$  is selected as  $\Delta s = l/100$ ,  $\Delta p$  is the difference of hydrostatic pressure between two neighboring elements along GE,  $\Delta s$  is the radial length of each element. The derivation of  $\partial k / \partial \phi$  is shown in Appendix B. The hydrostatic pressure of each element along GE is calculated recursively from point G to point E.

The hydrostatic pressure distribution in the convex and concave regions is obtained by approximating Equation (3-35) as:

$$\frac{\Delta p(\phi, s)}{\Delta \phi} = -2k(\phi, s) - s \cdot \frac{\partial k(\phi, s)}{\partial s} \quad (3-40)$$

where the angular span of the convex and concave regions is divided into 500 differential

elements as  $\Delta\phi=(\phi_3-\phi_1)/500$  for the convex region and  $\Delta\phi=(\phi_3-\phi_2)/500$  for the concave region.  $\Delta p$  is the difference of hydrostatic pressure, and  $\Delta\phi$  is the intersection angle between two neighboring radial lines in the primary shear zone. The derivation of  $\partial k(\phi,s)/\partial s$  is shown in Appendix B. The distribution of hydrostatic pressure along each radial line is obtained recursively starting from line EG to line TB in Equation (3-40).

### 3.5 Identification of slip-line parameters

There are four geometric parameters used to determine the shape of the slip-line field as shown in Figure 3.10: angle ranges of slip-line DH ( $\eta_1$ ) in the sticking and HJ ( $\eta_2$ ) in the sliding contact region, the radius of the slip-line BJ ( $R_2$ ), and the inclination angle of line EG with respect to the y-axis ( $\phi_1$ ) in the pre-flow region. The stress distribution in the primary shear zone and along the tool edge is influenced by the hydrostatic pressure at point G ( $p_G$ ) and the tool-chip contact parameters ( $\tau/k$  &  $\mu$ ), therefore, the hydrostatic pressure at point G and the tool-chip contact parameters need to be identified.

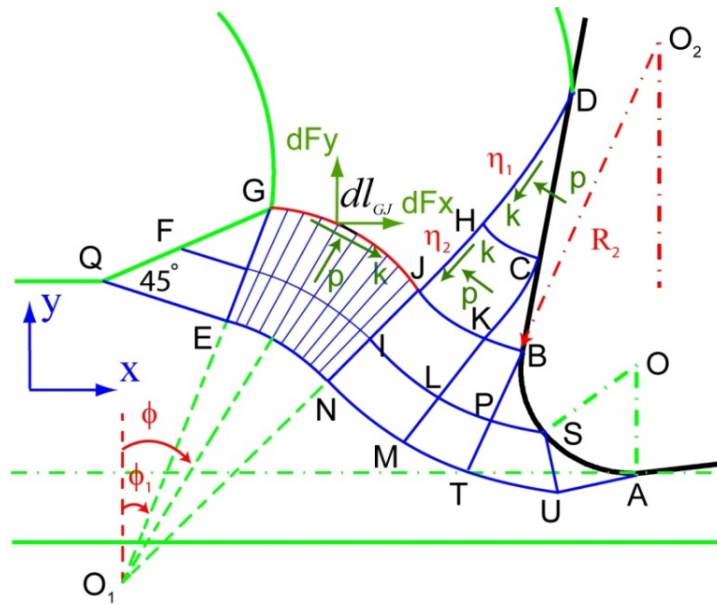


Figure 3.10 Identification of parameters in the slip-line field model.

Since the chip freely curls back after the material passes through the shear zones, the resultant force along the slip-lines that form the chip boundary should be zero (GJ, JH, HD).

The stress distribution along the chip boundary slip-lines is obtained from the stress analysis of the primary and secondary shear zones. The directions of the stresses are shown in Figure 3.10. The distribution of hydrostatic pressure and shear flow stress along slip-line GJ is calculated by dividing GJ into 500 differential elements, then the forces in the X and Y directions on each element of GJ are calculated as:

$$\begin{cases} dF_x = (p \cdot \sin \phi + k \cdot \cos \phi) \cdot dl_{GJ} \cdot w \\ dF_y = (p \cdot \cos \phi - k \cdot \sin \phi) \cdot dl_{GJ} \cdot w \end{cases} \quad (3-41)$$

where  $p$  is the hydrostatic pressure and  $k$  is the shear flow stress on the element,  $\phi$  is the angular coordinate of the element shown in Figure 3.10,  $w$  is the width of cut, and  $dl_{GJ}$  is the length of the element which is calculated by:

$$dl_{GJ} = l_{GJ} / 500 \quad (3-42)$$

The total force along GJ is obtained by summing up all of the elemental forces in the X and Y directions. The force along slip-line JH is calculated based on the force calculation procedure by Johnson et al. [11] which is based on the hydrostatic pressure  $p_J$  and shear flow stress  $k_J$  of point J. After the total forces along slip-line GJ, JH and HD are calculated, the force constraint which the model parameters need to satisfy is expressed as:

$$\begin{cases} F_{xGJ} + F_{xJH} + F_{xHD} = 0 \\ F_{yGJ} + F_{yJH} + F_{yHD} = 0 \end{cases} \quad (3-43)$$

Based on the geometry of the slip-line field, the chip thickness can be obtained by measuring the distance from point B to point G in Figure 3.10. The predicted chip thickness will also be compared to the experimental results in order to identify the tool-chip contact parameters.

The location of material stagnation point needs to be identified to determine the range of ploughing region. Since slip-line field theory is based on the continuum-plasticity theory, the FE method is used to identify the separation angle, and is subsequently used in the slip-line field model. FE modeling procedure and the identification of material separation point is explained in detail in Section 4.2.4.

The flow chart of the model's parameter identification and cutting force prediction is shown in Figure 3.11:

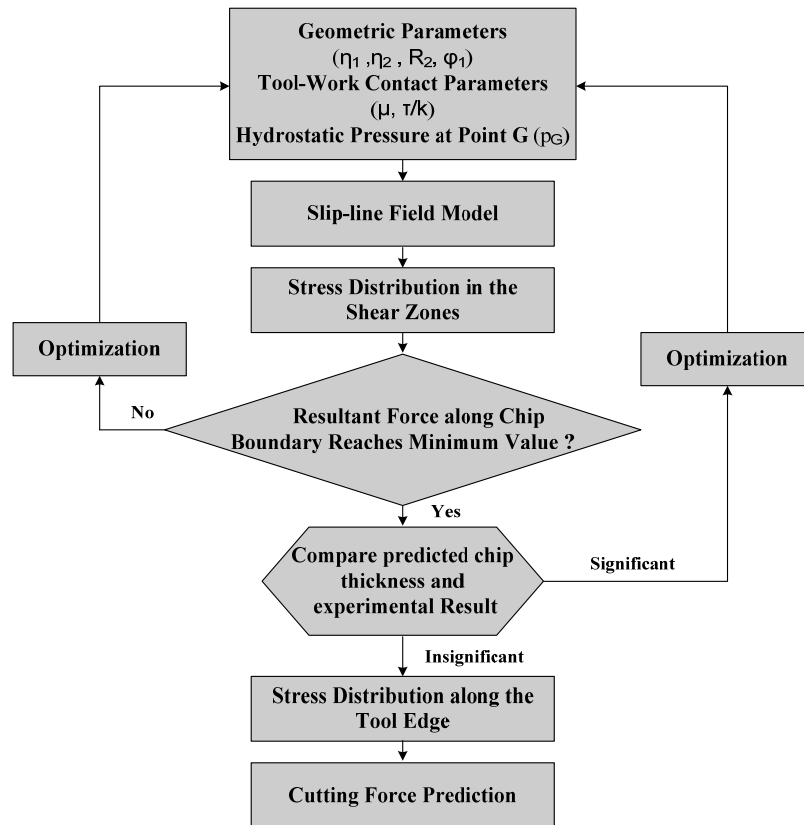


Figure 3.11 Flow chart of parameter identification and cutting force prediction.

## 3.6 Prediction of cutting forces

The cutting force is predicted by evaluating the total force along the tool edge in the tangential and feed direction, which is determined by the normal and shear stress distribution along the boundary lines DC, CB, BS, and SA in Figure 3.9. Since DC and CB are in the secondary shear zone, and BS and SA are in the tertiary shear zone, the shear flow stress and hydrostatic pressure have to be modeled in the secondary and tertiary shear zones based on the slip-line geometry and the stress distribution in the primary shear zone.

### 3.6.1 Stress analysis in the secondary shear zone

Slip-line BJ is divided into 500 angular elements in the primary shear zone. By generating the slip-line from each element of line BJ, 500  $\alpha$  slip-lines are formed in the secondary shear zone. For any  $\alpha$  slip-line YZ in Figure 3.12-(a), the hydrostatic pressure  $p_Y$

and shear flow stress  $k_Y$  at point Y are obtained from the stress distribution in the primary shear zone. The angular range  $\eta_3$  of slip-line BY is calculated as:

$$\eta_3 = \eta_{BJ} \cdot l_{BY} / l_{BJ} \quad (3-44)$$

where  $l_{BY}$  and  $l_{BJ}$  are the lengths of BY and BJ, and  $\eta_{BJ}$  is the angular range of line BJ which is derived from Equation (3-2).

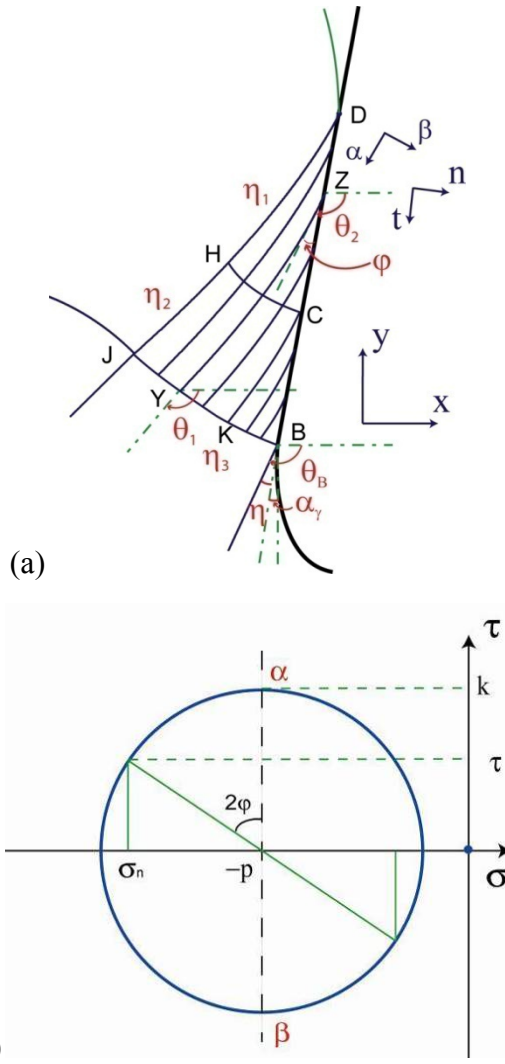


Figure 3.12 Stress analysis in the secondary shear zone.

Since line YZ is perpendicular to line BJ at point Y, the inclination angle of line YZ with respect to the x-axis at point Y is:

$$\theta_1 = \theta_B - \eta_3 = -\pi/2 - \alpha_\gamma - \eta - \eta_3 \quad (3-45)$$

where  $\theta_B$  is the inclination angle of the  $\alpha$  slip-line with respect to the x-axis at point B,  $\eta$  is

the intersection angle between the  $\alpha$  slip-line and tool rake face in the sticking region which is derived from Equation (3-7).

The inclination angle of line YZ with respect to the x-axis at point Z is calculated as:

$$\theta_2 = -\pi/2 - \alpha_\gamma - \varphi \quad (3-46)$$

where  $\varphi$  is the intersection angle between the slip-line and the tool rake face. In the sticking region BC,  $\varphi$  is equal to  $\eta$ ; in the sliding region CD,  $\varphi$  is derived based on the definition of matrix operator  $L$  in Equation (3-9) developed by Dewhurst [60]:

$$\varphi = \eta + \eta_{KY} \frac{2\mu}{1+\mu} = \eta + (\eta_3 - \eta_2) \frac{2\mu}{1+\mu} \quad (3-47)$$

where  $\eta_{KY}$  is the angular range of line KY.

In the secondary shear zone, it is assumed that the shear flow stress along each  $\alpha$  slip-line remains constant since the material is already strain-hardened after the deformation in the primary shear zone. Also, the thermal effect is neglected in the calculation of the hydrostatic pressure distribution along the  $\alpha$  slip-line. Based on Hencky's Equation, the relationship between the hydrostatic pressure and the shear flow stress along  $\alpha$  slip-line is expressed as:

$$p + 2k\theta = \text{constant} \quad (3-48)$$

where  $\theta$  is the inclination angle of the  $\alpha$  slip-line with respect to the x-axis. Therefore, the shear flow stress and hydrostatic pressure at point Z is calculated as:

$$\begin{cases} k_Z = k_Y \\ p_Z = p_Y + 2k_Y(\theta_1 - \theta_2) \end{cases} \quad (3-49)$$

From the Mohr circle shown in Figure 3.12-(b), the normal and shear stress on the rake face at point Z is obtained as:

$$\begin{cases} \sigma_{nZ} = -p_Z - k_Z \sin(2\varphi) \\ \tau_Z = k_Z \cos(2\varphi) \end{cases} \quad (3-50)$$

Then the elemental force normal and tangential to the tool rake face is:

$$\begin{cases} dF_{nZ} = \sigma_{nZ} \cdot l_{BD} / 500 \cdot w \\ dF_{\tau Z} = \tau_Z \cdot l_{BD} / 500 \cdot w \end{cases} \quad (3-51)$$

where  $l_{BD}/500$  is the length of each element,  $w$  is the width of cut.

The elemental force is projected into the x and y directions, and then the elemental forces in the x and y directions at point Z are:

$$\begin{cases} dF_{xZ} = dF_{nZ} \cos \alpha_\gamma - dF_{\tau Z} \sin \alpha_\gamma \\ dF_{yZ} = -dF_{nZ} \sin \alpha_\gamma - dF_{\tau Z} \cos \alpha_\gamma \end{cases} \quad (3-52)$$

The elemental force at other points along the tool rake face BD is calculated following the same procedure as point Z, and then the total force along BD is obtained by summing up all of the elemental force in the X and Y directions.

### 3.6.2 Stress analysis in the tertiary shear zone

Line BT is divided into 100 small elements in the stress analysis of the primary shear zone; therefore, 100  $\beta$  slip-lines are generated from line BT toward the tool edge BA in the tertiary shear zone. Due to the bifurcation of the material at point S, the direction of shear stress along SB is tangential to the tool edge from S to B, and the direction of shear stress along SA is from S to A. From Figure 3.13-(a), the intersection angle between the  $\alpha$  slip-line and the tangential direction of tool edge is  $\eta$  in region SPB, and the intersection angle between  $\beta$  slip-line and the tangential direction of tool edge is  $\eta$  in region ASU. Since the sticking contact is defined along the tool edge,  $\eta$  is equal to the angle calculated in Equation (3-7) in the sticking region of the secondary shear zone.

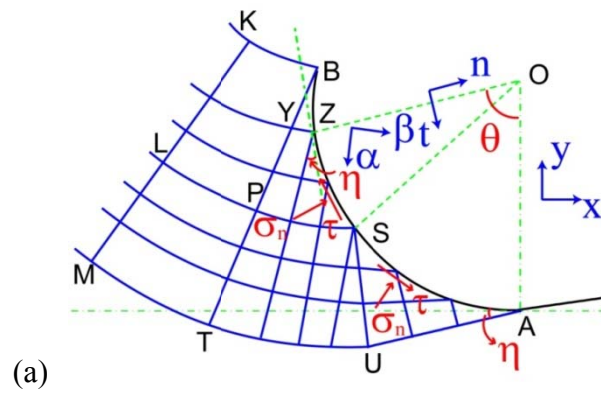
For each  $\beta$  slip-line YZ in the tertiary shear zone, the inclination angle of the slip-line with respect to the x-axis at point Y is:

$$\theta_1 = -\phi_2 \quad (3-53)$$

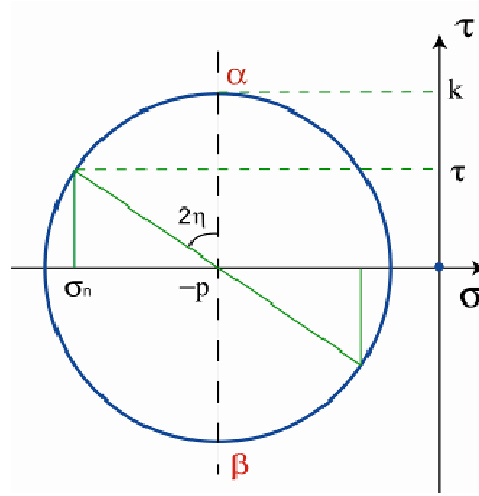
The inclination angle of the  $\beta$  slip-line with respect to the x-axis at point Z is:

$$\theta_2 = \pi/2 - \theta - \eta \quad (3-54)$$

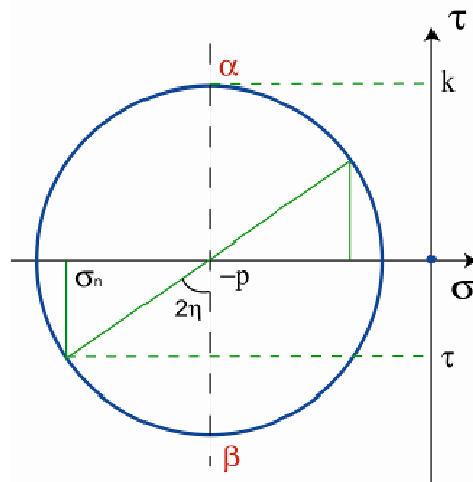
where  $\theta$  is the intersection angle between line OZ and OA.



(a)



(b)



(c)

Figure 3.13 Stress analysis in the tertiary shear zone.

By assuming that the shear flow stress along the  $\beta$  slip-line remains constant, the relationship between the hydrostatic pressure and the shear flow stress along the  $\beta$  slip-line is expressed by Hencky's Equation:

$$p - 2k\theta = \text{constant} \quad (3-55)$$

Therefore, the hydrostatic pressure at point Z is calculated as:

$$\begin{cases} k_z = k_y \\ p_z = p_y - 2k_y(\theta_1 - \theta_2) \end{cases} \quad (3-56)$$

Figure 3.13-(b) shows the stress Mohr circle along SB and Figure 3.13-(c) shows the stress Mohr circle along SA, then the normal and shear stress along the round edge is obtained as:

$$\begin{cases} \sigma_n = -p - k \sin(2\eta) \\ \tau = k \cos(2\eta) \end{cases} \quad \text{along edge SB} \quad (3-57)$$

$$\begin{cases} \sigma_n = -p - k \sin(2\eta) \\ \tau = -k \cos(2\eta) \end{cases} \quad \text{along edge SA} \quad (3-58)$$

where  $p$  and  $k$  are the hydrostatic pressure and the shear flow stress of one element on the tool edge.

The elemental force normal and tangential to the tool edge is:

$$\begin{cases} dF_n = \sigma_n \cdot l_{AB} / 100 \cdot w \\ dF_\tau = \tau \cdot l_{AB} / 100 \cdot w \end{cases} \quad (3-59)$$

where  $l_{AB}$  is the length of the circular arc AB.

By projecting the elemental force into the x and y directions, the elemental force in the x and y directions is:

$$\begin{cases} dF_x = dF_n \sin \theta - dF_\tau \cos \theta \\ dF_y = dF_n \cos \theta + dF_\tau \sin \theta \end{cases} \quad \text{along line SB} \quad (3-60)$$

$$\begin{cases} dF_x = dF_n \sin \theta + dF_\tau \cos \theta \\ dF_y = dF_n \cos \theta - dF_\tau \sin \theta \end{cases} \quad \text{along line SA} \quad (3-61)$$

The total force along tool edge AB is obtained by summing up all of the elemental forces along SB and SA in the X and Y directions.

The total tangential ( $F_t$ ) and feed ( $F_f$ ) cutting force is calculated by adding all of the forces along the tool rake face and round edge:

$$\begin{cases} F_t = F_{xDC} + F_{xCB} + F_{xBS} + F_{xSA} \\ F_f = F_{yDC} + F_{yCB} + F_{yBS} + F_{ySA} \end{cases} \quad (3-62)$$

## 3.7 Experimental validation by micro-turning

### 3.7.1 Experimental conditions

A series of turning tests have been performed on MIKROTOOL micro-machining center. A brass bar (Alloy 260) with a 6 mm diameter was turned along a longitudinal direction with a SANDVIK Carbide insert (TCGT110201-UM) as shown in Figure 3.14 - a. The hardness of the workpiece was measured to be 77 HRB, and the tool rake angle was 5°. The cutting edge radius of the tool was measured by fitting a circle into the SEM image of the tool cutting edge (Figure 3.14-b), and the edge radius was measured to be 20  $\mu\text{m}$  for the first set of experiments. The turning tool holder was clamped on a Kistler Type 9256 three component mini-dynamometer to measure the cutting forces. The chips were collected and their thickness was measured.

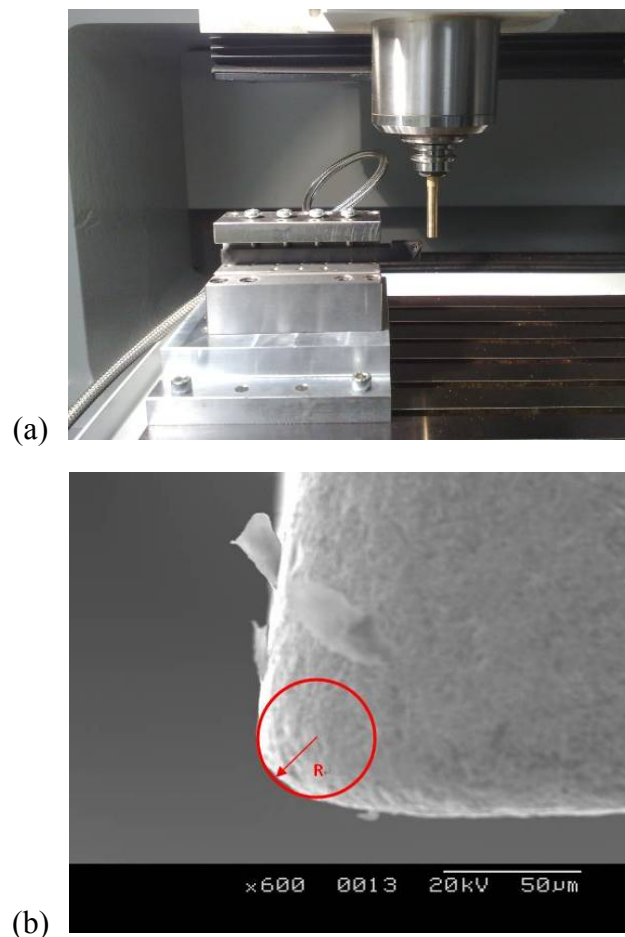


Figure 3.14 (a) Setup for microturning experiment; (b) SEM image of the cutting edge.

The uncut chip thickness was selected to be comparable with the tool edge radius, and a range of cutting speed (150 m/min – 350 m/min) was tried to investigate its effect on the process, see Table 3.1.

Table 3.1 Cutting conditions of micro-turning experiment.

Cutting Test	Width of Cut (mm)	Uncut Chip Thickness ( $\mu\text{m}$ )	Cutting Speed (m/min)
1	0.1	15, 17, 19, 21, 23, 25, 30, 40, 50, 60, 70, 80	200
2	0.3	15, 17, 19, 21, 23, 25, 30, 40, 50, 60, 70, 80	200
3	0.5	15, 17, 19, 21, 23, 25, 30, 40, 50, 60, 70, 80	200
4	0.1	21	150, 200, 250, 300, 350
5	0.3	21	150, 200, 250, 300, 350

Identification of the flow stress parameters in Johnson-Cook equation (3-15) requires the split-Hopkinson bar test data at various strains, strain-rates, and temperatures. Since the instruments for this test are not available in this thesis, the parameters are borrowed from Johnson and Cook for material brass 260 [61], and the coefficients  $A$ ,  $B$ ,  $C$ ,  $n$ ,  $m$  and  $T_m$  are listed in Table 3.2.

Table 3.2 Johnson-Cook parameters for brass 260 [61].

Material	$A$ [MPa]	$B$ [MPa]	$C$ [-]	$n$ [-]	$m$ [-]	$T_m$ [ $^{\circ}\text{C}$ ]
Brass	112	505	0.009	0.42	1.68	916

The SEM image of the tool cutting edge after the cutting process with  $w = 0.5$  mm width of cut,  $V = 200$  m/min cutting speed and  $h = 25$   $\mu\text{m}$  uncut chip thickness is shown in Figure 3.15. The observed material on the cutting edge confirms the assumption of sticking contact between tool and workpiece at the tool round edge.

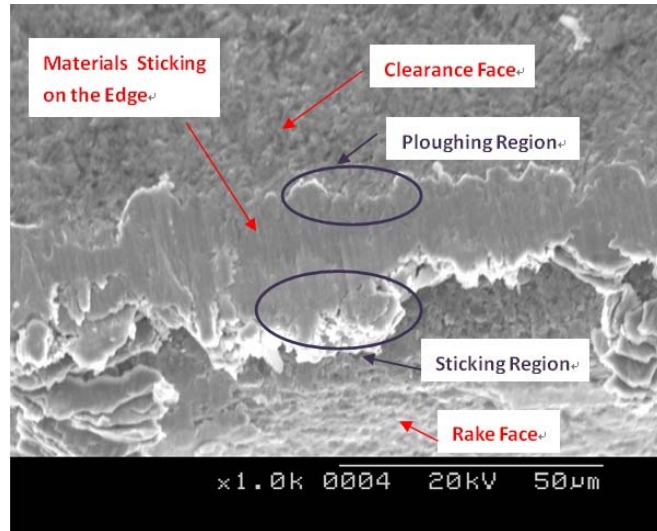


Figure 3.15 SEM image of the material on the cutting edge.

In order to identify the shear stress ratio ( $\tau/k$ ) in the sticking region, and the coulomb friction coefficient  $\mu$  in the sliding region, the thickness of the cut chips were measured at several locations of the chip under the optical microscope at the cutting speed  $V = 200$  m/min. The model assumes that the friction parameters don't change with the cutting speeds. The mean values of the chip thickness for each uncut chip thickness are listed in Table 3.3.

Table 3.3 Chip thickness measurement for carbide tool with 20  $\mu\text{m}$  edge radius.

Uncut Chip Thickness ( $\mu\text{m}$ )	15	17	19	21	23	25	40	60	80
Chip Thickness ( $\mu\text{m}$ )	38.6	43.5	46.0	52.5	58.9	61.5	110	161	217

The parameter identification procedure is based on the flow chart in Figure 3.11. The Matlab<sup>®</sup> function “fmincon” [65] is applied in the optimization process with the following objective constraint:

$$\begin{cases} F_{xGJ} + F_{xJH} + F_{xHD} < 10^{-3} (N) \\ F_{yGJ} + F_{yJH} + F_{yHD} < 10^{-3} (N) \\ \kappa - \kappa_E < 0.01 \end{cases} \quad (3-63)$$

where  $\kappa$  is the predicted chip ratio, and  $\kappa_E$  is the measured chip ratio from the experiment. By averaging the shear stress ratios and the coulomb friction coefficients identified from

the three cutting conditions respectively, it is obtained that:

$$\begin{cases} \tau / k = 0.95 \\ \mu = 0.15 \end{cases} \quad (3-64)$$

By applying the identified tool-chip contact condition, the geometric parameters and the hydrostatic pressure at point G are identified based on the first two parts of Equation (3-63) as the optimization objective.

The material separation angle, which determines the cutting and ploughing region, is identified to be  $56^\circ$  by FE simulation for turning brass with the carbide tool with an edge radius of  $20 \mu\text{m}$ . The FE modeling procedure is described in Section 4.2.4. The variation of the separation angle is found to be less than  $\pm 1^\circ$  when the uncut chip thickness changes between  $15 \mu\text{m}$  to  $25 \mu\text{m}$  and the cutting speed varies from  $150 \text{ m/min}$  to  $350 \text{ m/min}$ ; therefore, a constant separation angle of  $56^\circ$  is considered in the slip-line field model for this tool. Simulation and experimental results of Woon et al. [37] showed that the stagnation angle at the tool round edge was in the range of  $58.5 \pm 0.5^\circ$ , and was not sensitive to the change of uncut chip thickness for the tool with a  $10 \mu\text{m}$  edge radius. The parameter  $q$  in Equation (3-26) is considered to be unity ( $q = 1$ ) for linear distribution of shear strain (Equation (3-28)) with constant strain rate (Equation (3-27)) in the primary shear zone.

### 3.7.2 Experimental comparisons

The experimentally measured tangential and feed forces are compared against the simulated values obtained with the proposed slip-line field model in Figure 3.16. In order to eliminate the effect of the  $0.1 \text{ mm}$  tool nose radius, the experimental forces with  $w = 0.1 \text{ mm}$  width of cut are subtracted from the forces with  $w = 0.3 \text{ mm}$  and  $w = 0.5 \text{ mm}$  width of cuts, which lead to the cutting forces at  $w = 0.2 \text{ mm}$  and  $w = 0.4 \text{ mm}$  width of cuts. The difference between the experimental and simulated cutting forces is around 15%. The sources of errors include the difference between the Johnson-Cook material parameters and the actual property of the tested workpiece, and the assumption of a constant shear stress along the  $\beta$  slip-lines in the ploughing regions. In addition, the thermal conductance of the workpiece material is not considered. When initial yield strength  $A$  and strain-hardening

coefficient B in the borrowed Johnson-Cook material model [61] are reduced by 20%, the simulated tangential and feed forces are in close agreement with the experimental measurements (see Figure 3.16). It is found that the hardness of the tested material is higher than the brass used in Johnson-Cook. Material hardness depends on the ductility, elastic stiffness, plasticity, toughness and viscosity etc., while cutting forces are influenced by the strain-hardening, velocity and temperature related properties. As suggested by Chandrasekaran et al., parameters in Johnson-Cook model obtained from split-Hopkinson bar tests are used as a starting point to estimate the material flow stress for cutting process [66]. Identification of Johnson-Cook parameters for specific workpiece material in cutting is listed as the future research direction.

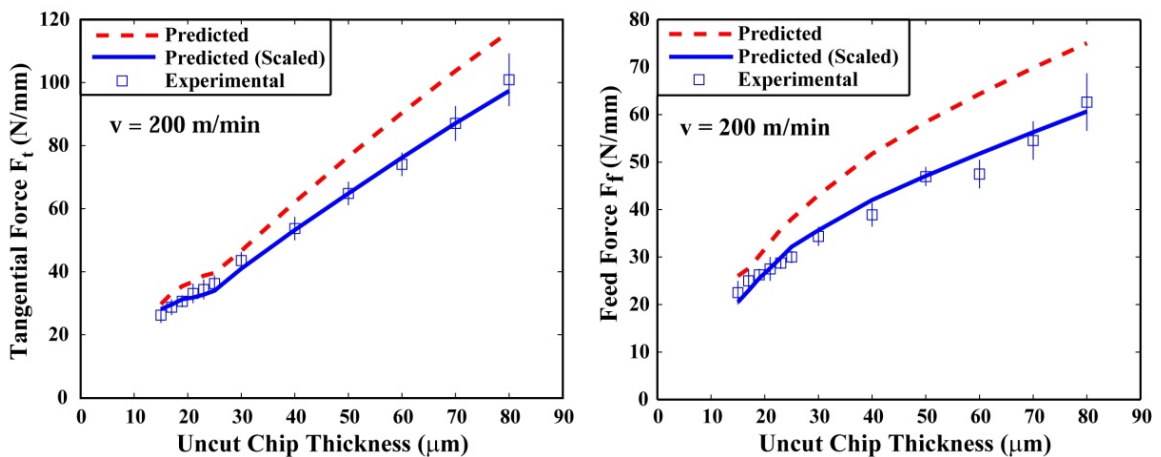


Figure 3.16 Tangential and feed force with uncut chip thickness; predicted: simulation results when using the Johnson-Cook parameters in Table 3.2; predicted (scaled): simulation results when initial yield strength A and strain-hardening coefficient B in Table 3.2 are reduced by 20%. Cutting edge radius: 20 μm.

There is hardly any change in the tangential and feed forces when the cutting speed is increased for the brass, see Figure 3.17. The strain-rate increases with the cutting speed, which results in the increase of material shear stress which is considered in the model. However, the temperature also increases with the cutting speed because of the increased cutting energy which, in turn, reduces the material shear stress, and counterbalances the effect of the strain-rate.

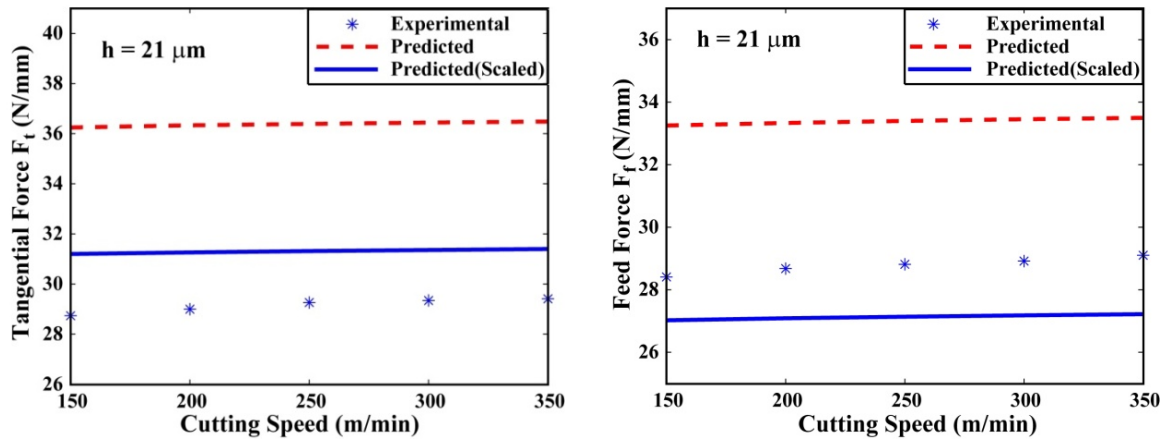


Figure 3.17 Tangential and feed force with cutting speed; predicted: simulation results when using the Johnson-Cook parameters in Table 3.2; predicted (scaled): simulation results when initial yield strength A and strain-hardening coefficient B in Table 3.2 are reduced by 20%. Cutting edge radius: 20  $\mu\text{m}$ .

In order to validate the predictive capability of the proposed model, additional experiments were conducted when the tool edge radii were 15  $\mu\text{m}$  and 35  $\mu\text{m}$ . The cutting speed was 200 m/min and the uncut chip thicknesses were varied from 17  $\mu\text{m}$  to 80  $\mu\text{m}$ . Figure 3.18 shows the comparison of cutting forces between the predicted and experimentally measured forces. The Johnson-Cook parameters used in the simulations were the same as the scaled values explained by Figure 3.16. Since tool-chip contact property was not affected by the tool geometry. The same tool-chip friction parameters identified from 20  $\mu\text{m}$  tool edge radius were applied in the simulations. It is observed that both the tangential and feed forces increase when the tool edge radius increases. The simulations are capable of capturing both the trend and the magnitude of the force variation with respect to the tool edge radius.

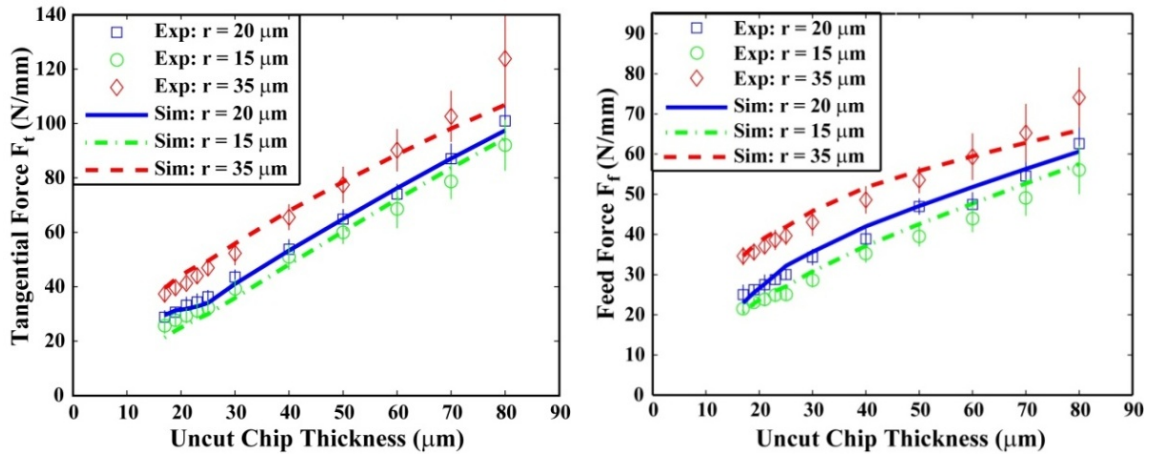


Figure 3.18 Cutting force with tool edge radius. (Sim: simulation results; Exp: experimental results).

### 3.7.3 Simulation results and discussions

After experimental validation of the model with cutting force measurements, further simulation tests have been carried out to have more insights to the process parameters which are difficult to measure experimentally. The simulated results of the effective strain, strain-rate, temperature, and shear flow stresses along line GB for the feed rates (i.e. uncut chip thickness) 15, 19, 21, 25 μm are shown in Figure 3.19. Since line GJ and line JB are divided into 500 elements, the x-axis which shows the number of elements along GB includes a total number of 1000 elements. It is observed that the strain decreases along GJ and then increases along JB. This is because the intersection angle ( $\phi$ ) between the radial line and the y-axis increases in the convex region and then decreases in the concave region shown in Figure 3.6. The strain-rate is constant along GJ because the strain-rate is independent of the intersection angle  $\phi$  as indicated in Equation (3-27). The distribution of temperature along GJ follows the same trend with the strain, since when the strain increases, more shear energy is transferred into thermal energy, which results in the increase of temperature. The variation of shear flow stress is due to the combined results of the strain-hardening, strain-rate, and thermal softening effects. By comparing the strain at different uncut chip thickness values, it is observed that the strain decreases when the uncut chip thickness increases from 15 μm to 25 μm. The chip thickness increases when the uncut

chip thickness increases, which results in a large angular span of the primary shear zone. Therefore, for the same element number along line GB, the inclination angle increases when the uncut chip thickness increases. The strain in the primary shear zone changes inversely with the inclination angle of the slip-line as illustrated in Equation (3-28), therefore, the increase of uncut chip thickness results in the decrease of the strain.

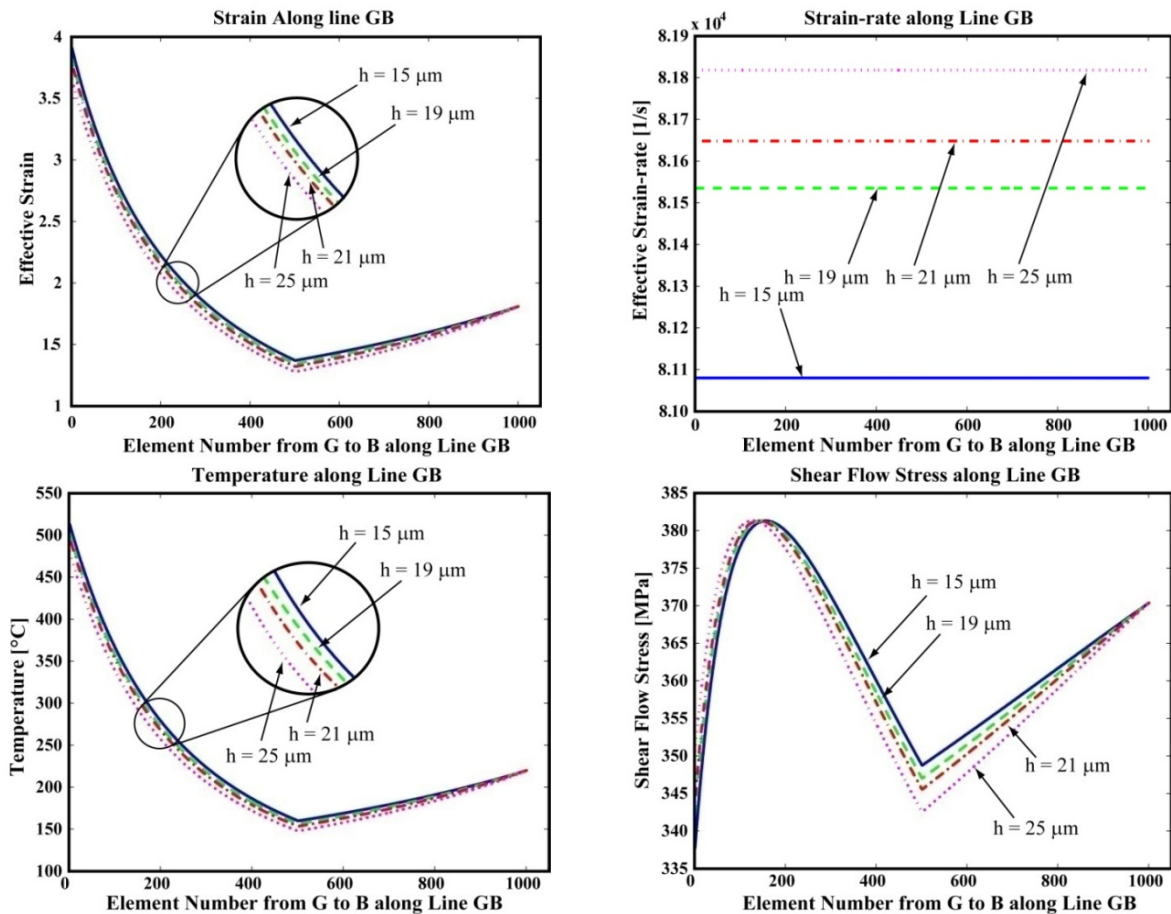


Figure 3.19 Strain, strain-rate, temperature, and shear flow stress along line GB.

Figure 3.20 shows the strain, shear strain rate, temperature, and shear flow stress distribution along slip-line NJ for uncut chip thickness values of 15, 19, 21, 25 μm. The strain increases linearly along NJ while the strain-rate remains constant. This is because the index  $q$  of the shear velocity variation in Equation (3-26) is selected to represent unity in the simulation. The increase of temperature along NJ is because more shearing energy is transferred into thermal energy as a result of the strain increase. The increase of shear flow energy is attributed to the strain-hardening effect.

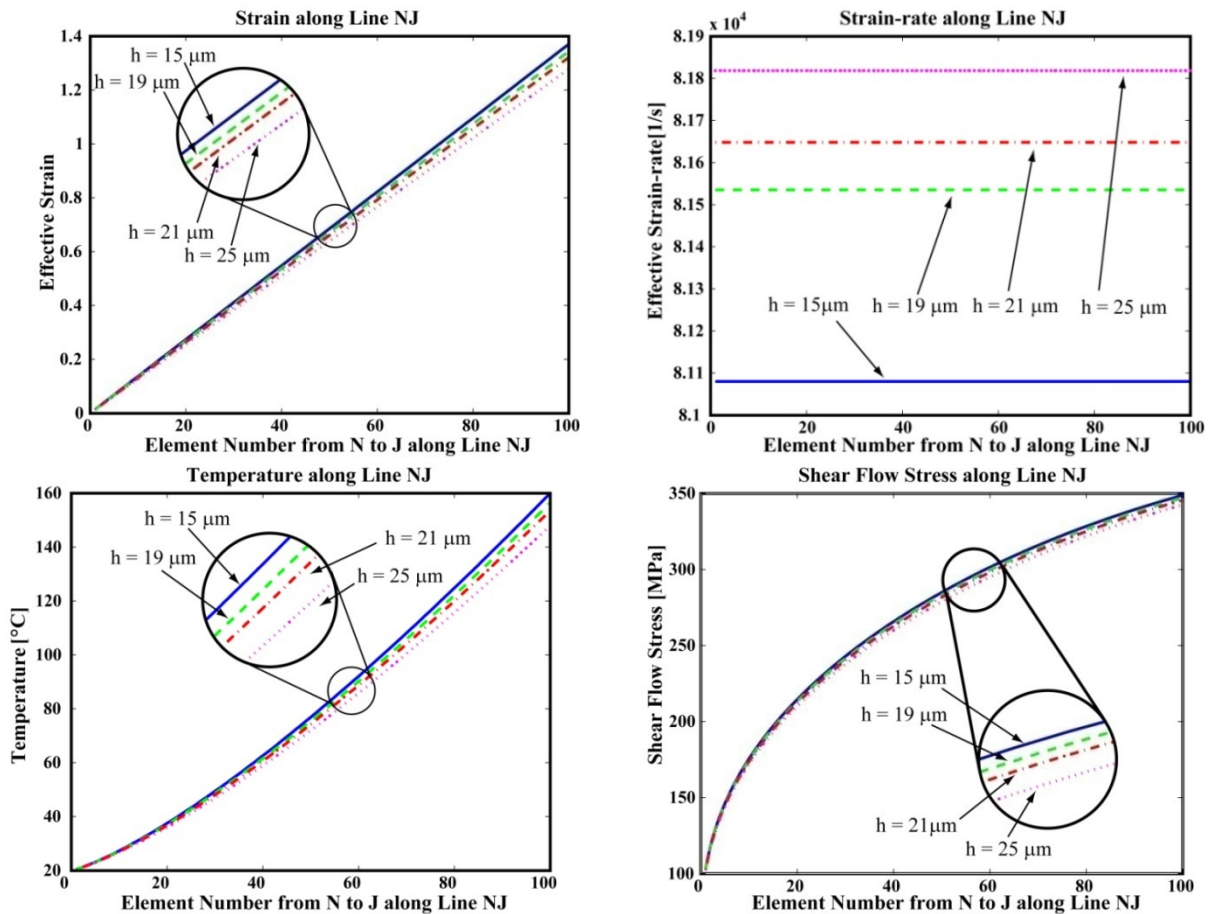


Figure 3.20 Strain, strain-rate, temperature and shear flow stress along line NJ.

The sensitivities of the tangential and feed forces to the coefficient of friction and stagnation angle are analyzed at cutting speed of  $V = 200$  m/min and feed rate of  $h = 25 \mu\text{m}$ . The coefficient of friction is varied from 0.1 to 0.5, and the stagnation angle is increased from  $30^{\circ}$  to  $70^{\circ}$ . The simulated tangential and feed forces increase by 22% and 11% respectively, when the coefficient of friction increases by 500%. The tangential force increases by 11%, while the feed force decreases by 27% when the stagnation angle is increased from  $30^{\circ}$  to  $70^{\circ}$ . The decrease of the feed force is attributed to the increased ploughing at higher stagnation angles. Since the material is suppressed downwards, the vertical component of the friction force in the ploughing region is negative. As the friction force in the ploughing region increases, the total feed force decreases. However, these are rather exaggerated variations in the friction and stagnation angle. In reality, the friction may change less than  $\pm 50\%$  based on the lubricant and surface quality of the tool. The

stagnation angle changes between 50 to 60 degrees depending on the edge radius and friction. The force changes by 3-4% with the realistic friction and stagnation angle changes.

Figure 3.21 shows the distribution of normal and friction stresses along tool-chip contact from point D to point A at  $V = 200$  m/min and  $h = 25$   $\mu\text{m}$ . The absolute value is plotted regardless of the direction of the stress. The normal stress increases from point D to the stagnation point S and then decreases to point A. The increase of the friction stress from point D to point B is due to the decrease of the inclination angle of the  $\alpha$  slip-lines with respect to the y-axis from line NJ to TB. Since the shear strain decreases from point B to point T along TB, the shear flow stress decreases from point B to A along the tool edge, resulting into the decrease of the friction stress.

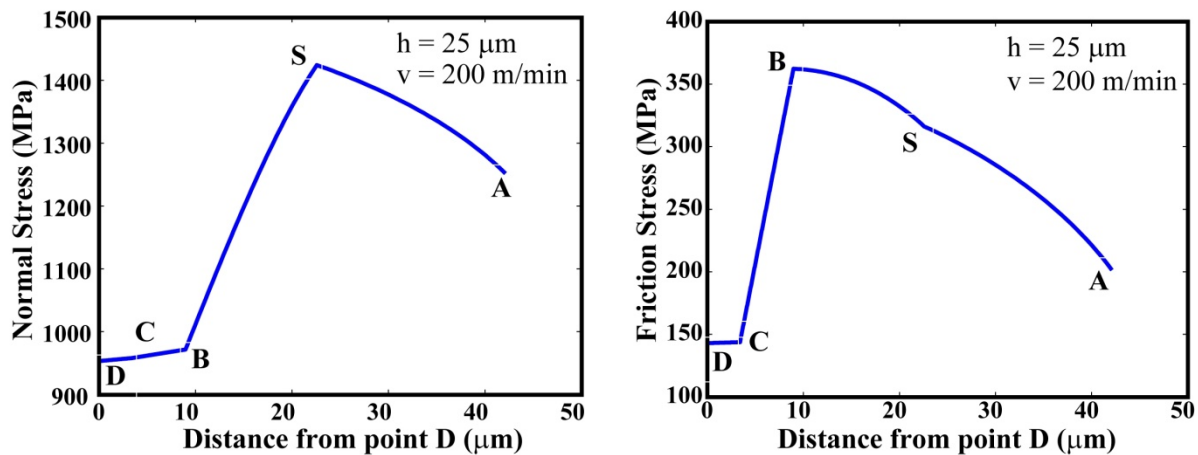


Figure 3.21 Distribution of normal and friction stress along tool-chip contact.

### 3.7.4 Summary of slip-line field model

The slip-line field model of the micro-cutting process with round tool edge including strain, strain-rate, and temperature effects on flow stress is presented. The plastic deformation zones are divided into the primary shear zone, the secondary shear zone where the chip moves along the regular rake face of the tool, and the tertiary zone where the material bifurcates upward to form the chip and downward to form the machined surface. A set of orthogonal micro-turning tests were conducted under a range of uncut chip thickness values and cutting speeds. The friction at the tool-chip contact is identified from the orthogonal cutting tests with one tool geometry and applied on the tools with different edge

geometry. The total force is obtained by adding the cutting force along the rake face of the tool and the ploughing force along the round edge below the material separation angle. The distribution of shear strain, shear strain-rate, temperature, and shear flow stress is obtained with different uncut chip thickness values, and the increase of the shear strain, temperature, and shear flow stress with respect to the decrease of uncut chip thickness is observed. The predicted cutting force is in agreement with the experimental results with respect to the variation of uncut chip thickness, cutting speed and edge radius.

It is shown that the micro-cutting process can be modeled and predicted effectively using the slip-line field model. The accuracy of the predictions can be improved by identifying the tool-chip friction properties from cutting tests. The realistic variation of stagnation angle around the curved cutting edge and friction alter the cutting forces only by 3-4%, while they may have stronger effects on strain, stress and temperature distributions at tool-chip material contact. The prediction accuracy is highly dependent on the correctness of the constitutive material model. In addition to analytical insight to the micro-cutting process, the slip-line field approaches are computationally faster than finite element methods. After the tool-chip friction parameters are identified from one edge radius value, they can be used to predict the cutting forces for other tool edge radii. However, slip-line field model is based on plastic flow laws, and cannot accommodate the fracture and non-homogenous materials.

### **3.8 Cutting forces prediction in micro-milling**

The slip-line field model is used to predict the cutting forces in micro-milling from material's constitutive model and friction parameters between the tool and workpiece materials. The simulated cutting forces in orthogonal micro-cutting are used to express cutting force coefficients as nonlinear functions of tool edge radius and uncut chip thickness, mimicking mechanistic models. The milling forces are then predicted by adjusting the cutting force coefficients as the chip varies. The predicted cutting forces are experimentally validated. Actual tool tip trajectory, run-out and the effects of dynamometer

dynamics are considered. There has been no mechanistic calibration used throughout the proposed process model chain.

### 3.8.1 Cutting force coefficient estimation from slip-line field model

A series of brass cutting simulations are performed at a range of uncut chip thicknesses ( $h \in [1, 50] \mu m$ ) and tool edge radii ( $r \in [0.001, 8] \mu m$ ). It is observed from Figure 3.17 that both the tangential and feed forces are not sensitive to the variation of cutting speed in the range of 150-350 m/min for cutting brass 260, therefore, the speed effect is neglected in modeling the cutting force coefficients. However, since cutting speed influences the strain-rate and temperature which are included in the Johnson-Cook constitutive model, it is possible to add the speed effect in the mechanics model to identify the cutting force coefficient for speed sensitive materials. The predicted cutting forces by slip-line field model for brass 260 are shown in Figure 3.22. The cutting forces are then modeled as:

$$F_t = K_t(h, r)hw ; F_f = K_f(h, r)hw \quad (3-65)$$

where the cutting force coefficients are curve fitted to the simulated forces as follows:

$$\begin{cases} K_t(h, r) = K_{t1}(h) + K_{t2}(h, r) = \alpha_t h^{d_t} + \beta_t h^{p_t} r^{q_t} \\ K_f(h, r) = K_{f1}(h) + K_{f2}(h, r) = \alpha_f h^{d_f} + \beta_f h^{p_f} r^{q_f} \end{cases} \quad (3-66)$$

The empirical constants ( $\alpha$ ,  $\beta$ ,  $d$ ,  $p$  and  $q$ ) relate the sensitivity of the forces to the edge radius and chip thickness. The first term  $\alpha h^d$  is independent of tool edge radius, and it could be considered as the force coefficient when the tool is perfectly sharp. The nonlinearity increases when the size of the tool edge radius is comparable with the uncut chip thickness. The identified constants in Equation (3-66) are listed in Table 3.4.

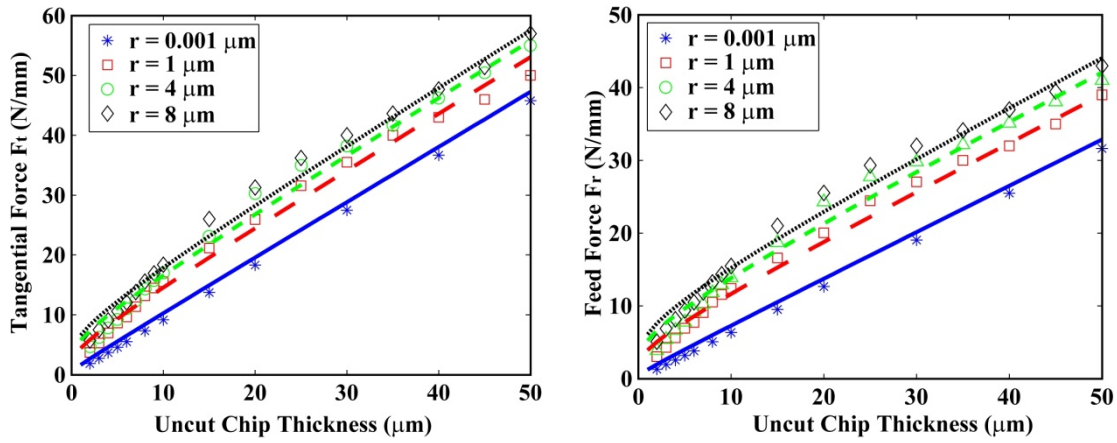


Figure 3.22 Simulated cutting forces from slip-line field model. Material: brass 260. See Equation (3-15) and Figure 3.16 for material properties. Cutting speed = 25 m/min and tool's primary rake angle = 5 deg. Symbols represent the simulated results from slip-line field model, and the lines are the curved-fitted results.

Table 3.4 Constants for the cutting force coefficients of material brass 260 at cutting speed 25 [m/min]. Units of chip thickness and edge radius are in [mm].

	$\alpha$	$d$	$\beta$	$p$	$q$
$K_t$ [N/mm <sup>2</sup> ]	914.4	-0.0004	62.21	-0.8144	0.2302
$K_f$ [N/mm <sup>2</sup> ]	629.4	-0.0002	78.24	-0.7868	0.2469

### 3.8.2 Prediction of micro-milling forces

The cutting force coefficients identified from the slip-line field model are used to predict micro-milling forces. Tangential ( $dF_t$ ) and radial ( $dF_r$ ) forces acting on a cutting edge with a differential depth of cut  $dz$  are expressed as (Figure 3.23):

$$dF_t(\phi) = K_t h(\phi) dz, \quad dF_r(\phi) = K_f h(\phi) dz \leftarrow \phi \in (\phi_{st}, \phi_{ex}) \quad (3-67)$$

where  $\phi$  is the instantaneous immersion angle of the tool, and  $\phi_{st}$  and  $\phi_{ex}$  are the entrance and exit angles of the cutter, respectively. The forces are zero when the edge is out of cut. The instantaneous chip thickness  $h(\phi)$  is evaluated by considering the exact kinematics of the milling [67], general tool geometry and the effect of radial run-out of flutes [68]. The elemental forces are resolved into feed and normal directions:

$$\begin{cases} dF_x(\phi) = -dF_t \cos(\phi) - dF_r \sin(\phi) \\ dF_y(\phi) = dF_t \sin(\phi) - dF_r \cos(\phi) \end{cases} \quad (3-68)$$

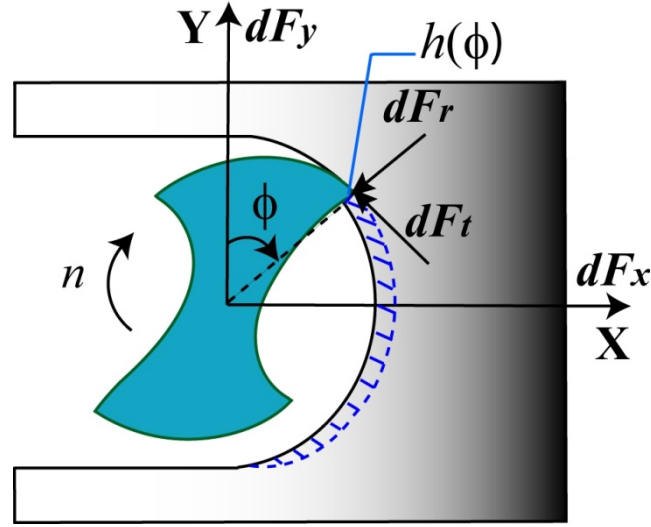


Figure 3.23 Micro-milling process.

The total milling forces are evaluated by integrating all the elemental forces contributed by  $N$  flutes ( $i$ ) along the axial depth of cut ( $a$ ).

$$\begin{cases} F_x(\phi) = \sum_{i=1}^N \int_0^a dF_x \left[ \phi + (i-1) \frac{2\pi}{N} \right] d\phi \\ F_y(\phi) = \sum_{i=1}^N \int_0^a dF_y \left[ \phi + (i-1) \frac{2\pi}{N} \right] d\phi \end{cases} \quad (3-69)$$

The details of the general milling model have been presented before by Altintas et al. [67][68], and the algorithms have been integrated into an advanced milling process simulation system [69] and used in predicting micro-milling forces, vibrations, dynamic chip thickness and surface form errors.

### 3.8.3 Experimental validation in micro-milling

The micro-milling tests have been performed on the micro-machining center having a spindle speed range of 60,000 rev/min. The experimental setup is shown in Figure 3.24. A two-flute carbide micro end mill (MITSUBISHI MS2MS) with 200  $\mu\text{m}$  diameter and 30° helix angle is used in milling Brass 260 with 75 HRB hardness. Tool edge radius of the micro mill is measured to be 3.7  $\mu\text{m}$  with an optical microscope shown as Figure 3.25. The workpiece is fixed on a Kistler 9256 three component mini-dynamometer to measure the

cutting forces. The vertical position of the tool tip with respect to the workpiece is aligned by moving the cutting tool down to the workpiece very slowly while a low voltage is applied on both tool and workpiece. The reference position is recorded when the tool came into contact with the workpiece and a short circuit signal is triggered.

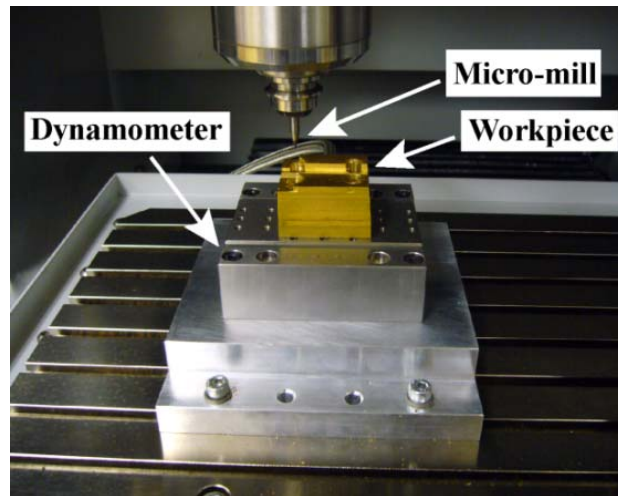


Figure 3.24 Set-up for micro-milling tests: Mikrotool CNC micro-machining center, Kistler 9256 mini-dynamometer, brass 260 coupon.

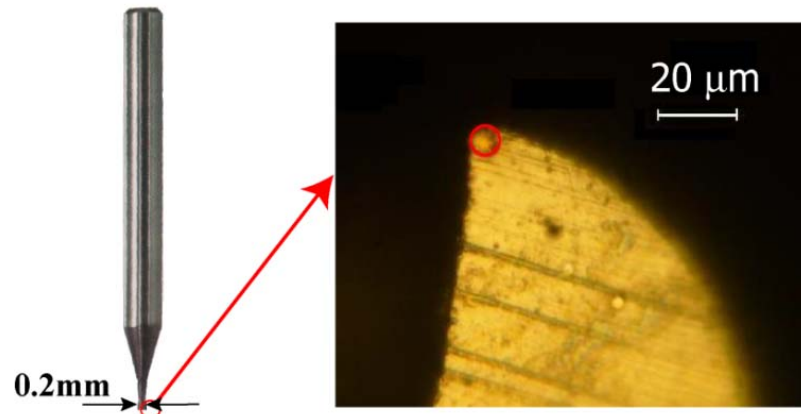


Figure 3.25 Two-fluted micro-mill with 200  $\mu\text{m}$  diameter and 3.7  $\mu\text{m}$  edge radius.

The static radial run-out of the micro-mill is measured and the experimental setup is shown as Figure 3.26. The cutting edge of the micro-mill is inspected by an on-machine camera through a 50X objective lens and a 3X microscope. The edge of the first tool flute is aligned to a reference line shown as Figure 3.27 (a), then the tool is rotated manually by 180°. The distance between the edge of the second flute and the reference line is measured

to be  $1.2\ \mu\text{m}$  shown in Figure 3.27 (b). Therefore, the radial run-out of the tool with respect to the spindle center is half of the measured distance ( $0.6\ \mu\text{m}$ ).

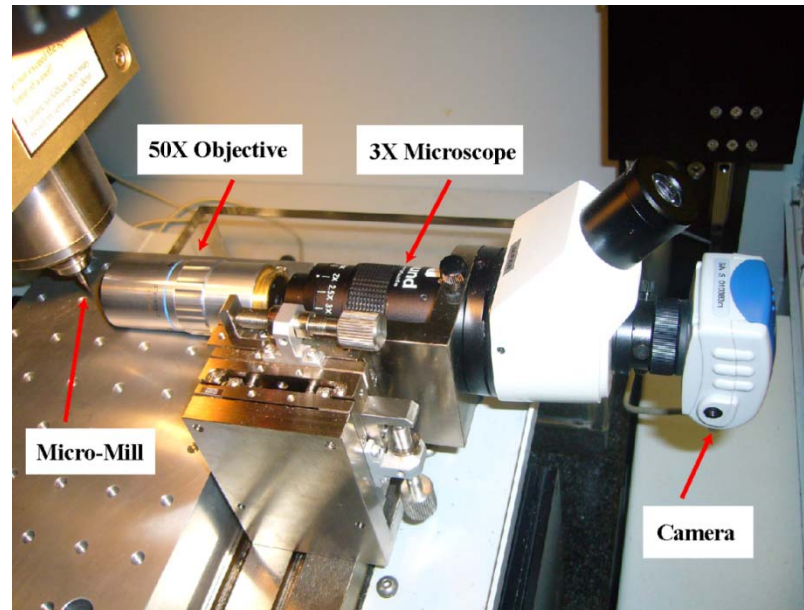


Figure 3.26 Experimental setup to measure static radial run-out of tool.

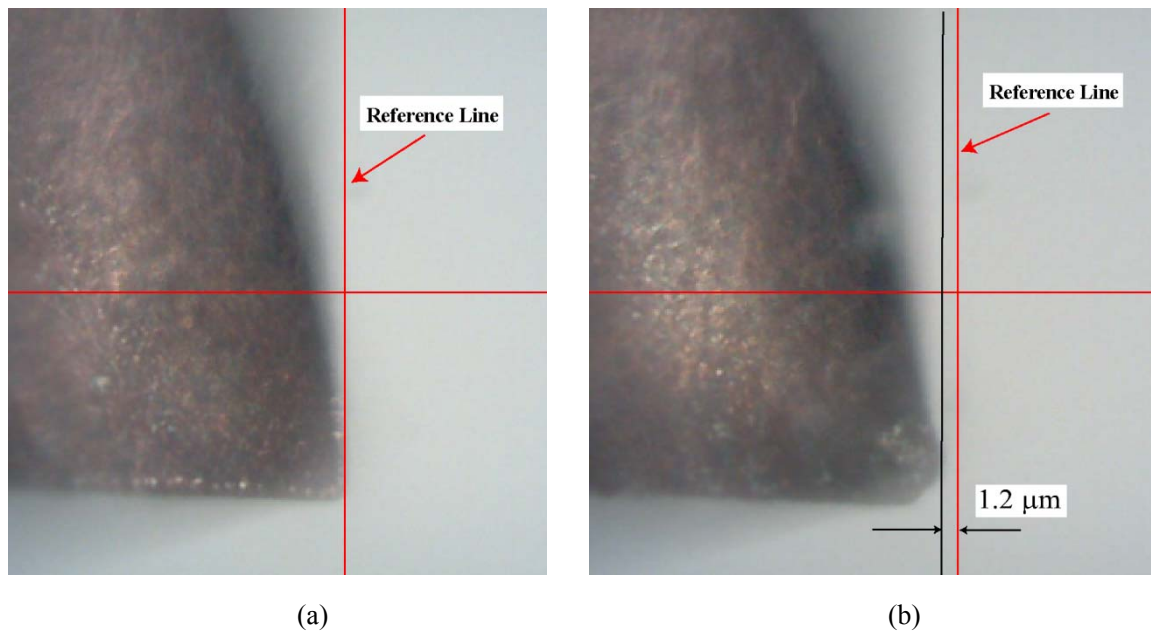


Figure 3.27 (a) The edge of first flute is aligned to the reference line, (b) Distance between the edge of second flute and the reference line.

Due to the high spindle speeds, the frequency bandwidth of the dynamometer was inadequate for measuring the periodic cutting forces in the micro-milling process. When the

tooth passing frequency of the force signal is beyond the bandwidth of the dynamometer, the force measurement is distorted due to the structural mode of the measurement system. Altintas and Park [70] employed a Kalman filter method to compensate the dynamics of the force sensor system in order to accurately measure the milling forces. Park and Malekian [71] applied the Kalman filter to reconstruct the cutting force in micro-milling based on the measurement data. The modal parameters of the dynamometer are identified from impact modal tests applied on the X and Y directions. The input force from the hammer (PCB086C80) and output force from the dynamometer are measured to obtain the FRF of the dynamometer. The FRF results shown in Figure 3.28 indicates a bandwidth of 2000 Hz with a dominant mode at 3403 Hz and 3067 Hz. Unless these two modes are compensated, the harmonics of the milling forces may cause poor measurements with the dynamometer at spindle speeds above 12000 rev/min.

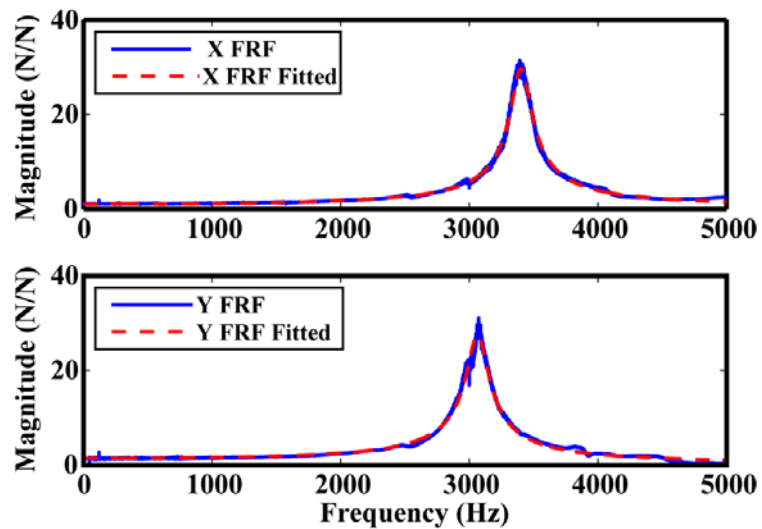


Figure 3.28 FRFs of dynamometer in X and Y directions.

The measured FRFs are curve fitted by the following transfer function:

$$\Phi(s) = \frac{1}{m's^2} + \frac{a'+b'j}{s-r'} + \frac{a'-b'j}{s-r'^*} + \frac{1}{k'}; \quad r' = -\zeta\omega_n + j\omega_n\sqrt{1-\zeta^2} \quad (3-70)$$

where  $r'$  is the pole of the characteristic polynomial calculated from the natural frequency  $\omega_n$  and the damping ratio  $\zeta$ ,  $a'$  and  $b'$  are real and imaginary residues,  $m'$  and  $k'$

are the residues for mass and stiffness in order to maintain the curve fitting accuracy in low and high frequency range. The residues are identified based on least square method and the modal parameters of the dynamometer are listed in Table 3.5.

Table 3.5 Modal parameters of dynamometer in X and Y directions.

Direction	$\omega_n$ (Hz)	$Z$	$a'$	$b'$	$m'$	$k'$
X	3403	0.0235	-1343	-14870	5.493	-2.87
Y	3067	0.0276	-1065	-14570	-1.823	-8.650

Several cutting tests at different spindle speeds and feed rates have been conducted to validate the predictive micro-milling model. The tool is inspected for wear and damage after each cut by a microscope integrated to the machine. Sample experimental and simulation results are given in Figure 3.29 and Figure 3.30. Speeds between 45,000 and 60,000 rev/min have been deliberately avoided to prevent resonating the two modes (3403 Hz and 3067 Hz) of the dynamometer. The dynamometer's modes are still slightly excited by the harmonics of high tooth passing frequencies (666 Hz and 1333 Hz), and appear as distorted oscillations on the raw measurement data. When the measured forces are Kalman filtered [70] to compensate the distortion of cutting forces caused by the dynamometer dynamics, they agree well with the simulations. The correct measurement of micro-milling forces, which are less than 1 N, would be difficult unless the dynamics of the dynamometer are considered. The simulations are carried out by using the cutting force coefficients predicted from slip-line field analysis (Table 3.4). The tool run-out and edge geometry are considered, as well as the effect of the exact chip size as the tool rotates by the simulation system [69]. Considering that the micro-milling forces are predicted directly from the constitutive model of the material, the simulation results fairly agree with the experimental measurements. Similar results are obtained at various feed rates and spindle speeds.

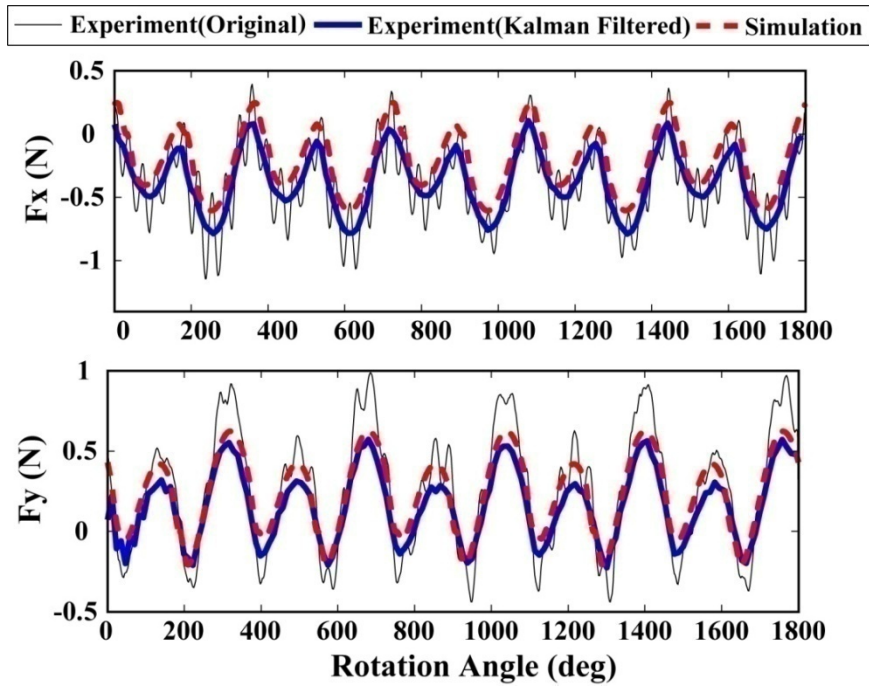


Figure 3.29 Slot micro-milling with 50  $\mu\text{m}$  axial depth of cut. Material: brass 260. Tool: 200  $\mu\text{m}$  diameter. Spindle speed: 20,000 [rev/min]. Feed-rate: 3  $\mu\text{m}/\text{rev}/\text{tooth}$ .

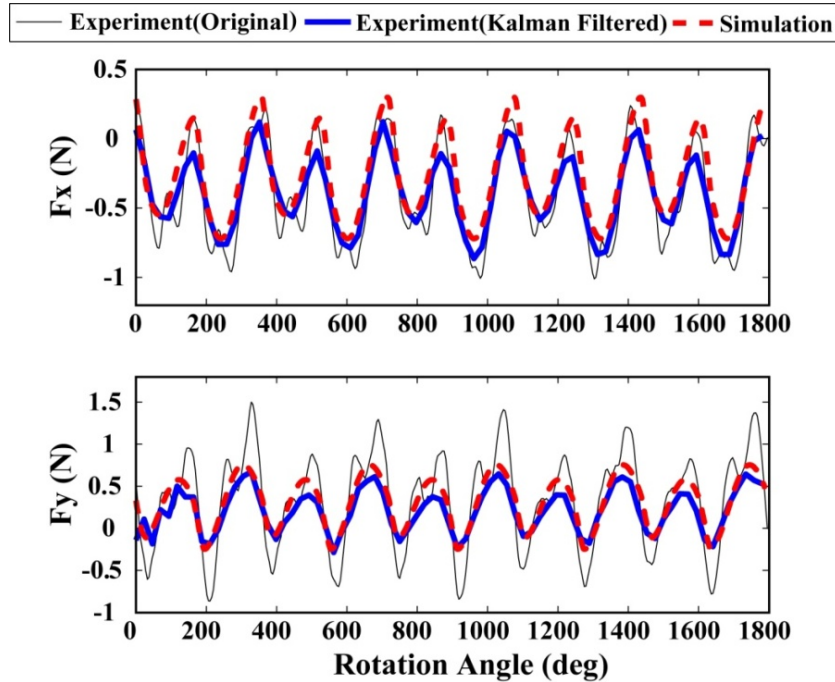


Figure 3.30 Slot micro-milling with 50  $\mu\text{m}$  axial depth of cut. Material: Brass 260. Tool: 200  $\mu\text{m}$  diameter. Spindle speed: 40,000 [rev/min]. Feed-rate: 5  $\mu\text{m}/\text{rev}/\text{tooth}$ .

### **3.9 Conclusion**

The chapter illustrates the analytical prediction of micro-turning and micro-milling forces directly from the material's temperature and strain sensitive flow stress model. This is based on slip-line field theory which models the plastic deformation of workpiece material including both shearing and ploughing effects. By modeling the strain, strain-rate and temperature in the primary shear zone from the variation of shear velocity, the distribution of flow stress and hydrostatic pressure is obtained, and the cutting force is predicted as an integration of the stress along the entire tool rake face and round edge. The cutting force simulations from orthogonal micro-cutting are used to model the cutting force coefficients as functions of uncut chip thickness and tool edge radius. The identified cutting coefficients are then used in milling model which considers the actual tool tip trajectory, radial run-out and dynamics of the dynamometer. Comparisons between simulated and experimental results show that micro-milling force which has less than one Newton amplitude can be predicted without mechanistic calibration. However, the prediction accuracy is influenced by the correctness of the constitutive property of workpiece material.

# Chapter 4

## Finite Element Modeling of Micro-cutting Process<sup>2</sup>

### 4.1 Overview

This chapter presents the FE modeling of orthogonal micro-cutting process by considering the uncut chip thickness and tool edge radius effects, and predicting the micro-milling forces with experimental validation. ABAQUS/Explicit 6.8-3 [72] is used as the software platform. The FE model simulates the micro-cutting forces from the material's constitutive model and friction parameters between the tool and workpiece materials. An arbitrary Lagrangian Eulerian meshing strategy is applied to avoid element distortion during the simulation. The predictions of cutting forces with the proposed FE model and the slip-line field model illustrated in Chapter 3 are compared against experimental measurements. Predictions of stress, strain and temperature fields are also compared to assess the viability of using the two methods in micro-cutting analysis. The micro-milling forces are then predicted by adjusting the cutting force coefficients as the chip varies. The predicted milling forces are compared with experimental results through a series of micro-milling tests at different cutting speeds and feed rates. The flowchart of the cutting force prediction in micro-milling from FE method is shown in Figure 4.1.

---

2. The content of Chapter 4 has been published in: Jin, X., Altintas, Y., 2011. Prediction of Micro-milling Forces with Finite Element Method. *Journal of Materials Processing Technology*, vol.212, 542-552.

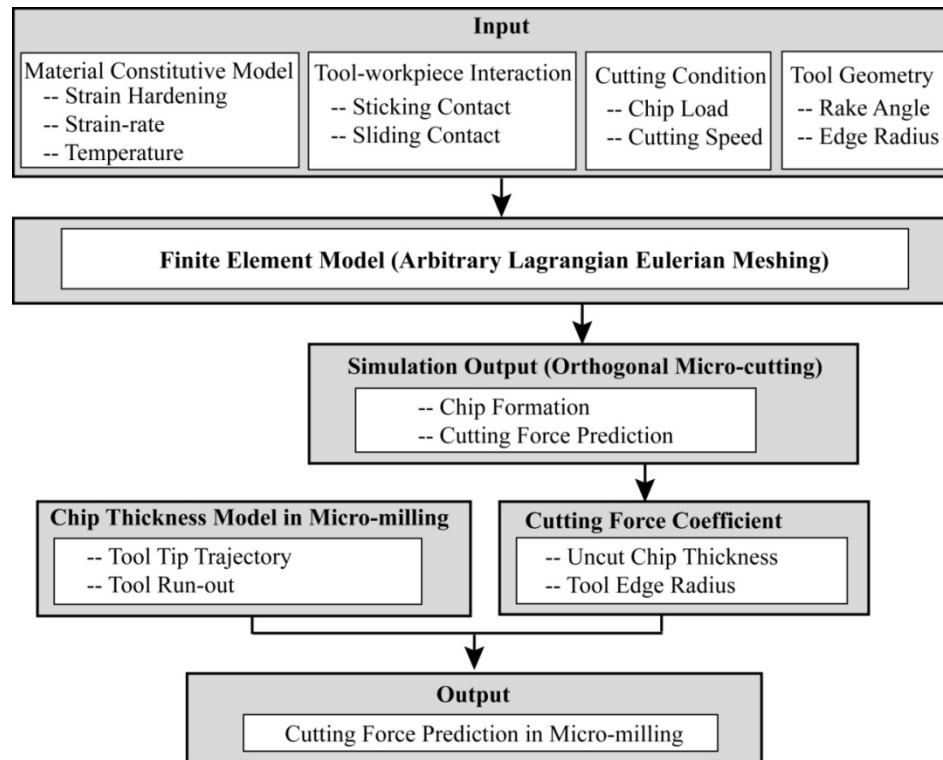


Figure 4.1 Flow chart of cutting force prediction from FE model.

The content of this chapter is arranged as follows. Section 4.2 illustrates the FE modeling procedure of orthogonal micro-cutting process with round tool edge effect. Section 4.3 shows the comparison of cutting force results from FE model against slip-line field simulations as well as experimental measurements. Distributions of stress, strain and temperature fields simulated by the analytical and numerical models are compared. Section 4.4 gives the experimental validation of the FE model by micro-milling experiments with a series of spindle speed and feed rate values. Concluding remarks are given in the last section.

## 4.2 FE modeling of orthogonal micro-cutting

The FE model of orthogonal micro-cutting process is developed using commercial software ABAQUS/Explicit 6.8-3. The dynamic, explicit, adiabatic analysis is applied since the work material deforms in a short period of time with large plastic strains during the cutting process [72]. The round cutting edge is included in the plain strain based FE model as shown in Figure 4.2. The tool is modeled as an isothermal rigid body represented by the

reference point (RP) in order to collect the cutting force data. The workpiece is meshed by the four-node thermally coupled quadrilateral elements. The size of the mesh close to the tool edge is around  $0.5 \mu\text{m}$  in order to maintain the simulation precision and to ensure a practical computational time. The tool is completely fixed and the workpiece moves towards the tool with velocity  $V$  in X - direction, and the nodes at the bottom surface of the workpiece are constrained in Y - direction. Room temperature ( $25 \text{ }^\circ\text{C}$ ) is applied to the tool and workpiece as an initial temperature condition.

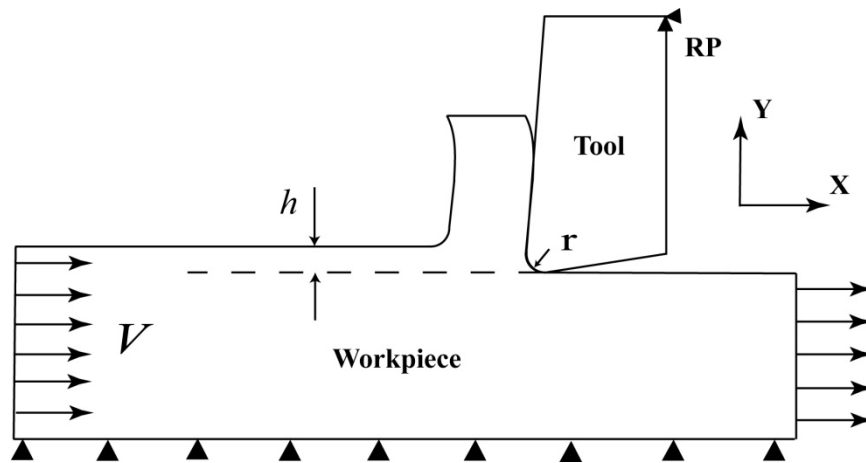


Figure 4.2 Finite element model of orthogonal micro-cutting process.

#### 4.2.1 Material properties

The constitutive model of workpiece material (Brass 260) is used as given by Johnson and Cook shown in Equation (3-15). The material constants are identified by Johnson and Cook and experimentally adjusted in Section 3.7 for the tested workpiece and given in Table 4.1. Other physical properties of the work material used in the FE model are summarized in Table 4.2.

Table 4.1 Johnson-Cook parameters of brass 260 (Strain-hardening constants in the original Johnson-Cook model [61] are reduced by 20% for the specific tested material as explained in Section 3.7)

$A$ [MPa]	$B$ [MPa]	$C$ [-]	$n$ [-]	$m$ [-]	$T_m$ [ $^\circ\text{C}$ ]	$T_r$ [ $^\circ\text{C}$ ]
90	404	0.009	0.42	1.68	916	25

Table 4.2 Physical properties of brass 260.

Property	Brass 260
Density [kg/m <sup>3</sup> ]	8500
Elastic Modulus [MPa]	110000
Poisson's Ratio	0.33
Conductivity [W/m/°C]	109
Specific Heat [J/kg/°C]	377
Inelastic Heat Fraction	0.9

#### 4.2.2 Tool-workpiece contact

The sticking and sliding contacts between the tool and the workpiece are considered in the FE model. In the sticking contact region, a critical frictional stress  $\tau$  is reached due to the high normal stress on the cutting tool. The sliding contact satisfies the coulomb friction law with a constant coefficient of friction  $\mu$ . The values of frictional stress limit and the coefficient of coulomb friction are based on the experimental identification shown in Equation (3-64) for the Brass 260 material:

$$\begin{cases} \mu = 0.15 \\ \tau = 220 [MPa] \end{cases} \quad (4-1)$$

The fraction of dissipated energy converted into heat due to the friction is assumed to be 100% and the heat is distributed equally between the tool and work surface in contact.

#### 4.2.3 Meshing strategy and chip formation

Arbitrary Lagrangian Eulerian (ALE) adaptive meshing is applied in the FE model to avoid the excessive distortion of the elements. ALE combines the feature of Lagrangian analysis in which the mesh is attached to the material, and Eulerian analysis where the mesh is fixed in space while the material moves through the mesh in Eulerian region. The mesh moves independently from the material in the ALE mesh domain. Nodal positions are remapped at a predefined frequency to reduce element distortion. Due to the adaptive

meshing technique, material separation mechanism is simulated without defining the fracture criteria of the workpiece material, and excessive distortions of the elements around the tool edge are avoided.

ALE constraint is applied to specify the mesh motion strategy as proposed by Nasr et al. [73]. The workpiece is partitioned into several sections as shown in Figure 4.3. The mesh regions filled with solid lines are specified as Eulerian regions where the mesh motions are constrained in both X and Y directions. Other regions are specified as Lagrangian regions where the mesh follows the motion of material. The Lagrangian regions filled with the dashed line are constrained in the Y direction in order to avoid the element distortion at the interface between the Lagrangian and Eulerian regions. By applying ALE constraint, the force oscillations experienced in ALE models where the mesh constraint was not considered [40] can be avoided.

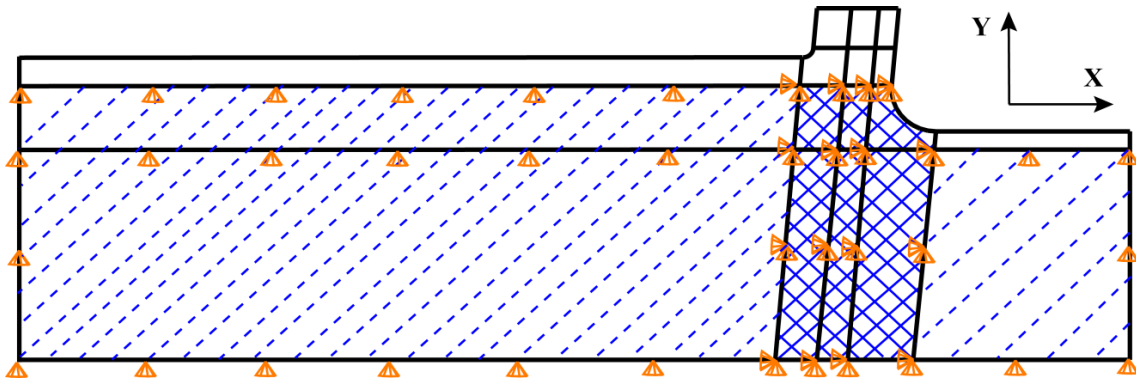


Figure 4.3 ALE constraint of the workpiece mesh.

An initial chip thickness is predefined at the beginning of the simulation. Figure 4.4 shows both the initial and machined chip thickness in the FE simulation. The meshing elements in the Eulerian region have no deformation; hence no element distortion occurs close to the tool edge. In the Lagrangian region, the mesh follows the material motion and forms the machined chip. The steady state chip shape is influenced by the material property and friction behavior rather than the initial guess.

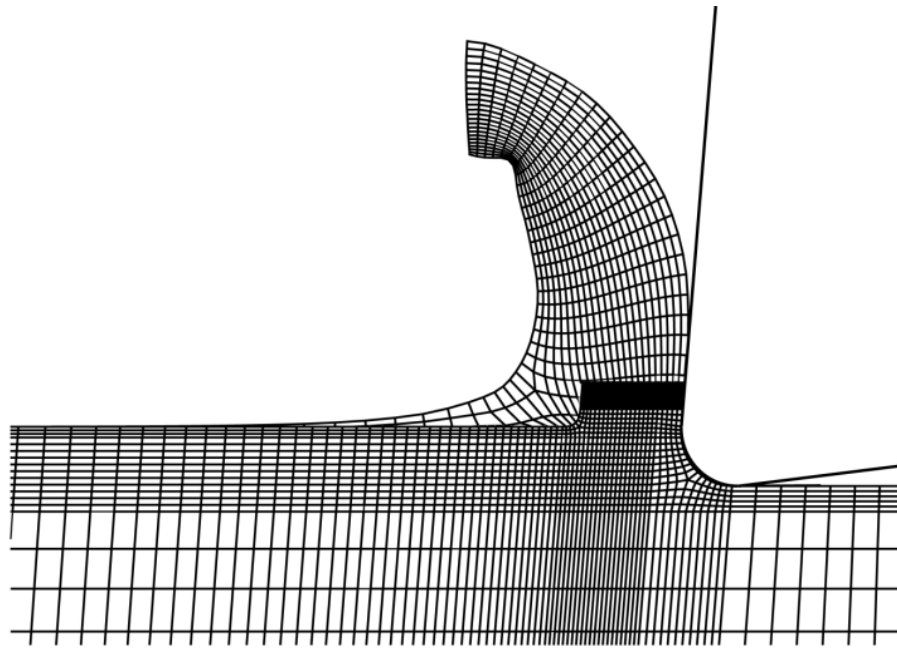


Figure 4.4 Initial and machined chip in the FE simulation.

When the uncut chip thickness is small, all the material is suppressed downwards by the tool edge, only ploughing occurs without chip formation. In this case only ALE is applied on the work elements and no mesh constraint is specified. Figure 4.5 shows the material deformation with small uncut chip thickness value.

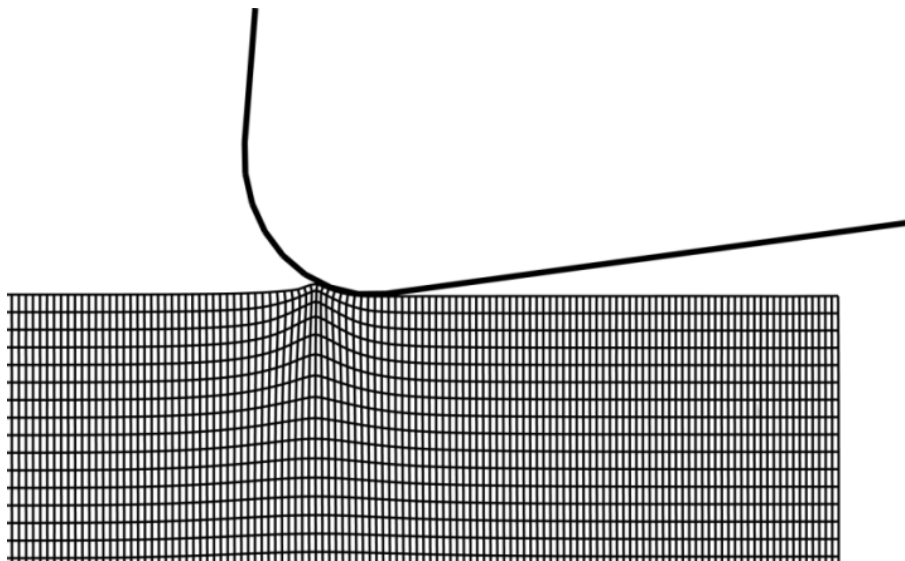


Figure 4.5 Material deformation with small uncut chip thickness.

#### 4.2.4 Determination of material separation point

The slip-line field model shown in Figure 3.1 calculates the force in the ploughing

region which is determined by the position of separation point S on the round tool edge. Material separation is due to excessive plastic deformation which results into the fracture of the material. By using ALE adaptive meshing strategy, the bifurcation of the workpiece material is observed from the distribution of velocity vector around tool edge without defining material fracture criterion, shown in Figure 4.6. The length of the vectors represents the relative velocity magnitude of the meshing elements in the FE model.

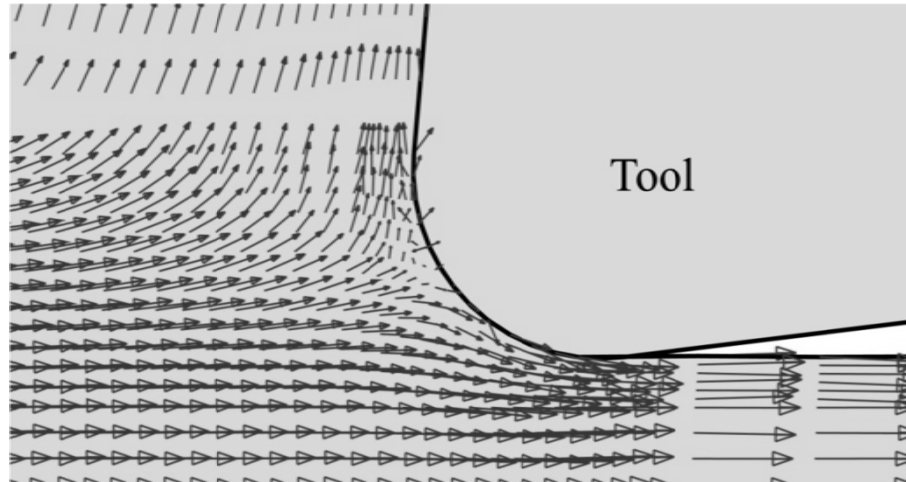


Figure 4.6 Vector of workpiece velocity around too edge.

Figure 4.7 shows the distribution of the vertical velocity components of the workpiece around the tool edge. The position with zero vertical velocity indicates the material separation position. The boundary line CD refers to the line with zero material velocity based on the spectrum of velocity magnitude. Therefore, the separation angle  $\theta_S$  is identified by measuring the angle between line CO and the y-axis as shown in Figure 4.7, where C is the material separation point, and O is the center of the round edge.

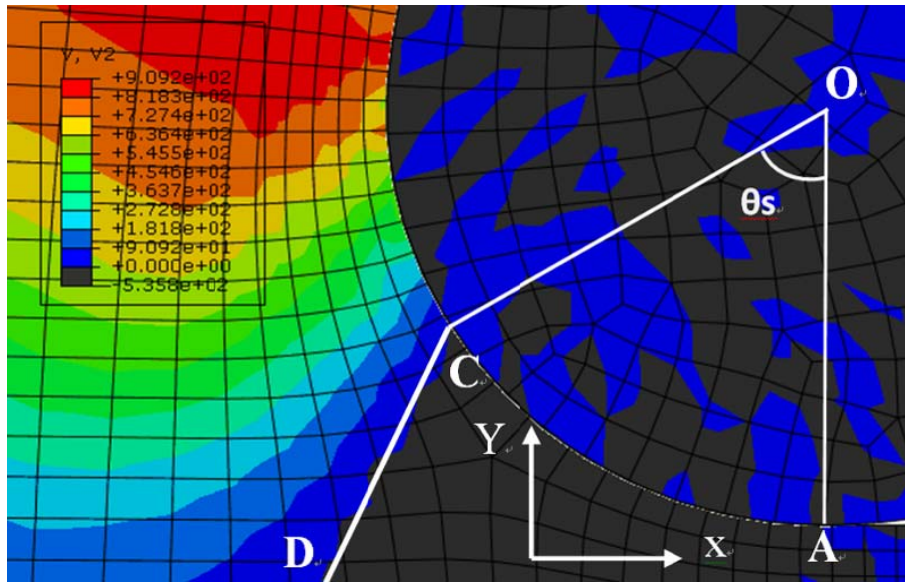


Figure 4.7 Spectrum of vertical velocity in the tertiary zone.

### 4.3 Prediction of cutting forces with FE model

A series of brass cutting simulations are performed at different uncut chip thicknesses ( $h \in [0.5, 80] \mu m$ ) and tool edge radii ( $r \in [1, 20] \mu m$ ). The tangential and feed forces are captured at the reference point of the tool. Figure 4.8 shows the evolution of cutting forces with respect to time. Since the tool is modeled as a rigid body, the forces reach constant, steady state values which are recorded.

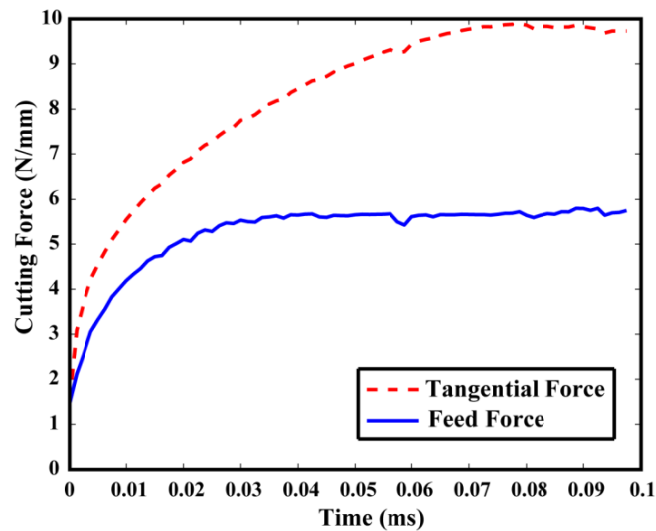


Figure 4.8 Simulated cutting forces with FE. Uncut chip thickness =  $4 \mu m$ , cutting speed = 25 m/min, tool edge radius =  $8 \mu m$  and primary rake angle = 5 deg, material: brass 260.

The micro-cutting processes at two different cutting speeds are simulated with  $4\ \mu\text{m}$  tool edge radius. The cutting speed  $v_1 = 25\ \text{m/min}$  corresponds to 40000 r/min spindle speed for a micro-mill with  $200\ \mu\text{m}$  diameter, and speed  $v_2 = 12\ \text{m/min}$  corresponds to 20000 r/min spindle speed. Figure 4.9 shows the cutting force results. The force variation is observed to be less than 5% when the cutting speed is increased from 12 m/min to 25 m/min. The effect of the cutting speed on the force prediction can be neglected when cutting Brass 260 in the operation range of the spindle used in this study. However, the speed effect can be included if the material exhibits sensitivity at the cutting speed range used in the application.

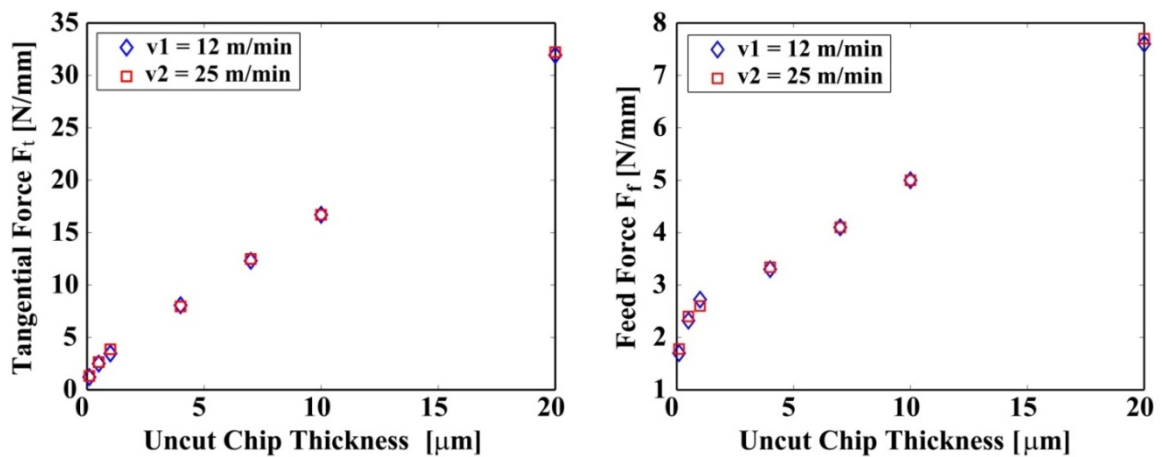


Figure 4.9 Simulated forces with cutting speeds. Cutting speeds:  $v_1 = 12\ \text{m/min}$ ,  $v_2 = 25\ \text{m/min}$ , cutting edge radius =  $4\ \mu\text{m}$ .

Figure 4.10 shows the predicted cutting forces by FE model when a tool with  $20\ \mu\text{m}$  cutting edge radius is used. The results are compared with the slip-line field simulations and the experimental measurements conducted in Section 3.7.2. Identical material properties, tool-chip interaction parameters and cutting conditions are used in both models. It is found that tangential forces from the FE simulations are close to the experimental results, while the feed forces are underestimated. However, the proposed slip-line model predicts both tangential and feed forces with acceptable accuracy. Filice et al. [74] reported the underestimation of the FE simulated feed force compared to the experimental data by 30%. Rech et al. [75] included the tool edge radius in the FE model and showed that the simulated feed forces were less than 50% of the experimental values. Figure 4.10 shows

that the feed force predicted by the FE model increases from 11.5 to 17 N/mm when the uncut chip thickness increases from 20 to 80  $\mu\text{m}$ . The tool–chip contact lengths simulated from the FE model are shown in Figure 4.11 for the uncut chip thickness values of 25, 50 and 80  $\mu\text{m}$ . The tool–chip contact length increases with the uncut chip thickness and the values are given in Table 4.3. FE model using ABAQUS/Explicit allows constant friction stress at the sticking zone (220 MPa here), hence the effects of temperature, strain and strain-rate are not considered. Since the feed force is mainly contributed by the integration of friction stress along the tool–chip contact area, the FE model underestimates the feed force mainly due to the underestimation of the friction stress along the tool-rake face which would be larger if the changes in the material properties are considered more accurately at the contact zone.

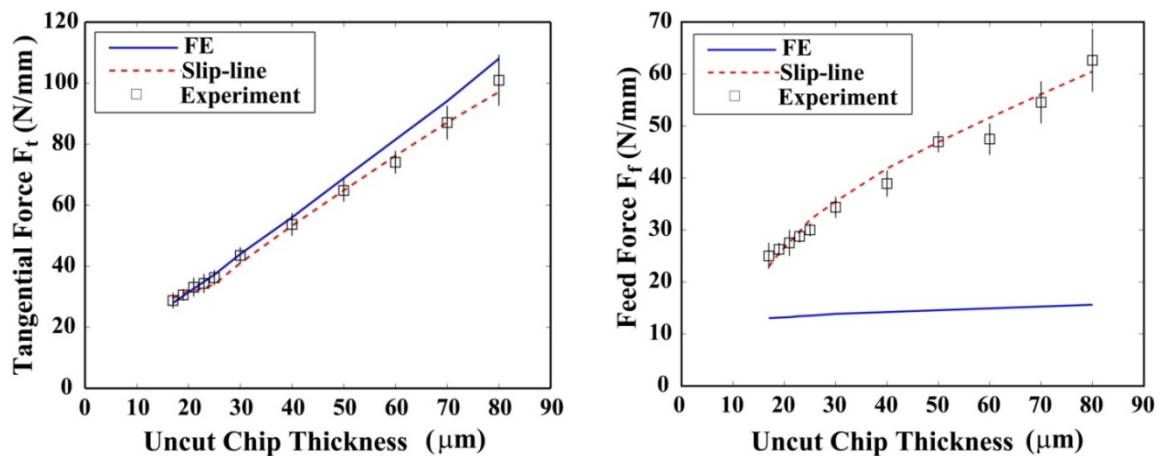
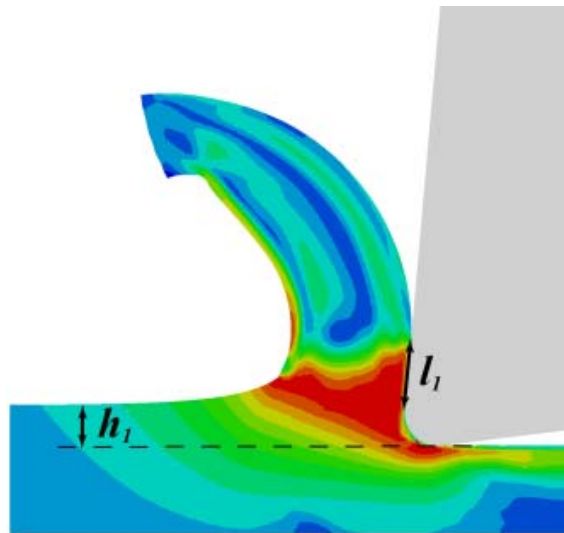
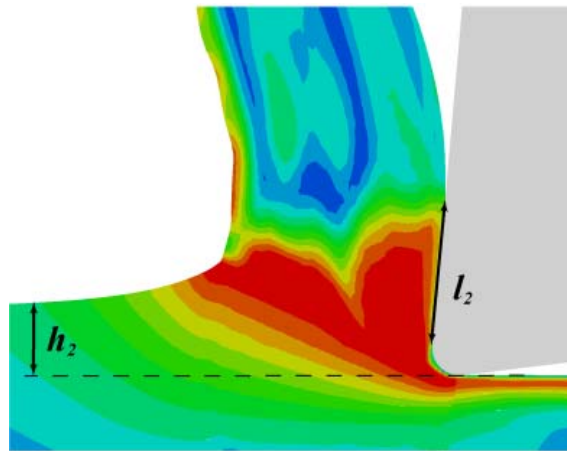


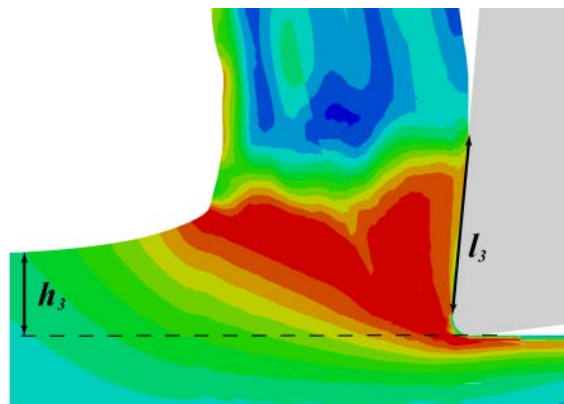
Figure 4.10 Comparison of cutting force prediction from FE model against slip-line field model and experiment. Tool edge radius = 20  $\mu\text{m}$ ; rake angle = 5 deg; clearance angle = 7 deg; cutting velocity = 25 m/min; material: brass 260.



a)  $h_1 = 25 \mu\text{m}$



b)  $h_2 = 50 \mu\text{m}$



c)  $h_3 = 80 \mu\text{m}$

Figure 4.11 Tool-chip contact length predicted by FE model. Tool edge radius =  $20 \mu\text{m}$ , rake angle =  $5 \text{ deg}$ .

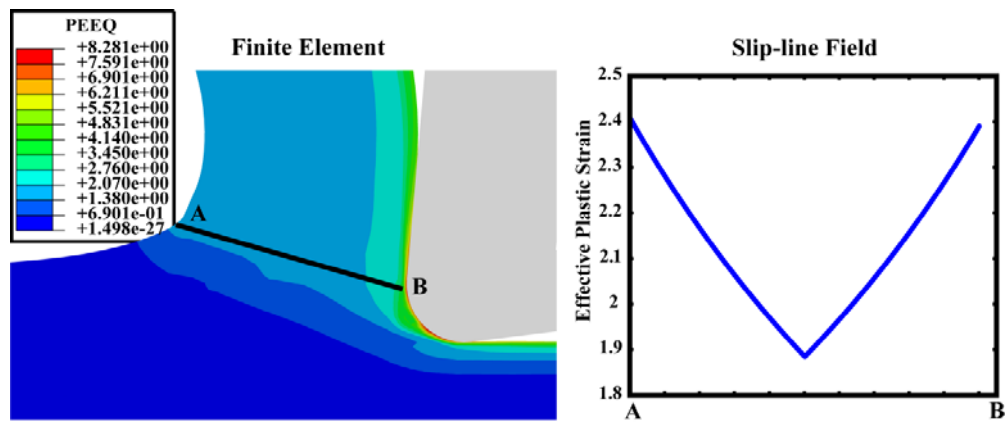
Table 4.3 Tool-chip contact length.

Uncut chip thickness ( $\mu\text{m}$ )	Tool-chip contact length ( $\mu\text{m}$ )
25	42
50	93
80	161

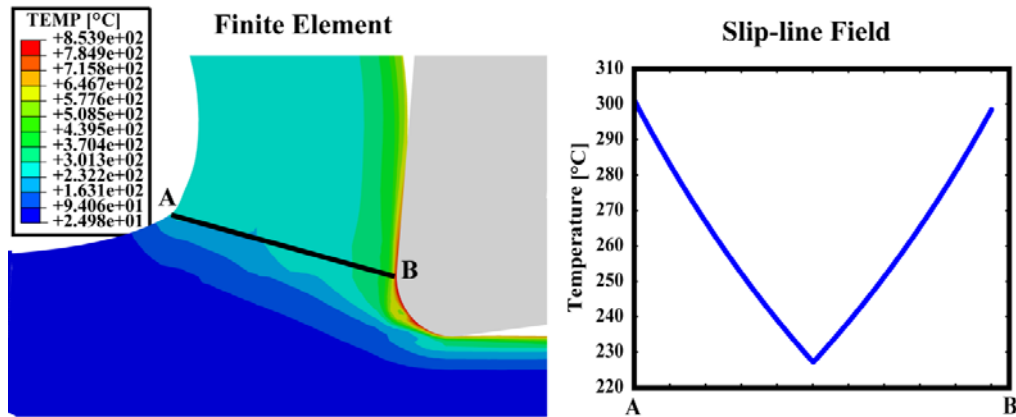
The comparisons of equivalent plastic strain, temperature and Von-Mises stress in the material deformation zones between the FE and slip-line field model are shown in Figure 4.12. The slip-line field results are shown along the upper boundary of the primary shear zone, which corresponds to line AB in the FE simulation. The variation of the results in the primary shear zone (AB) is given in Table 4.4. The predicted equivalent plastic strain (Figure 4.12 a) and the temperature (Figure 4.12 b) values by both methods are in good agreement, and the difference of the maximum Von-Mises stress (Figure 4.12 c) is around 6%. Slip-line field and FE models appear to give similar results in the primary shear zone. However, the FE simulation shows that the temperature in the secondary shear zone rises from 301 °C to 854 °C, which is close to the melting temperature of Brass 260 (916 °C). The high temperature has a thermal softening effect on the flow stress, and the Von-Mises stress decreases from 611 MPa to around 300 MPa in FE model. However, the slip-line field model predicts the temperature at about 300 °C and the Von-Mises stress at around 650 MPa. Since the feed force is mainly influenced by the friction load along the tool rake face, which is determined by the Von-Mises stress, the underestimation of the feed force from FE model is also due to the overestimation of the temperature which leads to reduced friction stress in the secondary shear zone.

Table 4.4 Variation of equivalent plastic strain, temperature and Von-Mises stress in the primary shear zone.

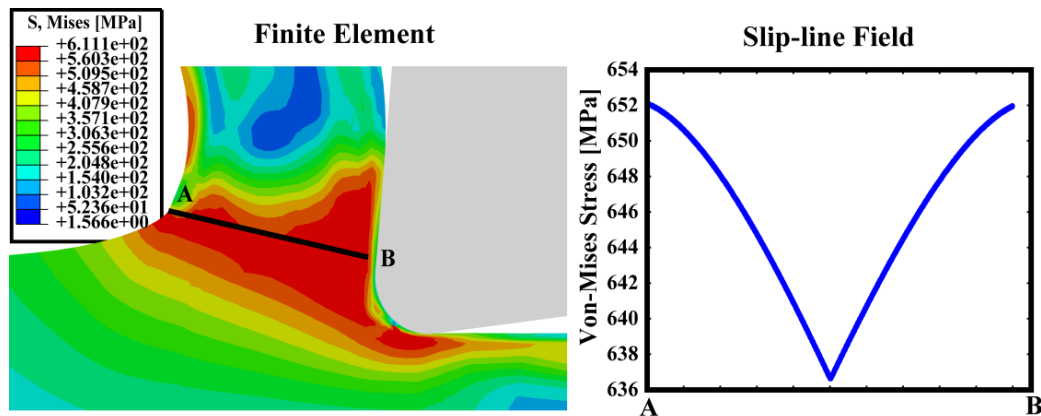
	Equivalent plastic strain [-]	Temperature [°C]	Von-Mises stress [MPa]
FE	[1.38, 2.76]	[232, 301]	[560, 611]
Slip-line field	[1.8, 2.4]	[225, 300]	[636, 652]



a) Predicted equivalent plastic strains.



b) Predicted temperature variations.



c) Predicted Von-Mises stress variations.

Figure 4.12 Comparison of predicted strain, temperature and Von-Misses stresses by FE and slip-line field models in the primary shear zone. Tool edge radius = 20  $\mu\text{m}$ ; rake angle = 5 deg; clearance angle = 7 deg; uncut chip thickness = 25  $\mu\text{m}$ , cutting velocity = 25 m/min. Material: brass 260.

## 4.4 Prediction of micro-milling forces with FE model

Figure 4.13 shows the predicted cutting forces with respect to the uncut chip thicknesses ( $[0.5, 20] \mu\text{m}$ ) and tool edge radii ( $[1, 8] \mu\text{m}$ ) for brass 260 material from the FE model and the slip-line field model (SL). The predicted results are based on the slip-line field and FE simulations from the constitutive properties of the workpiece material and friction parameters, no experimental cutting calibration is required. The procedure of modeling the cutting force coefficients as functions of uncut chip thickness and tool edge radius is explained in Section 3.8.1. By curve fitting the simulated force results in Figure 4.13, the identified constants for Equation (3-66) based on FE and slip-line field models are listed in Table 4.5.

The cutting force coefficients, which are curve fitted to FE and slip-line field based predictions as opposed to cutting force measurements used in mechanistic models, can include chip size, temperature, edge radius and rake angle effects [76].

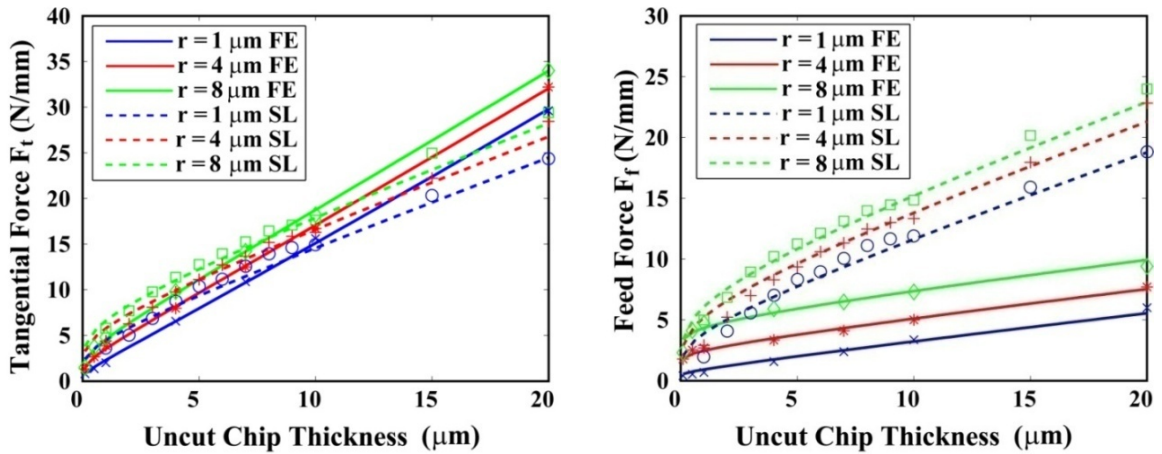


Figure 4.13 Predicted cutting forces. Material: brass 260. Cutting speed = 25 m/min and tool's primary rake angle = 5 deg. Symbols represent the simulated results from FE and slip-line field models, and the solid and dashed lines are the curved-fitted results.

Table 4.5 Constants for the cutting force coefficients of material brass 260 at cutting speed 25 m/min. Units of chip thickness and edge radius are in [mm].

		$\alpha$	$D$	$\beta$	$p$	$q$
FE	$K_t$ [MPa]	1744.0	0.059	181.2	-0.795	0.531
	$K_f$ [MPa]	191.5	-0.054	531.6	-0.918	0.892
Slip-line field	$K_t$ [MPa]	914.4	-0.0004	62.21	-0.814	0.230
	$K_f$ [MPa]	629.4	-0.0002	78.24	-0.787	0.247

Micro-milling forces are predicted including the actual tool tip trajectory and radial run-out of the flutes using the simulation system [69]. Several cutting tests at different spindle speeds and feed rates have been conducted to experimentally validate the simulation results. The experimental setup is described in Section 3.8.3. The cutting conditions are listed in Table 4.6. The tool was inspected for wear and damage after each cut by a microscope integrated to the machine. Speeds between 45,000 and 60,000 rev/min have been deliberately avoided to prevent resonating the two modes (3403 Hz and 3067 Hz) of the dynamometer. The dynamometer's modes are still slightly excited by the harmonics of high tooth passing frequencies (333 Hz, 666 Hz and 1333 Hz), and appeared as distorted oscillations on the raw measurement data. The measured forces are Kalman filtered to compensate the distortion of cutting forces caused by the dynamometer dynamics. The simulations are carried out by using the cutting force coefficients predicted from FE simulations and slip-line field model.

Table 4.6 Cutting conditions for micro-milling test.

Test Number	Tool diameter ( $\mu\text{m}$ )	Spindle speed (rpm)	Feed rate ( $\mu\text{m}/\text{tooth}$ )	Depth of cut ( $\mu\text{m}$ )
1	200	10000	3	50
2	200	20000	3	50
3	200	40000	1	50
4	200	40000	5	50
5	200	40000	7	50

The experimental and simulation results obtained from FE and slip-line field models are given in Figure 4.14 to Figure 4.18. Both the original and Kalman filtered experimental data, as well as the frequency spectrums of the forces are given in the figures. The Kalman filtered results are closer to the simulations compared to the original data. The peak at the frequency of the spindle speed in the FFT of the cutting forces indicates that the tool run-out effect plays an important role in micro-milling operations.

The simulated normal ( $F_y$ ) cutting forces with both FE and slip-line field models, which are more influenced by the tangential component, agree with the experimental results. The frequency content of the forces also shows good agreement between the Kalman filtered experimental results and the simulations. The discrepancy of the cutting forces in X-direction is observed between the FE model and the experiment. This is due to the underestimation of the feed force from the FE model. Since the thermal softening of the material is better handled by the slip-line field model, it predicts the micro-milling forces more accurately in both directions.

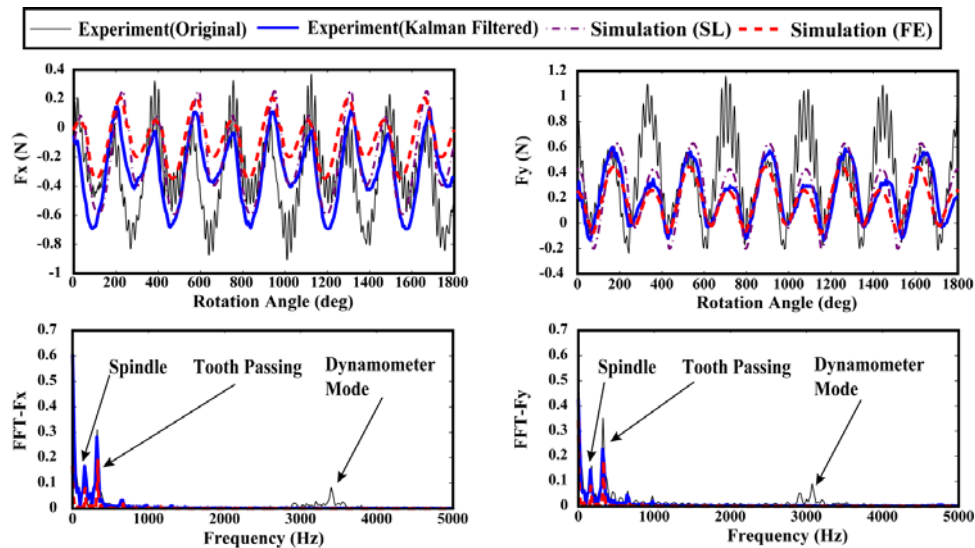


Figure 4.14 Comparison of cutting forces and the frequency spectrums at:  $n = 10,000$  rev/min,  $c = 3 \mu\text{m/tooth}$ ,  $a = 50 \mu\text{m}$ . Material: brass 260.

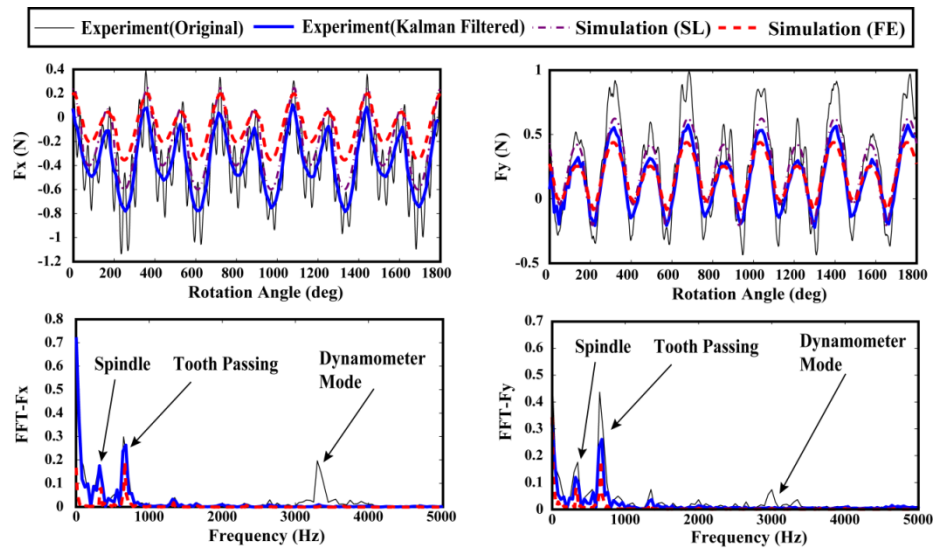


Figure 4.15 Comparison of cutting forces and the frequency spectrums at:  $n = 20,000$  rev/min,  $c = 3 \mu\text{m}/\text{tooth}$ ,  $a = 50 \mu\text{m}$ . Material: brass 260.

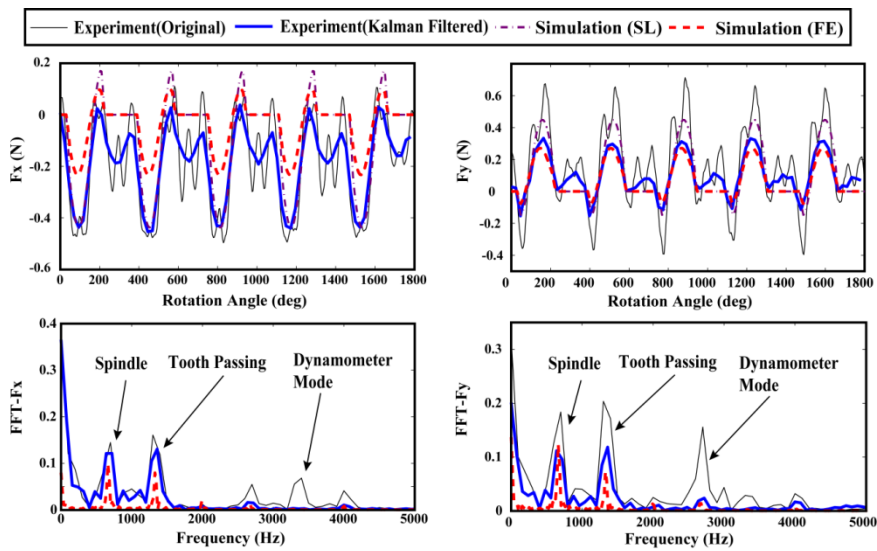


Figure 4.16 Comparison of cutting forces and the frequency spectrums at:  $n = 40,000$  rev/min,  $c = 1 \mu\text{m}/\text{tooth}$ ,  $a = 50 \mu\text{m}$ . Material: brass 260.

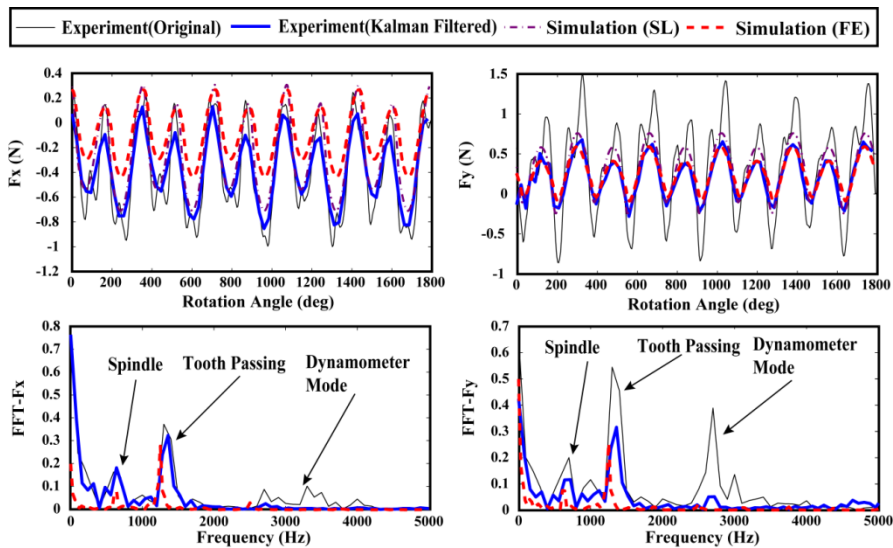


Figure 4.17 Comparison of cutting forces and the frequency spectrums at:  $n = 40,000$  rev/min,  $c = 5 \mu\text{m/tooth}$ ,  $a = 50 \mu\text{m}$ . Material: brass 260.

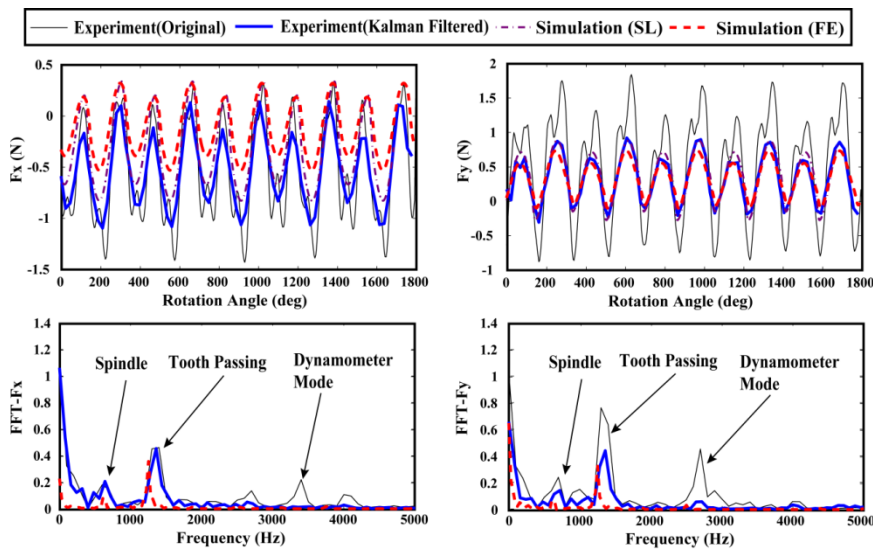


Figure 4.18 Comparison of cutting forces and the frequency spectrums at:  $n = 40,000$  rev/min,  $c = 7 \mu\text{m/tooth}$ ,  $a = 50 \mu\text{m}$ . Material: brass 260.

## 4.5 Microstructure effect on micro-cutting process

The chip formation and cutting forces are affected by material microstructure in micro-cutting of workpiece with multiple phases. Figure 4.19 shows the microstructure of normalized AISI 1045 steel sample from metallurgical observation. The light regions show the ferrite grains and the dark regions are the pearlite colonies. The average size of ferrite

grains is measured to be  $18\ \mu\text{m}$ , which is comparable with the uncut chip thickness and tool edge radius in size. The heterogeneity of workpiece material is caused by the difference of constitutive property between ferrite and pearlite grains.

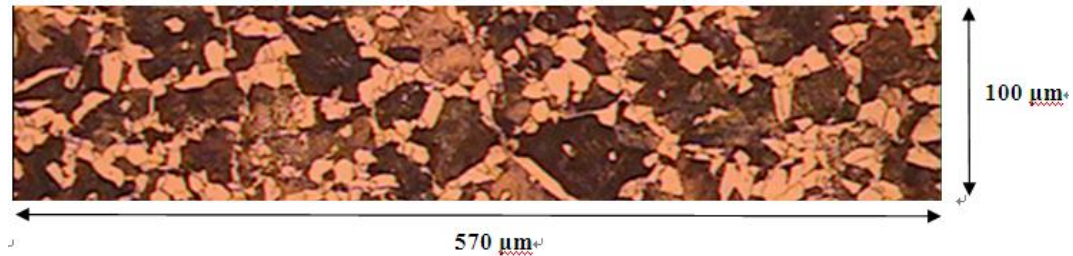


Figure 4.19 Microstructure of normalized AISI 1045 steel.

The FE method is used to include the material microstructure in simulating the cutting process. Figure 4.19 is converted into binary image representing the distributions of ferrite and pearlite respectively, shown as Figure 4.20 with the resolution of  $475 \times 100$ . The pixels in the figure are divided into two groups from the binary values, and then mapped into the meshing elements of the workpiece in the FE model, shown as Figure 4.21.



Figure 4.20 Binary image converted from Figure 4.19.



Figure 4.21 FE model of workpiece material with ferrite and pearlite phases.

The constitutive properties of ferrite and pearlite phases are based on the stress-strain curves shown in Figure 4.22, which is obtained from tensile tests for various single

structure steels [77]. The stress-strain curves show the strain-hardening effect on the flow stress for each phase. For ferrite and pearlite, the strain-hardening related parameters  $A, B, n$  in Johnson-Cook equation (3-15) are identified by curve fitting the stress-strain curves and given in Table 4.7. The strain-rate and temperature related parameters are assumed the same for two phases, and the values are borrowed from the split Hopkinson bar test results conducted by Jaspers and Dautzenberg for AISI 1045 steel [78].

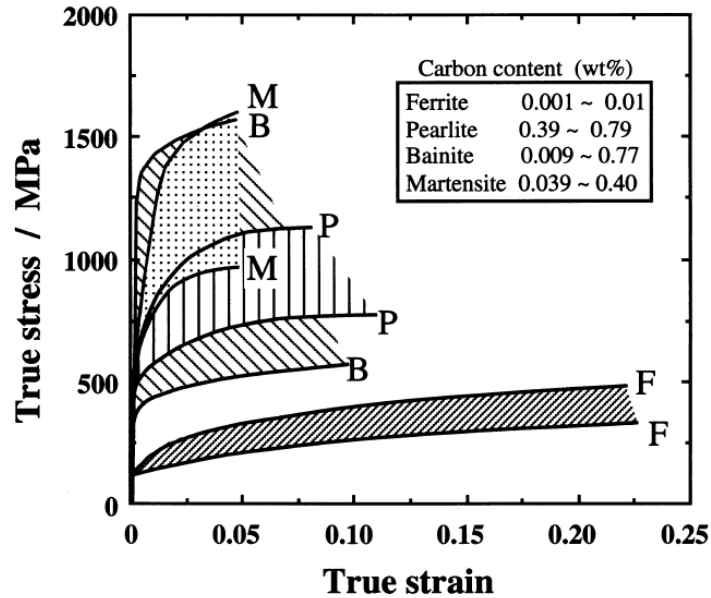


Figure 4.22 Stress-strain curves for various single structure steels [77].

Table 4.7 Johnson-Cook parameters and cutting conditions in FE simulation.

Material	$A$	$B$	$n$	$C$	$m$	$T_m$
Ferrite	115.2	640.4	0.477	0.0134	1	1479
Pearlite	442.7	1152	0.294	0.0134	1	1479
1045 Steel [78]	553.1	600.8	0.234	0.0134	1	1479

Two FE simulations are conducted with heterogeneous and homogeneous 1045 workpiece materials, respectively. The effect of round tool edge is included. Since the adaptive ALE meshing algorithm is not effective when the workpiece includes two types of materials in ABAQUS/Explicit, the fracture criterion of workpiece elements is defined. It is assumed that pearlite elements have a shear failure criterion of 1.8 and the softer ferrite

elements have a shear failure criterion of 2.2 [79]. The cutting condition of the two FE simulations is listed in Table 4.8.

Table 4.8 Cutting condition in the FE model.

Tool edge radius [ $\mu\text{m}$ ]	20
Uncut chip thickness [ $\mu\text{m}$ ]	25
Cutting speed [m/min]	200

The chip formation with heterogeneous workpiece material is shown in Figure 4.23. The softer material phase ferrite is extruded as well as sheared during the cutting process, resulting into the variation of chip thickness. Material fracture around the tool edge causes uneven surface finish. The chip formation of the FE simulation assuming homogeneous 1045 steel workpiece material is given in Figure 4.24, which shows a constant chip thickness in steady-state cutting process.

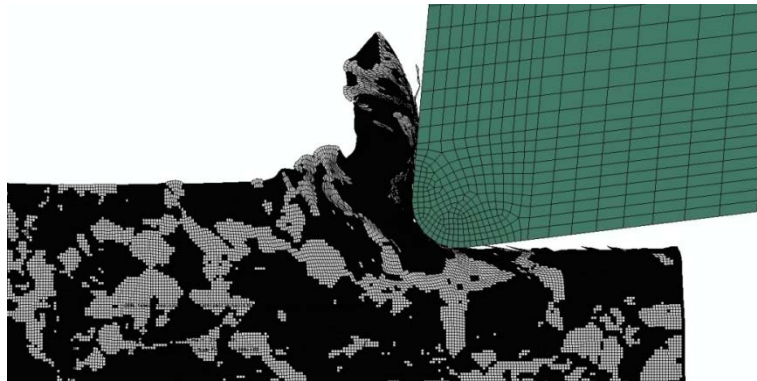


Figure 4.23 Chip formation with heterogeneous workpiece material.

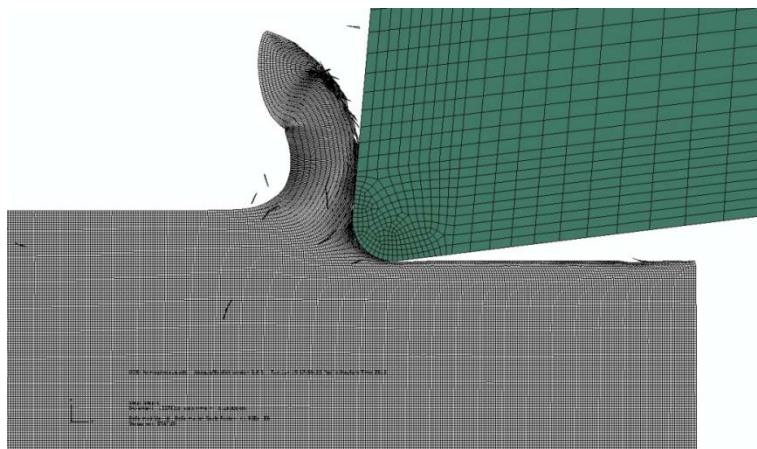


Figure 4.24 Chip formation with homogeneous workpiece material.

The simulated tangential and feed forces with heterogeneous and homogeneous workpiece materials are shown in Figure 4.25. Since ALE adaptive meshing technique is not applied in the FE model, the frequent deletion of workpiece elements which satisfy the failure criterion around tool edge causes the oscillations of cutting forces. However, the difference of average cutting forces between the heterogeneous and homogeneous materials is less than 10% in both tangential and feed directions.

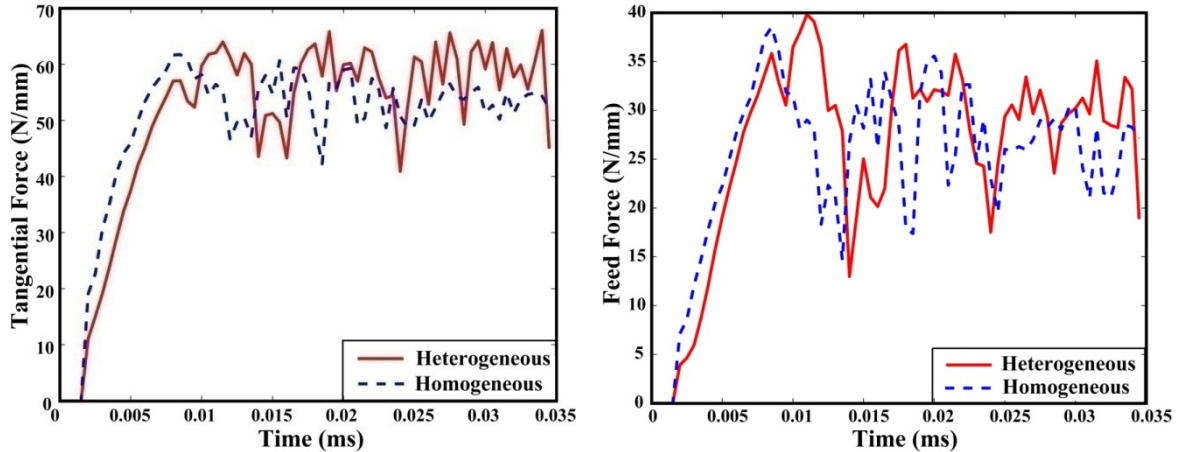


Figure 4.25 Cutting forces with heterogeneous and homogeneous materials.

## 4.6 Conclusion

This chapter presents the prediction of micro-milling forces from the FE model for Brass 260. Based on the material constitutive model and identified tool–chip contact parameters, the FE model shows the effect of tool edge geometry, uncut chip thickness and cutting speed on the force prediction. The material separation angle is obtained from the finite element simulation by investigating the velocity direction of the material around the tool edge. The predicted cutting force from FE model is compared against the slip-line field simulation and turning experimental results. While assumption of constant friction stress and overestimation of the temperature in the secondary shear zone cause underestimation of feed force in the FE model, the friction stress is updated as a function of changing material properties in the slip-line field model. As a result, slip-line field model presents more accurate prediction of feed force. Based on the simulation results, the cutting force coefficients are identified as nonlinear functions of chip thickness and tool edge radius

from FE and slip-line field models independently. The cutting coefficients are then used in milling model which considers the tool tip trajectory, radial run-out and dynamics of the dynamometer. It is shown that the micro-milling forces in normal direction can be predicted accurately, but estimated less accurately in the feed direction due to the aforementioned friction model used in the FE model. If the friction model is improved, the FE model can also estimate the feed forces as accurately as the slip-line field model. Moreover, when the rake face has chip breaking and lubrication grooves, which are more common in macro-cutting tools, FE model can be more effective than slip-line field models provided that the friction model is improved. FE model is also able to simulate the chip formation process with workpiece material having multiple phases, while the slip-line field model only considers the steady state cutting process assuming homogeneous workpiece material. FE simulation of micro-cutting with normalized 1045 steel shows the variation of chip thickness due to different constitutive properties between ferrite and pearlite phases, and the fracture of workpiece material elements around cutting edge causes uneven surface finish.

# Chapter 5

## Dynamic Modeling of Micro-milling Process<sup>3</sup>

### 5.1 Overview

This chapter presents the prediction of chatter stability in micro-milling by considering the process damping caused by round cutting edge and the micro-mill dynamics in high frequency range. The cutting forces are predicted from the material's properties and tool geometry using the slip-line field model. FRF in the frequency range of 0.5 - 120 kHz at tool tip is measured directly by a specially designed miniature piezoelectric actuator attached to the micro-mill shank when the tool is clamped in the spindle. Process damping coefficient is identified by the FE model of micro-cutting with round cutting edge. Chatter stability lobes are predicted in frequency domain by using the cutting force and process damping coefficients identified from the constitutive model of the material, and directly measured FRF of the micro-mill. The model is experimentally verified by micro-milling of AISI 1045 steel.

Henceforth, the content of the chapter is organized as follows. The dynamic cutting force model of micro-milling is presented in section 5.2. The identification of cutting force and process damping coefficients is explained in section 5.3. The chatter stability prediction model is presented in section 5.4, followed by experimental validation in section 5.5 and conclusion in section 5.6.

### 5.2 Dynamic cutting force model in micro-milling process

The micro mill has lateral flexibilities in feed ( $x$ ) and normal ( $y$ ) directions as shown in Figure 5.1. The regenerative chip thickness removed by flute  $j$  when it is at an angular position  $\phi_j(t) = \Omega t + (j-1)\phi_p$  can be expressed as [2]:

---

3. The content of Chapter 5 has been submitted for review.

$$\begin{cases} h_j(\phi_j) = c \sin \phi_j + v(t) - v(t - T_p) \\ v(t) = x(t) \sin \phi_j + y(t) \cos \phi_j \end{cases} \quad (5-1)$$

where  $C$  is the feed per tooth,  $\Omega$  [rad / s] is the angular velocity of the spindle,  $T_p$  is the tooth period,  $[x(t), y(t)]$  and  $[x(t - T_p), y(t - T_p)]$  are the vibrations of the tool at the present ( $t$ ) and previous ( $t - T_p$ ) tooth periods, respectively. The pitch angle of the cutter is given by  $\phi_p = 2\pi / N$  for a micro-mill with ( $N$ ) number of teeth. The cutting forces have three components when the micro mill vibrates: static forces due to rigid body motion of the cutting edge ( $c \sin \phi_j$ ); dynamic forces due to regenerative chip thickness [ $v(t) - v(t - T_p)$ ]; and process damping forces caused by the contact between the round edge of the tool and wavy surface finish [80]. The tangential ( $F_{tj}$ ) and radial ( $F_{rj}$ ) cutting forces acting on a cutting edge with an axial depth of cut ( $a$ ) is expressed as:

$$\begin{cases} F_{tj}(\phi_j) = K_t ah(\phi_j) + C_t a \frac{\dot{v}}{V_c} \\ F_{rj}(\phi_j) = K_r ah(\phi_j) + C_r a \frac{\dot{v}}{V_c} \end{cases} \quad (5-2)$$

where ( $V_c$ ) is the cutting speed, the vibration velocity is expressed as:

$$\dot{v} = dv / dt = \dot{x}(t) \sin \phi_j + \dot{y}(t) \cos \phi_j \quad (5-3)$$

( $C_t$ ) and ( $C_r$ ) are the process damping coefficients in tangential and radial directions, respectively. The tangential and radial forces are projected in feed ( $x$ ) and normal ( $y$ ) directions as:

$$\begin{cases} F_x(t) = \sum_{j=1}^N [-F_{tj}(\phi_j) \cos \phi_j - F_{rj}(\phi_j) \sin \phi_j] \\ F_y(t) = \sum_{j=1}^N [+F_{tj}(\phi_j) \sin \phi_j - F_{rj}(\phi_j) \cos \phi_j] \end{cases} \quad (5-4)$$

By substituting the chip thickness (Equation (5-1)) and vibration velocity  $\dot{v}$

(Equation (5-3)) into Equations (5-2) and (5-4), the dynamic micro-milling forces with static ( $F_{st}(t)$ ), regenerative ( $F_{rc}(t)$ ) and process damping ( $F_{pd}(t)$ ) parts are derived as:

$$\{F(t)\} = \begin{Bmatrix} F_x(t) \\ F_y(t) \end{Bmatrix} = \{F_{st}(t)\} + \{F_{rc}(t)\} + \{F_{pd}(t)\} \quad (5-5)$$

where

$$\begin{aligned} F_{st}(t) &= K_t a c \sum_{j=1}^N \begin{Bmatrix} (-\sin \phi_j \cos \phi_j - k_r \sin^2 \phi_j) \\ (\sin^2 \phi_j - k_r \sin \phi_j \cos \phi_j) \end{Bmatrix} \\ F_{rc}(t) &= K_t a \sum_{j=1}^N \begin{bmatrix} -\sin \phi_j \cos \phi_j - k_r \sin^2 \phi_j & -\cos^2 \phi_j - k_r \sin \phi_j \cos \phi_j \\ \sin^2 \phi_j - k_r \sin \phi_j \cos \phi_j & \sin \phi_j \cos \phi_j - k_r \cos^2 \phi_j \end{bmatrix} \begin{Bmatrix} \Delta x(t) \\ \Delta y(t) \end{Bmatrix} = K_t a A_m \cdot \Delta v \\ F_{pd}(t) &= \frac{C_r a}{V_c} \sum_{j=1}^N \begin{bmatrix} -c_t \sin \phi_j \cos \phi_j - \sin^2 \phi_j & -c_t \cos^2 \phi_j - \sin \phi_j \cos \phi_j \\ c_t \sin^2 \phi_j - \sin \phi_j \cos \phi_j & c_t \sin \phi_j \cos \phi_j - \cos^2 \phi_j \end{bmatrix} \begin{Bmatrix} \dot{x}(t) \\ \dot{y}(t) \end{Bmatrix} = C_r a B_m \cdot \dot{v} \end{aligned} \quad (5-6)$$

The dimensionless constants are defined as  $k_r = K_r / K_t$  and  $c_t = C_t / C_r$ .  $A_m$  and  $B_m$  are directional matrices that are periodic at tooth passing intervals.  $\Delta v = \{\Delta x \ \Delta y\}^T$  is the regenerative vibration vector, and  $\dot{v} = \{\dot{x} \ \dot{y}\}^T$  is the vibration velocity vector.

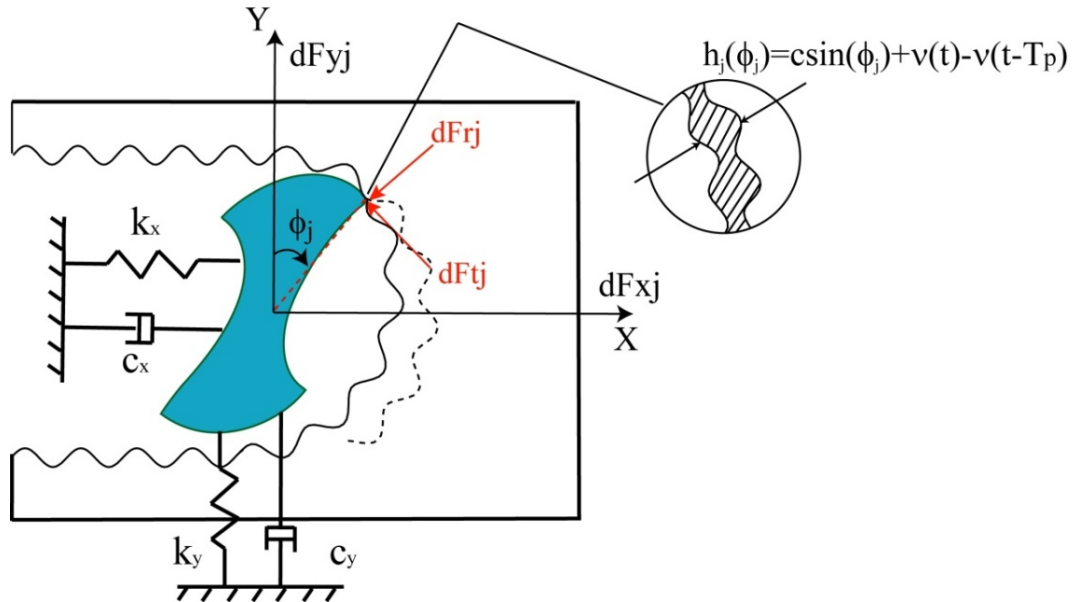


Figure 5.1 Dynamic micro-milling system.

## 5.3 Identification of cutting force and process damping coefficients

The prediction of static, regenerative and process damping forces require the identification of cutting force ( $K_t, K_r : [N/m^2]$ ) and process damping ( $C_t, C_r : [N/m]$ ) coefficients for a micro tool with round cutting edge. Unlike in macro milling, the chip thickness is usually as small or less than the cutting edge radius in micro-cutting. As a result, the cutting force and process damping coefficients, which are estimated using the plasticity models here, are highly sensitive to edge radius and chip thickness in micro-milling.

### 5.3.1 Identification of cutting force coefficients

The cutting force coefficients are identified directly from the material's constitutive model by using slip-line field simulations. The Johnson-Cook parameters for AISI 1045 steel are borrowed from Jaspers and Dautzenberg [78] who calibrated them from split Hopkinson pressure bar tests, see Figure 5.2. In the slip-line model, the AISI 1045 steel is assumed as homogeneous material. A number of orthogonal turning simulations have been carried out for a range of cutting edge radius ( $r \in [1, 8] \mu m$ ) and chip thickness ( $h \in [1, 12] \mu m$ ) as shown in Figure 5.2. The cutting force coefficients are modeled as functions of uncut chip thickness and tool edge radius shown in Equation (3-66). The constants in Equation (3-66) are identified by curve fitting the simulation data shown in Figure 5.2 and the values are listed in Table 5.1 when the unit of uncut chip thickness and the tool edge radius is in millimeter.

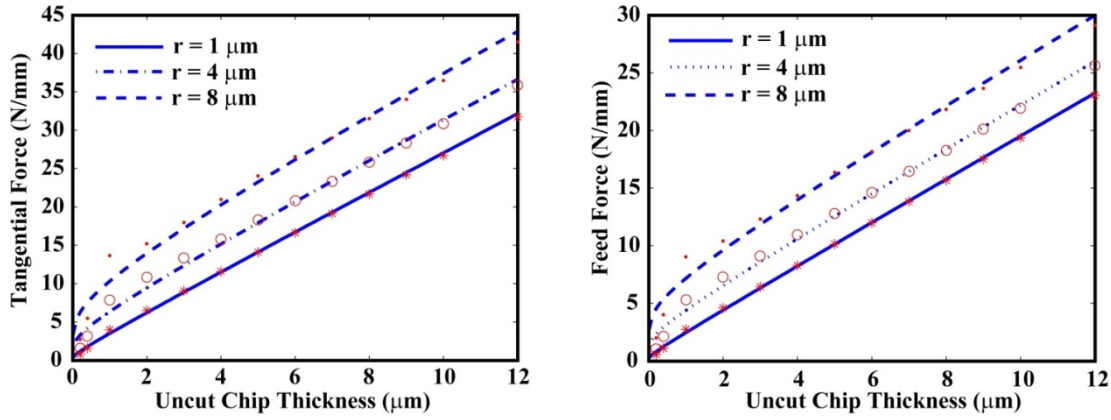


Figure 5.2 Cutting forces predicted by slip-line field model (Material: AISI 1045 steel.  $A=553.1\text{MPa}$ ,  $B=600.8\text{MPa}$ ,  $C=0.013$ ,  $n=0.234$ ,  $m=1$ ,  $T_m=1460\text{ }^\circ\text{C}$  and  $T_r=25\text{ }^\circ\text{C}$ ). Symbols represent the simulated results from slip-line field model, and the lines show the curved-fitted results.

Table 5.1 Cutting force coefficients in Equation (3-66) for AISI 1045 steel.

	$\alpha$	$d$	$\beta$	$p$	$q$
$K_t$ [N/mm <sup>2</sup> ]	2447	-0.0108	4305	-0.8176	1.050
$K_r$ [N/mm <sup>2</sup> ]	1796	-0.0094	2723	-0.8557	1.088

The validity of the cutting force coefficients are experimentally demonstrated in series of chatter free slot-milling of AISI 1045 steel with 21 HRC hardness. A two-fluted carbide micro end mill with 400 μm diameter and zero rake angle was used. The spindle speed was 9000 rev/min with a feed rate of  $c = 7\mu\text{m}/\text{tooth}$  and axial depth of  $a = 10\mu\text{m}$ . The cutting force coefficients identified from the slip-line field model are used in static force model ( $\mathbf{F}_{st}(t)$ ) given in Equation (5-6). The predicted and experimentally measured micro-milling forces are compared shown in Figure 5.3. Kalman filter algorithm has been used to compensate the distortion of cutting forces caused by the dynamometer dynamics.

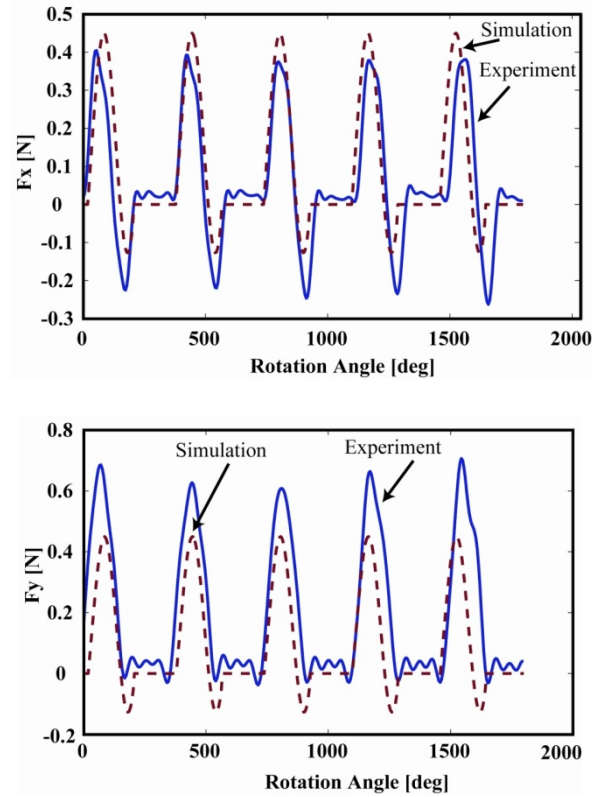


Figure 5.3 Comparison of micro-milling forces predicted by slip-line field model and experiment.

### 5.3.2 Identification of process damping coefficients

The process damping is contributed by the contact between the wavy surface finish and round cutting edge of the tool at the clearance face side. The process damping coefficients are predicted by modeling the contact mechanics through finite element simulation of the oscillating tool as shown in Figure 5.4. The FE model is based on Abaqus/Explicit 6.8-3, and the flow stress properties of AISI 1045 steel are given in Figure 5.2. The cutting forces in the cutting velocity ( $x$ ) and normal ( $y$ ) directions can be expressed as:

$$\begin{cases} F_t(t) = K_t a h_0 + K_t a [-y(t) - y(t - T_p)] + C_t a \frac{\dot{y}(t)}{V_c} \\ F_r(t) = K_r a h_0 + K_r a [-y(t) - y(t - T_p)] + C_r a \frac{\dot{y}(t)}{V_c} \end{cases} \quad (5-7)$$

The equation of motion of the undamped tool, that is flexible only in normal direction,

is given by:

$$\ddot{y}(t) + \omega_y^2 y(t) = \frac{\omega_y^2}{k_y} F_r(t) \quad (5-8)$$

where  $\omega_y, k_y$  are natural frequency and stiffness of the oscillating tool, respectively. The cutting force coefficients ( $K_t, K_r$ ) are identified by simulating rigid tool shearing the material as explained in the previous section. The process damping coefficients are identified from the finite element simulation of the ploughing forces between material separation point (S) on the edge radius and point (A) where the contact is lost with the wavy surface, see Figure 5.4-a. An initial chip thickness is assumed for the chip formation simulation, and the material is cut with a cutting velocity of ( $V_c$ ) in tangential direction.

Total ploughing forces have static ( $F_0$ ) and process damping ( $C_a \dot{y}(t)/V_c$ ) components as:

$$\begin{cases} F_{pt}(t) = F_{pt0} + C_t a \dot{y}(t)/V_c \\ F_{pr} = F_{pr0} + C_r a \dot{y}(t)/V_c \end{cases} \quad (5-9)$$

where the velocity of tool vibration is:

$$\dot{y}(t) = y \sin(\omega t) \quad (5-10)$$

The energy dissipated by the ploughing forces in one vibration period ( $\tau_p$ ) is:

$$\begin{cases} E_{pt} = \int_0^{\tau_p} (F_{pt0} + C_t a \dot{y}(t)/V_c) \dot{y}(t) dt = \int_0^{\tau_p} (C_t a \dot{y}(t)/V_c) \dot{y}(t) dt \\ E_{pr} = \int_0^{\tau_p} (F_{pr0} + C_r a \dot{y}(t)/V_c) \dot{y}(t) dt = \int_0^{\tau_p} (C_r a \dot{y}(t)/V_c) \dot{y}(t) dt \end{cases} \quad (5-11)$$

The process damping coefficients are identified from the dissipated energy [52] in each direction as follows:



tool with flank wear land of  $(L_w)$ , see Figure 5.4-b. The process damping force model with the tool wear length  $(L_w)$  effect is expressed as:

$$F_{pr} = C_r \frac{a}{V_c} \dot{y} = K_{sp} \frac{L_w^2}{2} \cdot \frac{a}{V_c} \dot{y} \quad (5-13)$$

The contact force coefficient  $K_{sp}$  is independent of the tool geometry and cutting speed, and it is influenced by the elastic-plastic properties of the workpiece material. The flow stress and physical properties of the workpiece material (AISI 1045) are given in Figure 5.2 and in Table 5.2, respectively. A tool with zero rake angle and 80  $\mu\text{m}$  flank wear was used in both simulations and experiments. The cutting conditions in simulations and dynamics cutting tests are given in Table 5.2. Tool displacement ( $y$ ), vibration velocity ( $\dot{y}$ ), and the resulting normal contact forces ( $F_{pr}$ ) in radial direction ( $y$ ) are simulated for two vibration cycles as shown in Figure 5.5. The decay of tool vibration amplitude shows the energy dissipation due to the process damping effect.

Table 5.2 Physical parameters of AISI 1045 steel and cutting condition.

Physical parameters		Cutting condition		
Density [kg/m <sup>3</sup> ]	7870	Tool Geometry	Rake Angle [°]	0
Elastic Modulus [GPa]	200		Clearance Angle [°]	7
Poisson's Ratio	0.3		Edge Radius [ $\mu\text{m}$ ]	20
Conductivity [W/m/ °C]	51.9		Tool Wear Length [ $\mu\text{m}$ ]	80
Specific Heat [J/kg/ °C]	486	Modal Stiffness [N/m]		6.94e6
Inelastic Heat Fraction	0.9	Natural Frequency [Hz]		1500
		Cutting Velocity [m/min]		55

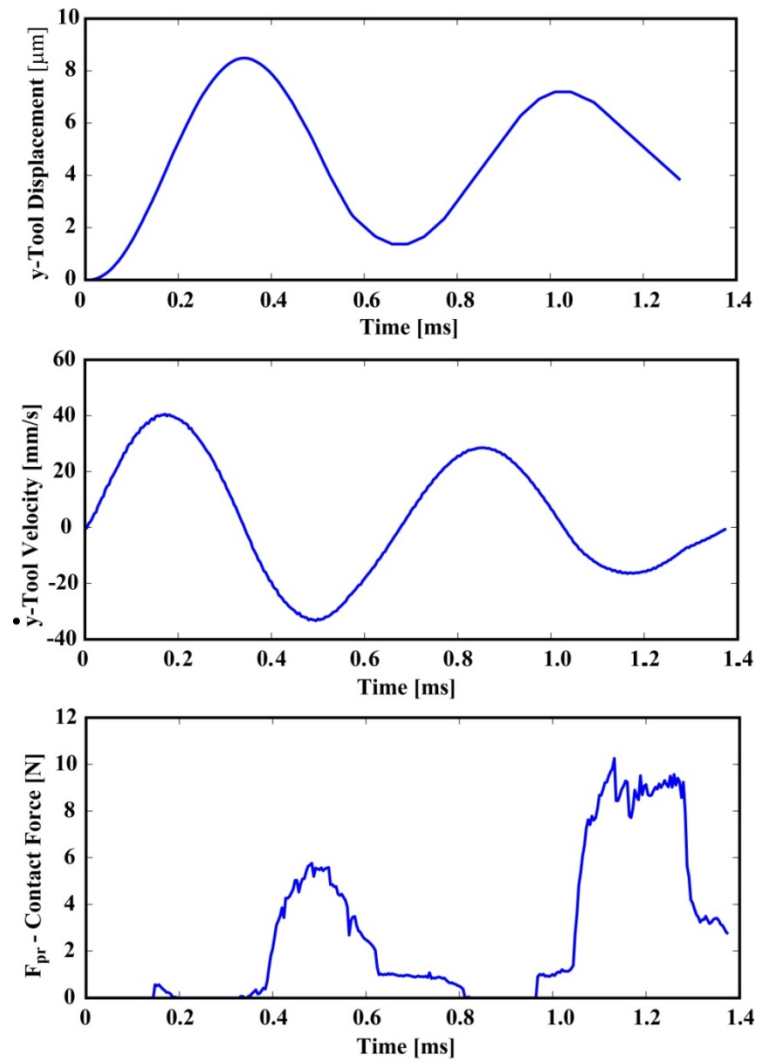


Figure 5.5 FE simulation of displacement, velocity and contact force in orthogonal cutting of AISI 1045 with a tool having 80  $\mu\text{m}$  flank wear.

The contact force is positive when the tool velocity is negative, showing that flank wear - workpiece contact occurs when the tool is traversing downwards. Tool disengages from the finish surface when the tool velocity is positive; hence the contact forces become zero. The average process damping coefficients are found from the FE simulations as follows:

$$\begin{cases} C_{pr1} = 0.462 \times 10^5 [N / m] \\ C_{pr1} = 1.54 \times 10^5 [N / m] \end{cases} \quad (5-14)$$

Coulomb friction becomes dominant when the flank wear is simulated with flat clearance face, i.e.  $C_{pr1} / C_{pr1} \approx 0.3$  which is the Coulomb friction used in FE simulations. The contact force coefficient ( $K_{sp}$ ) for AISI 1045 steel is evaluated from Equation (5-14) as:

$$K_{sp} = \frac{2 \cdot C_{pr1}}{L_w^2} = 4.82 * 10^{13} \left[ N / m^3 \right] \quad (5-15)$$

Eynian and Altintas [50] identified the contact force coefficient for AISI 1045 steel from piezo-actuator controlled indentation tests for the same worn tool, and the range was within  $K_{sp} = \left[ 3.2 * 10^{13} N / m^3, 4.7 * 10^{13} N / m^3 \right]$ . The discrepancy between the FE identified results and the experimental results may originate from the meshing of the workpiece and tool in the FE model. On the other hand, the indentation experiment is a quasi-static procedure, which doesn't include the strain-rate or temperature effects. Overall, the contact force coefficients obtained from the proposed FE simulation and experiments are in reasonable agreement, hence they can be extended to the identification of process damping in micro-milling.

The cutting edge radius of a two fluted micro-end mill with 600  $\mu\text{m}$  diameter is measured as 4  $\mu\text{m}$  with an optical microscope as shown in Figure 5.6. The rake and clearance angles were measured as zero and ten degrees, respectively.

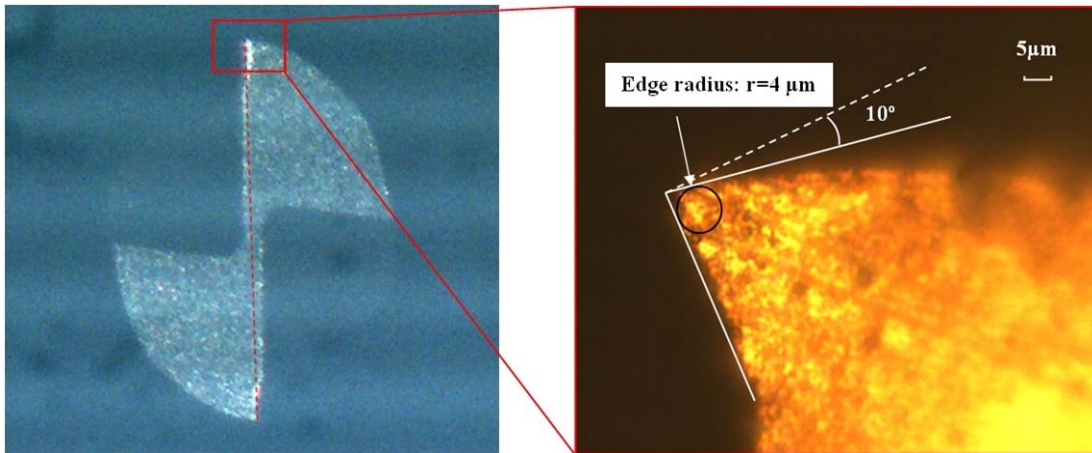


Figure 5.6 Measurement of tool edge geometry under optical microscope.

The FE model of orthogonal micro-cutting is set up based on the measured geometric

parameters of the tool edge. An undamped single degree of freedom oscillator (Equation (5-8)) with natural frequency 3800 Hz and stiffness of 0.89 N/m was used in FE simulations. The width of cut and the cutting velocity were 0.1 mm and 55 m/min, respectively. Tool displacement ( $y$ ), vibration velocity ( $\dot{y}$ ), and the resulting normal contact forces ( $F_{pr}$ ) in radial direction ( $y$ ) are simulated as shown in Figure 5.7.

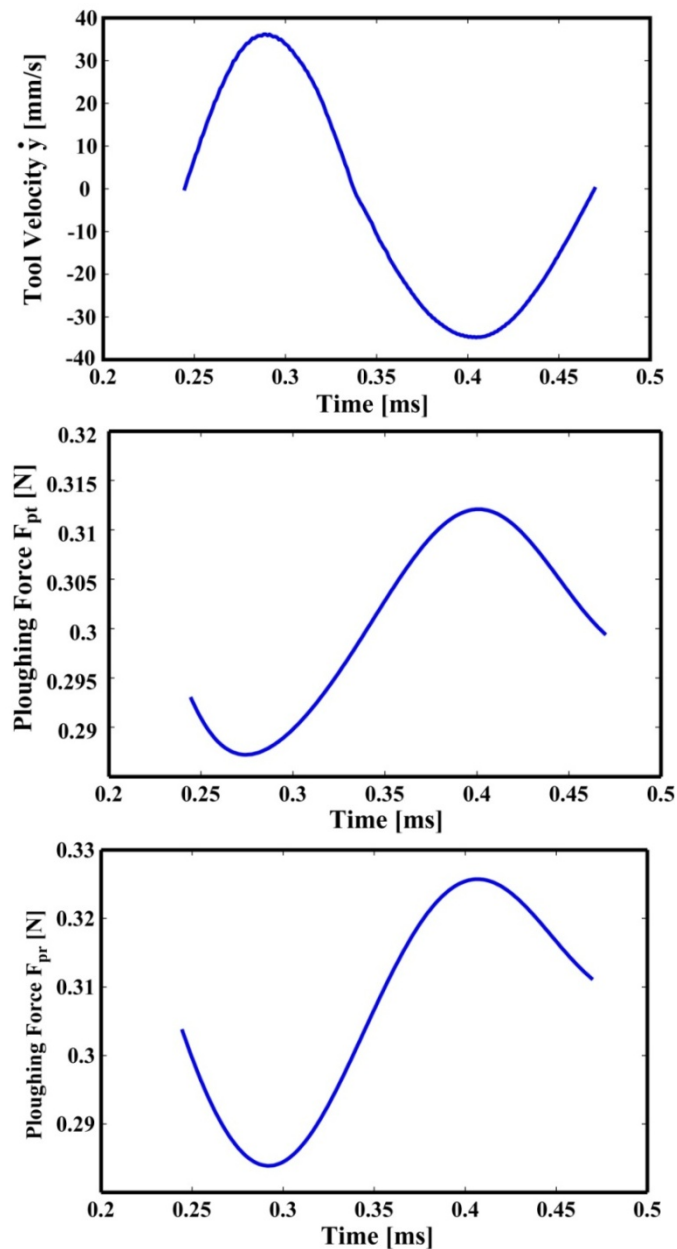


Figure 5.7 FE simulations of displacement, velocity and contact force in orthogonal cutting of AISI 1045 with a micro-tool.

The process damping coefficients in tangential and radial directions are estimated from Equation (5-12):

$$\begin{cases} C_{pt2} = 1.872 \times 10^4 [N/m] \\ C_{pr2} = 2.136 \times 10^4 [N/m] \end{cases} \quad (5-16)$$

The ratio of process damping coefficients between X and Y-directions is  $C_{pt2}/C_{pr2} = 0.877$  which is far greater than Coulomb friction coefficient which was set to be 0.3 in FE simulations. Unlike in macro-cutting case with tool wear land, the directions of contact forces in micro-cutting changes continuously along the round cutting edge which affect the ploughing of the finish surface.

## 5.4 Prediction of chatter stability in micro-milling

The chatter vibration system is presented by the block diagram shown in Figure 5.8, where the parameters of the dynamic cutting process are shown in the Laplace domain. Input to the system is the desired chip thickness  $h_0$ , and the output of the feedback system is the current vibration  $v(t)$  left on the inner surface of the workpiece shown in Figure 5.1. In the Laplace domain,  $v(s) = \mathcal{L}v(t)$ , and the vibration imprinted on the outer surface during the previous revolution is  $e^{-sT_p}v(s) = \mathcal{L}v(t - T_p)$ , where  $T_p$  is the spindle period.

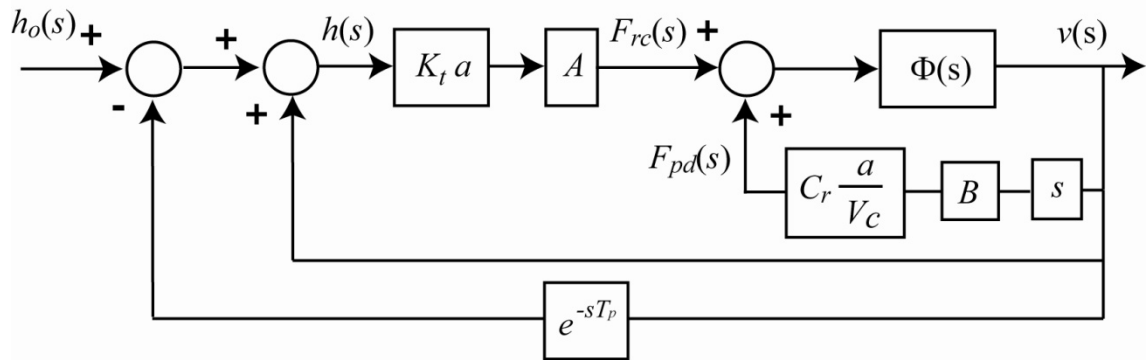


Figure 5.8 Block diagram of chatter dynamics with process damping.

The range of natural frequencies vary from 500Hz (i.e. spindle mode) to 120,000Hz (i.e. fluted section) in micro-milling, hence the process damping of high frequency modes are crucial in predicting the stability. The stability of micro-milling is investigated in

frequency domain by removing the forced excitation part ( $\mathbf{F}_{st}(t)=0$ ) in Equation (5-5), and considering the self excitation part of the dynamic forces as:

$$F_{dn}(t) = K_t a A(t) \cdot \Delta v(t) + \frac{C_r a}{V_c} B(t) \cdot \dot{v}(t) \quad (5-17)$$

Periodic directional coefficients are averaged over a tooth period (i.e. pitch angle) to eliminate their time dependency as:

$$\bar{A} = \frac{1}{\phi_p} \int_{\phi_{st}}^{\phi_{ex}} A(\phi) d\phi, \quad \bar{B} = \frac{1}{\phi_p} \int_{\phi_{st}}^{\phi_{ex}} B(\phi) d\phi \quad (5-18)$$

By substituting the averaged directional factors into Equation (5-17), the dynamic micro-milling force can be expressed in Laplace domain as:

$$F_{dn}(s) = K_t a \bar{A} \cdot (1 - e^{-sT_p}) v(s) + s \frac{C_r a}{V_c} \bar{B} \cdot v(s) \quad (5-19)$$

The vibration vector is expressed as the product of transfer function of the structure at the tool tip ( $\Phi(s)$ ) and dynamic force vector  $\mathbf{F}_{dn}(s)$ :

$$v(s) = \Phi(s) F_{dn}(s) \rightarrow \Phi(s) = \begin{bmatrix} \Phi_{xx}(s) & \Phi_{xy}(s) \\ \Phi_{yx}(s) & \Phi_{yy}(s) \end{bmatrix} \quad (5-20)$$

The transfer function of the system with process damping is reduced to an eigenvalue problem as follows:

$$\begin{aligned} \left[ \mathbf{I} - s \frac{C_r a}{V_c} \bar{\mathbf{B}} \Phi(s) \right] F_{dn}(s) &= K_t a (1 - e^{-sT_p}) \bar{A} \Phi(s) F_{dn}(s) \\ F_{dn}(s) &= K_t a (1 - e^{-sT_p}) \bar{A} \Phi(s) \cdot \left[ \mathbf{I} - s \frac{C_r a}{V_c} \bar{\mathbf{B}} \Phi(s) \right]^{-1} F_{dn}(s) \\ \left\{ \mathbf{I} - K_t a (1 - e^{-sT_p}) \bar{A} \Phi(s) \cdot \left[ \mathbf{I} - s \frac{C_r a}{V_c} \bar{\mathbf{B}} \Phi(s) \right]^{-1} \right\} F_{dn}(s) &= \{0\} \end{aligned} \quad (5-21)$$

The stability of the system is analyzed in frequency domain ( $s=i\omega_c$ ) from the characteristic equation when the process is critically stable at chatter frequency ( $\omega_c$ ).

$$\left| \mathbf{I} - K_t a (1 - e^{-i\omega_c T_p}) \bar{\mathbf{A}} \Phi(i\omega_c) \cdot \left[ \mathbf{I} - i\omega_c \frac{C_r a}{V_c} \bar{\mathbf{B}} \Phi(i\omega_c) \right]^{-1} \right| = 0 \quad (5-22)$$

The stability of the system can be solved only iteratively due to speed dependent process damping term in Equation (5-22). First, the process damping term is neglected ( $C_r = 0$ ), and the characteristic equation is reduced to classical zero order stability problem as solved by Altintas and Budak [81]:

$$\begin{aligned} \left| \mathbf{I} - \Lambda \bar{\mathbf{A}} \Phi(i\omega_c) \right| = 0 &\leftarrow \Lambda = K_t a (1 - e^{-i\omega_c T_p}) \\ a_0 \Lambda^2 + a_1 \Lambda + 1 = 0 &\rightarrow \Lambda = \Lambda_R + i\Lambda_I, \kappa = \frac{\Lambda_I}{\Lambda_R} \end{aligned} \quad (5-23)$$

The critically stable axial depth of cut ( $a$ ) and tooth period ( $T_p$ ) are estimated as:

$$\tilde{a} = -\frac{2\pi\Lambda_R}{NK_t} \left[ 1 + \left( \frac{\Lambda_I}{\Lambda_R} \right)^2 \right], \tilde{T}_p = \frac{\varepsilon + 2k\pi}{\omega_c} \leftarrow \varepsilon = \pi - 2 \tan^{-1} \frac{\Lambda_I}{\Lambda_R} \quad (5-24)$$

The estimated values are used to assign numerical values to the process damping coefficient at the same chatter frequency ( $\omega_c$ ) as:

$$C_0 = \left[ \mathbf{I} - i\omega_c \frac{C_r \tilde{a}}{\tilde{V}} \bar{\mathbf{B}} \Phi(i\omega_c) \right]^{-1} \leftarrow \tilde{V}_c = \frac{\pi d}{N\tilde{T}_p} \quad (5-25)$$

where  $d$  is the diameter of the micro-end mill. The characteristic equation is updated with the constant process damping term having complex numbers ( $C_0$ ) as:

$$\left| \mathbf{I} - \Lambda \bar{\mathbf{A}} \Phi(i\omega_c) \cdot C_0 \right| = 0 \quad (5-26)$$

The eigenvalue solution (Equation (5-24)) is repeated until the depth of cut and tooth period converges to constant values with an acceptable tolerance, i.e.  $\tilde{a} \rightarrow a_{\text{lim}}; \tilde{T}_p \rightarrow T_p$ . The flowchart of solving the chatter stability for micro-milling is shown in Figure 5.9.

The spindle speed is evaluated as  $n(\text{rev}/\text{min}) = 60/(NT_p)$ . The effect of process damping is negligible and the solution converges within two – three iterations when the tooth passing frequency ( $\omega_T = 1/T_p$ ) is equal or not less than 5-6 times of chatter

frequency ( $\omega_c$ ). However, when the speed is low and the tooth passing frequency is less than 10-15 times of chatter frequency, the process damping becomes highly effective, and about 15-20 iterations may be needed for convergence. The strength of the process damping becomes highly dependent on the edge radius of the micro-end mills.

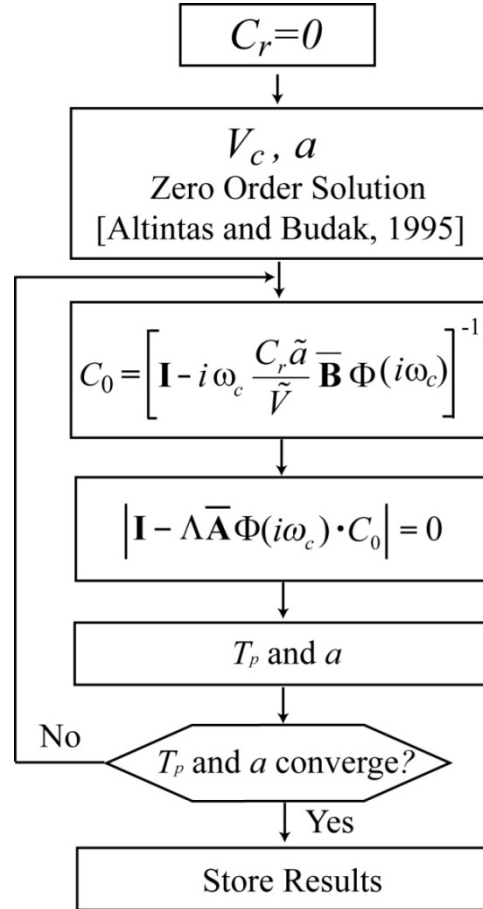


Figure 5.9 Flowchart of solving chatter stability in micro-milling.

## 5.5 Experimental validation for micro-milling chatter

The cutting tests have been conducted on a Micromachining Center equipped with 60,000 rev/min Fischer Precise spindle with ball bearings. The feed drives are powered by linear motors. A two fluted, Mitsubishi Materials MS2MS carbide micro-end mill with 600  $\mu\text{m}$  diameter, 1.2 mm flute length and 4  $\mu\text{m}$  edge radius is used in slot milling of AISI 1045 steel. The feed-rates were kept constant at  $c = 5 \mu\text{m}/\text{tooth}$ . The methods to measure the frequency response function of the micro-end mill and chatter frequencies in micro-milling

tests are summarized here.

### 5.5.1 Identification of FRF at micro-mill tip

Since the impact modal tests cannot be applied on the micro-mill to avoid its fracture, a piezo actuator has been designed to excite it up to 120 kHz frequency range similar to the instrumentation presented in [41][42]. The micro-end mill shank has 4 mm diameter with 16 mm overhang from the tool holder as shown in Figure 5.11.

The experimental setup to measure the FRF of micro-mill is shown in Figure 5.10. A 3 mm x 2 mm piezoelectric actuator (Physik Instrumente P-882) with 9 mm length is attached to the tool shank. The other side of the actuator is connected to a force sensor (Kistler 9211) which has a natural frequency of 200 kHz. The force sensor is glued to a fixture which is clamped on the X-Y stage of the micro-milling machine. The tool is moved towards the actuator by CNC until 20 N preload is generated on the tool shank. The piezoelectric actuator expands and contracts when a sinusoidal voltage is applied by a signal generator at a frequency range of 0.5 kHz to 120 kHz. While the harmonic excitation is applied only on the shank to avoid tool failure, the vibrations are measured both at the shank and flute tip by a laser Doppler vibrometer (CLV-2534).

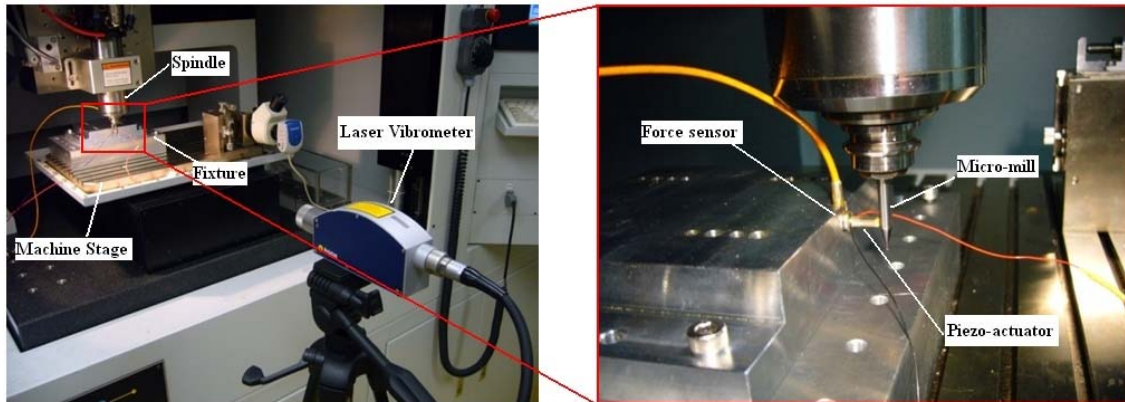


Figure 5.10 Experimental setup to measure the FRF of micro-mill.

The FRF at the flute tip ( $\Phi_{22}$ ) is indirectly identified as:

$$\Phi_{11} = \frac{x_1}{F_1}, \quad \Phi_{21} = \frac{x_2}{F_1} = \frac{x_1}{F_2} \rightarrow \Phi_{22} = \frac{x_2}{F_2} = \frac{\Phi_{21}^2}{\Phi_{11}} \quad (5-27)$$

The measured FRF and reconstructed FRF from four dominant modes at the tool tip

( $\Phi_{22}$ ) are shown in Figure 5.11. The tool is assumed to be symmetric in radial directions ( $\Phi_{22} = \Phi_{xx} = \Phi_{yy} = \Phi$ ) and cross frequency response is negligible ( $\Phi_{xy} = \Phi_{yx} = 0$ ) since the source of the dominant flexibilities are due to cylindrical tool holder and tool. The modes are between 3.8 to 106.6 KHz, and their estimated modal parameters are given in Table 5.3. The modal parameters are used in expressing the FRFs at the tool tip as:

$$\widehat{\Phi}(i\omega) = \sum_{l=1}^4 \frac{\omega_{nl}^2 / k_l}{\omega_{nl}^2 - \omega^2 + i2\zeta_l \omega_{nl} \omega} \quad (5-28)$$

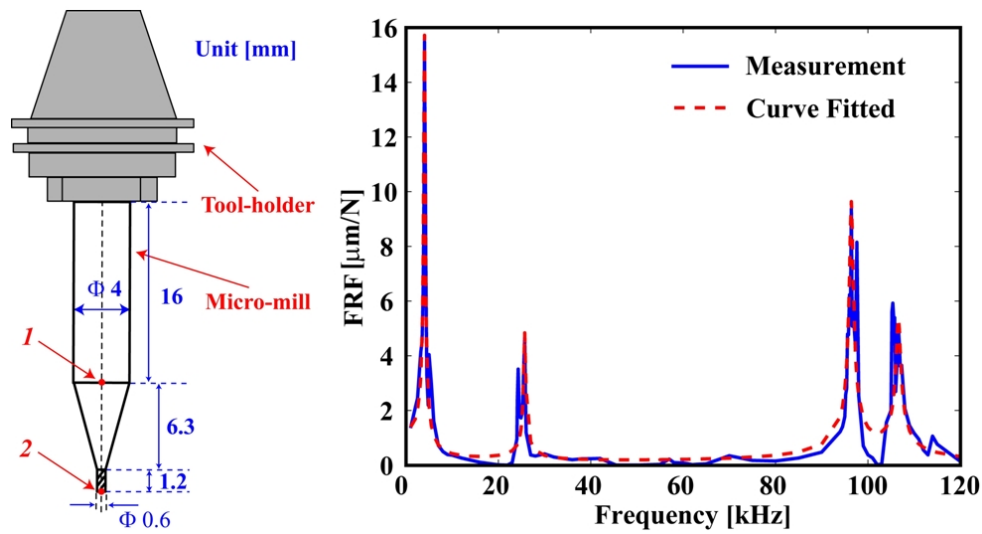


Figure 5.11 Measured and curve-fitted FRF of micro-mill at tool tip.

Table 5.3 Modal parameters of micro-mill.

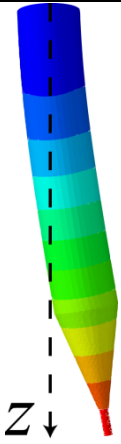
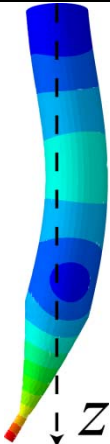
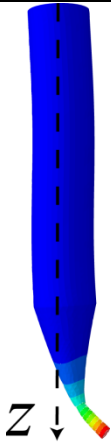
Mode	Natural Frequency [kHz]	Damping ratio	Stiffness [N/μm]	Mode Shape
1	3.8	3.62%	0.89	1 <sup>st</sup> Bending mode of shank
2	25.7	0.78%	13.7	2 <sup>nd</sup> Bending mode of shank
3	96.4	0.41%	13.0	1 <sup>st</sup> Bending mode of taper and flute
4	106.6	0.45%	22.1	2 <sup>nd</sup> Bending mode of flute

Experimental and FE modal analysis indicate the source of each mode as given in Table 5.3. Micro-end-mill's shank (3.8 kHz), which is attached to mechanical ATC 2-10-6 chuck, appears to have the highest flexibility followed by the first bending mode of the

fluted section (96.4 kHz).

FE method is also used to predict the natural frequencies and mode shapes of the micro-mill by Abaqus/Standard 6.8-3. Perfect cantilever constraint is applied at the shank end. A three-dimensional model of the tool is set up, and tetrahedron elements are used to mesh the tool. The density and the elastic modulus of the carbide used as micro-mill materials are  $14300 \text{ kg/m}^3$  and  $580 \text{ GPa}$ , respectively. The cutting flutes are approximated by a cylinder with the diameter equals to 90% of the nominal value of the tip diameter. The natural frequencies and mode shapes of the first four bending modes are shown in Table 5.4. The Z-axis represents the tool axial direction without deformation. FE results show that the first two modes come from the bending of the tool shank, the 3<sup>rd</sup> and 4<sup>th</sup> mode are the bending modes of the taper part and tool tip. The difference of the natural frequencies between the experimental measurement and the FE prediction shows that the boundary condition at the clamping point of the tool causes change of tool dynamics. The experimental measurement is able to identify tool-tip FRF considering the clamping condition and actual tool geometry.

Table 5.4 Natural frequencies and mode shapes of micro-mill from FE simulation.

Mode 1	Mode 2	Mode 3	Mode 4
$\omega_{n1} = 7.56 \text{ kHz}$	$\omega_{n2} = 41.03 \text{ kHz}$	$\omega_{n3} = 93.75 \text{ kHz}$	$\omega_{n4} = 120.89 \text{ kHz}$
			

### 5.5.2 Chatter stability tests

The experimental setup is shown in Figure 5.12. Since the dynamometer does not have sufficient bandwidth to detect chatter frequencies, a microphone (AKG C1000S) with a frequency bandwidth of 20 kHz and an acoustic emission (AE) sensor (Physical Acoustics NANO30) with a bandwidth of 750 kHz are used to measure the vibration signals during cutting tests. A National Instrument data acquisition card is used to collect sensor data at 200 kHz via CUTPRO software [69]. For the feed-rate of  $c = 5 \mu\text{m}/\text{tooth}$  and  $4 \mu\text{m}$  edge radius, the corresponding cutting force coefficients are evaluated for an average chip thickness of  $c_{ave} = (1/\pi) \int_0^\pi c \sin \phi d\phi = 3.183 \mu\text{m}$  from Table 5.1. The stability of the system was solved by including the chip size dependent nonlinearity in the cutting force coefficients [83], but the results did not change noticeably in this particular case. The process damping coefficients are given in Equation (5-16). The following coefficients are used in predicting the stability lobes:

$$\begin{cases} K_t = 4042 \text{ MPa} \\ K_r = 2814 \text{ MPa} \end{cases} \rightarrow k_r = K_r / K_t = 0.696$$

$$\begin{cases} C_{pt} = 1.872 \times 10^4 \text{ [N/m]} \\ C_{pr} = 2.136 \times 10^4 \text{ [N/m]} \end{cases} \rightarrow c_t = C_{pt} / C_{pr} = 0.877$$
(5-29)

The averaged directional matrices are evaluated for slot milling with two fluted micro-end mill as:

$$\bar{\mathbf{A}} = \frac{1}{\pi} \int_0^\pi \mathbf{A}(\phi) d\phi = \frac{1}{2} \begin{bmatrix} -k_r & -1 \\ 1 & -k_r \end{bmatrix} = \begin{bmatrix} -0.348 & -0.5 \\ 0.5 & -0.348 \end{bmatrix}$$

$$\bar{\mathbf{B}} = \frac{1}{\pi} \int_\pi^{2\pi} \mathbf{B}(\phi) d\phi = \frac{1}{2} \begin{bmatrix} -1 & -c_t \\ c_t & -1 \end{bmatrix} = \begin{bmatrix} -0.5 & -0.438 \\ 0.438 & -0.5 \end{bmatrix}$$
(5-30)

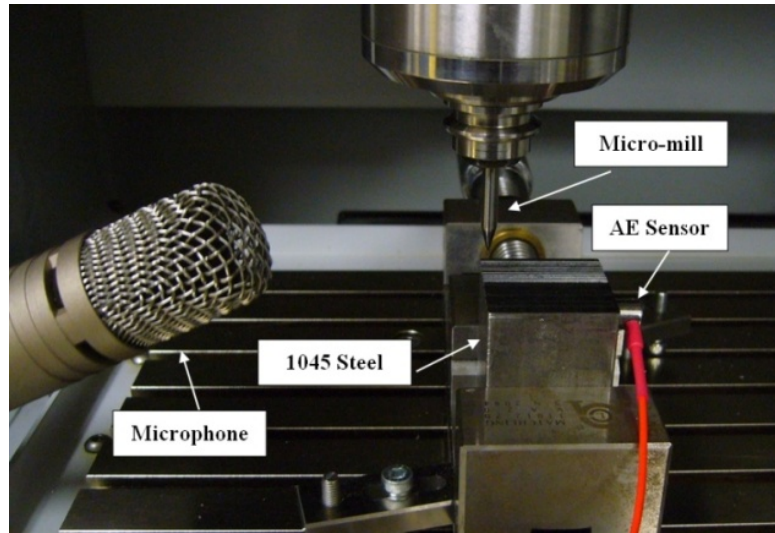


Figure 5.12 Experimental setup for micro-milling test.

The stability lobes are predicted for a speed range of [10,000-120,000] rev/min by considering all four vibration modes and process damping as shown in Figure 5.13. The first bending mode (3.8 kHz) of micro-mill shank dominates the lobes, while others are stiffer and damped out by the process at the operating speed range of the machine.

A series of micro-milling tests were performed to verify the proposed chatter stability model. The Fast Fourier Transform (FFT) of the collected data from microphone and AE sensor were used to detect the frequency of the vibrations. The predicted chatter stability diagram is compared against the experimental data in Figure 5.14. Sample spectrums of Microphone signals at the chatter ( $A: n = 45450 \text{ rev/min}, a = 30 \mu\text{m}$ ) and stable ( $B: n = 54,600 \text{ rev/min}, a = 50 \mu\text{m}$ ) conditions are shown in the Figure 5.15. AE sensor gave the similar results except it amplifies the signals beyond 7 kHz, which is above the chatter frequency, shown in Figure 5.16.

The microphone data gives the highest peak at  $\omega_c = 4264 \text{ Hz}$ , which is close to the first bending mode of the shank when the speed is 45450 rev/min. The corresponding spindle and tooth frequencies are  $\omega_s = 757.5 \text{ Hz}$  and  $\omega_t = 1515 \text{ Hz}$ , respectively. The other peaks are at the tooth passing frequency harmonics and also at  $\omega = \omega_c \pm l\omega_t$  which

indicates that the chatter occurs at  $\omega_c = 4264 Hz$ . The chatter frequency is higher than the natural frequency (3800 Hz) because of the added cutting stiffness and possibly increased spindle bearing stiffness at this speed.

The process is stable at spindle speed  $n = 54600 rev/min$  and depth of cut  $a = 50 \mu m$ . The spectrums of sound and AE sensors are dominated by the harmonics of spindle rotation (910 Hz) or tooth passing frequency (1820 Hz), which indicates forced vibration but stable micro-milling process.

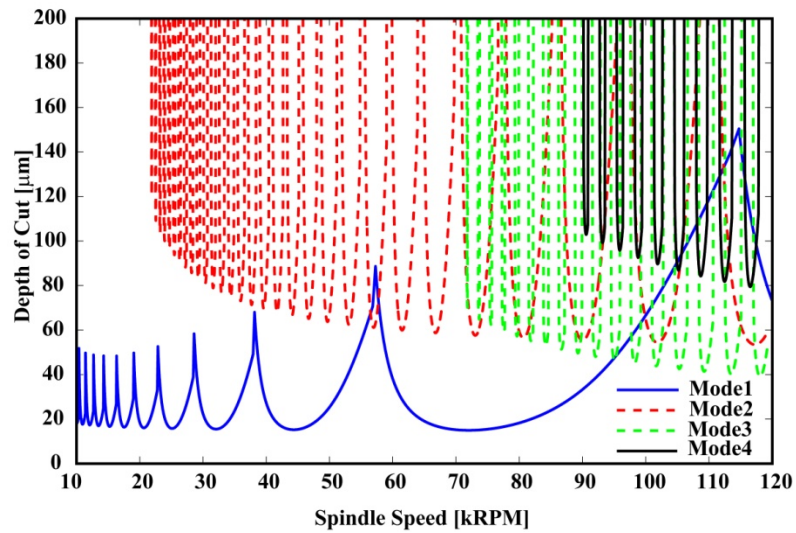


Figure 5.13 Predicted stability lobes with process damping effect. All four modes of micro-mill are considered.

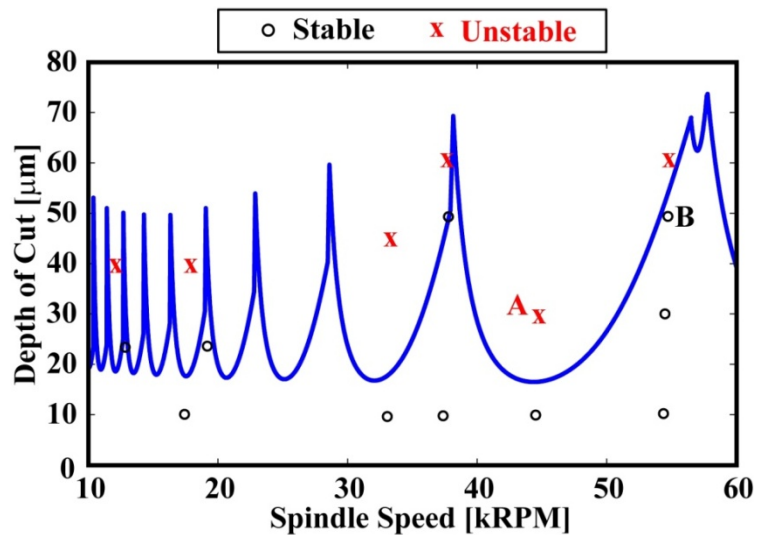
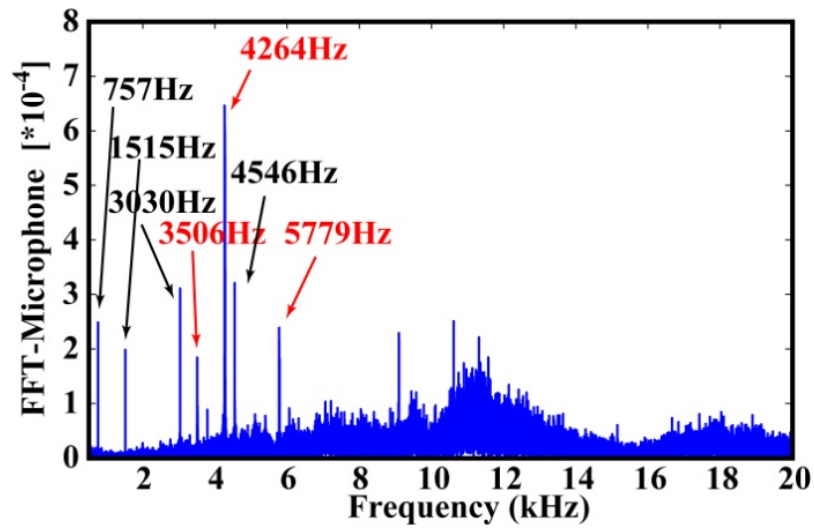
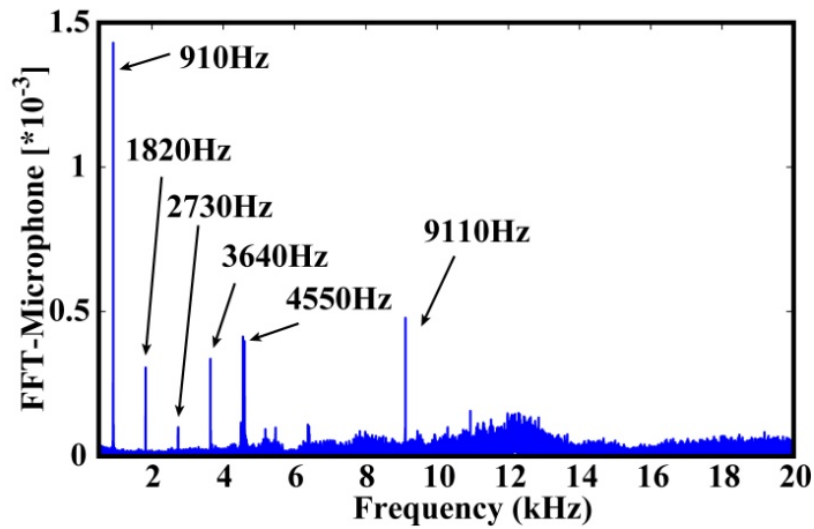


Figure 5.14 Predicted and experimentally evaluated chatter stability lobes.

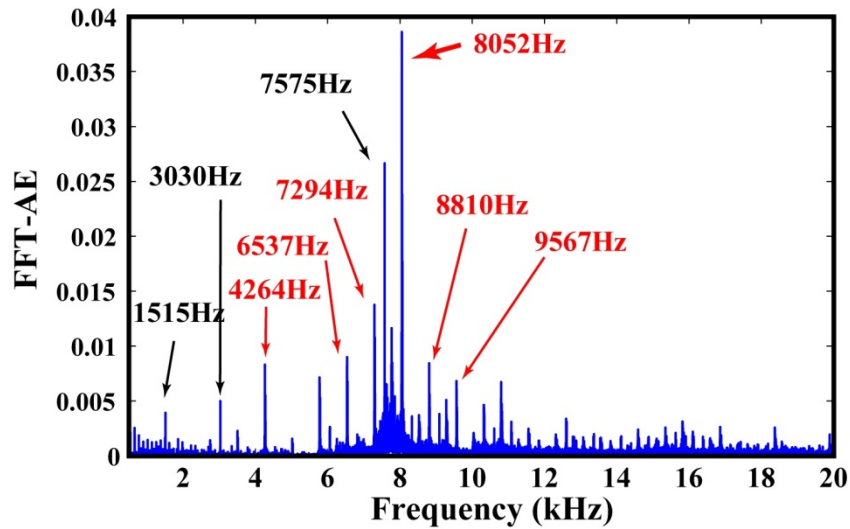


A) Chatter at  $n = 45450$  rev/min,  $a = 30 \mu m$ .

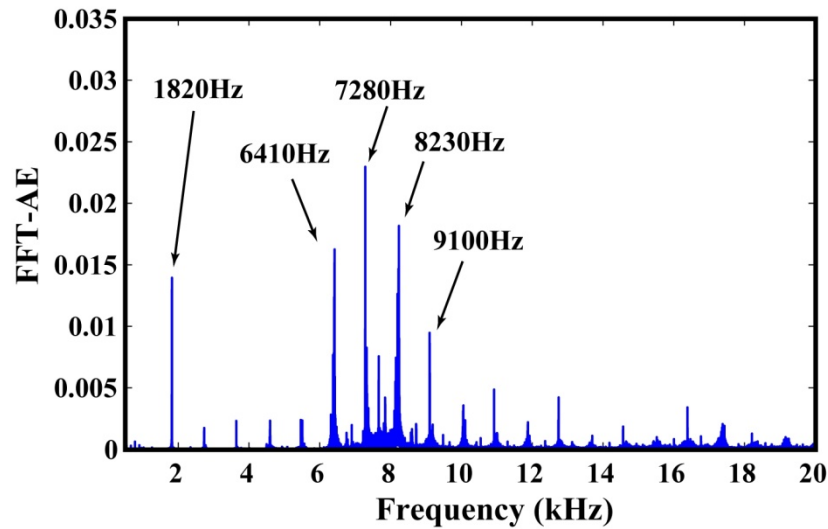


B) Stable at  $n = 54,600$  rev/min,  $a = 50 \mu m$ .

Figure 5.15 Microphone signals from chatter tests.



A) Chatter at  $n = 45450$  rev/min,  $a = 30\mu m$ .



B) Stable at  $n = 54,600$  rev/min,  $a = 50\mu m$ .

Figure 5.16 AE signals from chatter tests.

## 5.6 Conclusion

There are fundamental challenges in predicting the cutting forces and chatter stability in micro milling operations where the end mill has less than one mm diameter; the forces are less than ten Newtons; and the spindle speeds are over 40,000 rev/min. It is shown that the cutting force coefficients can be predicted from a slip-line model using material's constitutive models. The micro-milling forces, which have less than one Newton amplitude

and difficult to measure, can be predicted accurately. The contact between the worn or rounded clearance face of the tool and wavy surface finish can also be modeled by finite element method, and used as process damping coefficients in dynamic micro-milling models. The micro-mills have natural frequencies ranging from 2-4 kHz up to 100 kHz which are difficult to measure through standard impact tests. An alternative method, which uses high frequency piezo actuator and cross FRF tests, can be used to predict the direct FRFs at the tool tip. Once the FRF, cutting force and process damping coefficients are identified, the chatter stability of micro-milling operations can be reliably predicted in frequency domain.

This chapter presents a comprehensive modeling of micro milling processes by predicting forces and vibrations as a function of material properties, tool geometry, structural dynamics and operating conditions. The proposed modeling methods can guide the tool designer and micro-milling planner to select optimum cutting conditions in order to achieve desired surface finish and avoid tool-part damage.

# Chapter 6

## Conclusions and Future Research Directions

### 6.1 Conclusions

Cutting force prediction from material constitutive model with round tool edge effect, and chatter stability prediction considering high frequency modes of micro-tool and process damping effect address key problems in mechanics and dynamics modeling of micro-cutting process.

An analytical model based on slip-line field theory is developed to simulate plastic deformation of workpiece material including the strain hardening, strain-rate, and temperature effects on the flow stress. The stress distribution in the primary deformation zone is modeled based on the variation of shear velocity along the slip lines. Tangential and feed forces are predicted by integrating the normal and frictional stress along tool rake face and round edge. Finite element method is used to simulate the chip formation and predict the cutting force evolution of micro-cutting process. Arbitrary Lagrangian Eulerian adaptive meshing technique is applied to avoid the excessive deformation of workpiece elements around cutting edge. Distributions of strain, temperature and stress simulated between slip-line field and finite element models are compared to evaluate the predictive accuracy of both models. The simulation results are used to model the cutting force coefficients as non-linear functions of uncut chip thickness and tool edge radius. The micro-milling forces are predicted considering the radial tool run-out, actual tool tip trajectory and measurement distortions caused by dynamometer dynamics. Moreover, finite element model is used to simulate the chip formation in cutting workpiece material with multiple phases.

The experimental validation of cutting forces through micro-turning and micro-milling tests show that the developed models are able to predict the cutting forces which have less than one Newton amplitude. The predictions are obtained directly from the constitutive

property of workpiece material, hence no mechanistic cutting calibration is needed. Slip-line field model simulates the stress distribution and cutting forces for homogeneous material with high accuracy since the flow stress variation along tool-chip contact region is considered, while finite element model has less accuracy in predicting the feed force in orthogonal micro-cutting due to the limitation of defining tool-chip contact property in the commercial software. Finite element model has the advantage of simulating the chip formation for both homogeneous and heterogeneous workpiece material.

Dynamic micro-milling forces are modeled including the static force components from the rigid body motion of the cutting flute, forced vibrations due to the structural dynamics of micro-mill, and process damping due to the contact between tool edge and machined surface. Static cutting force coefficients are identified from slip-line field simulations. Piezo-actuator based shaker is developed to experimentally identify the structural dynamics at tool tip. Finite element simulations are conducted to identify the process damping coefficients by calculating the energy dissipation at the ploughing region with round tool edge. Chatter stability of micro-milling is solved using iterative method in frequency domain including the process damping effect. Microphone and acoustic emission sensors are used to experimentally validate the chatter stability model of micro-milling process.

The FRF measurement on micro-mill shows that the developed piezo-actuator system is able to measure the modal parameters up to 120 kHz which are difficult to obtain through standard impact tests. The identification of process damping coefficient from FE model includes the strain-hardening and temperature effects on flow stress of workpiece material in the ploughing region. Once the FRF, cutting force and process damping coefficients are identified, the chatter stability of micro-milling operations can be reliably predicted in frequency domain.

The thesis contributions are summarized as follows:

- The stress variation in the material deformation zone is considered in the slip-line field model of micro-cutting process, while the classic slip-line field theory only assumes a constant flow stress in the shear zone. The proposed model applies the

Johnson-Cook constitutive equation to simulate the distribution of strain, strain-rate and temperature in the primary deformation zone, and predicts both shearing and ploughing forces due to round tool edge effect.

- The predictive accuracy of cutting force from slip-line field and finite element models are evaluated by comparing the simulations with experimental results. It is shown that the slip-line model predicts both tangential and feed forces accurately, while finite element model underestimates the feed force, which is due to the underestimation of the friction stress in the commercial FE software systems. If FE systems allow the integration of cutting process specific friction field, they are also expected to give accurate prediction of cutting forces in feed direction, although at a significant computational cost.
- The cutting force coefficients are identified as functions of uncut chip thickness and tool edge radius. Nonlinearity of cutting force with respect to uncut chip thickness due to the round tool edge effect is included. The cutting force coefficients are obtained from the simulated force results, and no mechanistic calibration from cutting tests is needed. The micro-milling forces with sub-Newton magnitude are predicted directly from material constitutive model considering radial tool run-out, actual tool tip trajectory and dynamometer dynamics.
- The FRF of micro-mill in the frequency range of 0.5 - 120 kHz is identified directly from the developed piezo-actuator. The process damping coefficient in the ploughing region is identified using finite element simulations. High frequency modes of micro-mill and process damping effect are considered in obtaining the chatter stability lobe, which provides a guidance to select optimum cutting condition.

This thesis presents a complete chain of micro-milling force and stability prediction model based on material properties and physics of cutting in the literature.

## 6.2 Future research directions

The accuracy of cutting force prediction from slip-line field model depends on the Johnson-Cook parameters of workpiece material. However, the constitutive parameters may vary for the same type of material if different heat treatment methods are applied. Identification of constitutive parameters for specific workpiece material will improve the predictive accuracy of the slip-line field model.

Finite element model underestimates the feed force in orthogonal cutting due to the disadvantage of commercial FE software in modeling the tool-chip contact. More realistic modeling of the contact property including the flow stress variation in the secondary deformation zone could improve the cutting force prediction from FE model.

The process damping coefficient is identified from the finite element model. The simulation which needs to be conducted for each type of workpiece material and tool geometry is computationally expensive. Analytical model of tool indentation into the wavy surface finish could be developed to obtain the contact force coefficient from constitutive parameters of workpiece material.

The chatter tests conducted in this thesis use a ball bearing spindle with maximum rotating speed of 60,000 rpm, while the air-bearing spindle is also used in the industry with the rotating speed up to 200,000 rpm. The pressurized air film would change the dynamic boundary conditions of the spindle shaft at different operating conditions. Moreover, when the tool rotates with high spindle speed, the frequency response function varies due to the gyroscopic and centrifugal effects. Chatter stability modeling of micro-milling considering the cutting condition dependent dynamics caused by air bearing, gyroscopic and centrifugal effects will improve the accuracy of predicting stability lobe in high spindle speed.

# Bibliography

- [1] Y. Bang, K. Lee, S. Oh, 2005. 5-Axis micro milling machine for machining micro parts. *International Journal of Advanced Manufacturing Technology*, 25 (9–10), 888–894.
- [2] Altintas Y., 2012, *Manufacturing Automation*, Cambridge University Press.
- [3] W.Y. Bao, I.N. Tansel. Modeling micro-end-milling operations, 2000. Part1: analytical cutting force model. *International Journal of Machine Tools and Manufacture*, 40, 2155–2173
- [4] I.S. Kang, J.S. Kim, J.H. Kim, M.C. Kang, Y.W. Seo, 2007. A mechanistic model of cutting force in the micro end milling process. *Journal of Materials Processing Technology*, 187–188, 250–255
- [5] Bissacco G, Hansen HN, Slunsky J, 2008. Modelling the Cutting Edge Radius Size Effect for Force Prediction in Micro Milling. *Annals of the CIRP* 57(1), 113–116.
- [6] M. Malekian, S. Park, M. Jun, 2009. Modelling of dynamic micro-milling cutting forces. *International Journal of Machine Tools and Manufacture*, 49, 586–598
- [7] H.U. Lee, D.W. Cho, K.F. Ehmann, 2008. A mechanistic model of cutting forces in micro-end-milling with cutting-condition-independent cutting force coefficients. *ASME Journal of Manufacturing Science and Engineering*, 130 (3), 0311021–0311029
- [8] Martin B. G. Jun, Chanseo Goo, Mohammad Malekian, Simon Park, 2012. A New Mechanistic Approach for Micro End Milling Force Modeling. *ASME Journal of Manufacturing Science and Engineering*, 134 (1), 0110061–0110069.
- [9] Zaman, M. T., Kumar, A. S., Rahman, M., and Sreeram, S., 2006. A Three-Dimensional Analytical Cutting Force Model for Micro End Milling Operation, *International Journal of Machine Tools and Manufacturing*, 46(3-4), 353–366.
- [10] M.P. Vogler, R.E. DeVor, S.G. Kapoor, 2003. Microstructure-Level Force Prediction Model for Micro- Milling of Multi-Phase Materials. *Journal of Manufacturing Science and Engineering, Transactions of the ASME*, 125 (2), 202–209.
- [11] Johnson, W., Sowerby, R., Venter, R.D., 1982. *Plane-Strain Slip-Line Field for Metal Deformation Process*. Pergamon Press Ltd., Oxford, UK.

- [12] Merchant, M.E., 1945. Mechanics of the metal cutting process, II. Plasticity conditions in orthogonal cutting. *Journal of Applied Physics* 16, 318–324.
- [13] Lee, E.H., Shaffer, B.W., 1951. The theory of plasticity applied to a problem of machining. *Journal of Applied Mechanics* 18, 405–413.
- [14] Kudo, H., 1965. Some new slip-line solutions for two-dimensional steady-state machining. *International Journal of Mechanical Science* 7, 43–55.
- [15] Dewhurst, P., 1978. On the non-uniqueness of the machining process. *Proc. R. Soc. London, Ser. A* 360, 587–610.
- [16] Dewhurst, P., Collins, I.F., 1973. A matrix technique constructing slip-line field solutions to a class of plane strain plasticity problems. *International Journal for Numerical Methods in Engineering* 7, 357–378.
- [17] Childs, T., 1980. Elastic effects in metal cutting chip formation. *International Journal of Mechanical Sciences* 22, 457–466.
- [18] Palmer, W.B., Oxley, P.L.B. *Mechanics of Metal Cutting*. Proceedings of the Institution of Mechanical Engineers, Vol. 173, No. 24, 623-654.
- [19] Oxley, P.L.B., Welsh, M.J.M., 1963. Calculating the shear angle in orthogonal metal cutting from fundamental stress, strain, strain-rate properties of the work material. Proceedings of the Fourth International Machine Tool Design and Research Conference, Pergamon, Oxford, 73–86.
- [20] Roth, R. N., Oxley, P.L.B, 1972. A slip-line field analysis for orthogonal machining based on experimental flow fields. *International Journal of Mechanical Sciences*, Vol 14, 85-97.
- [21] Wang X, Jawahir IS, 2007. Recent Advances in Plasticity Applications in Metal Machining: Slip-Line Models for Machining with Rounded Cutting Edge Restricted Contact Grooved Tools. *International Journal of Machining and Machinability of Materials* 2(3): 347–360.
- [22] Adibi-Sedeh, A.H., Madhavan, V., Bahr, B., 2003. Extension of Oxley’s analysis of machining to use different material models. *Journal of Manufacturing Science and Engineering* 125, 656–666.
- [23] T. Shi, S. Ramalingam, Slip-line solution for orthogonal cutting with a chip breaker and flank wear. *International Journal of Mechanical Sciences*, 33 (9) (1991), 689–744.

- [24] Waldorf, D.J., DeVor, R.E., Kapoor, S.G., 1998. Slip-line field for ploughing during orthogonal cutting. *Journal of Manufacturing Science and Engineering* 120, 693–698.
- [25] Manjunathaiah, J., Endres, W.J., 2000. A new model and analysis of orthogonal machining with an edge-radiused tool. *Journal of Manufacturing Science and Engineering* 122, 384–390.
- [26] Ren, H., Altintas, Y., 2000. Mechanics of machining with chamfered tools. *Journal of Manufacturing Science and Engineering* 122, 650–659.
- [27] N Fang, IS Jawahir. 2002. An analytical predictive model and experimental validation for machining with grooved tools incorporating the effects of strains, strain-rates, and temperatures. *CIRP Annals-Manufacturing Technology* 51, 83–86.
- [28] Fang, N., 2003a. Slip-line modeling of machining with a rounded-edge tool – Part I: new model and theory. *Journal of the Mechanics and Physics of Solids* 51,715–742.
- [29] Fang, N., 2003b. Slip-line modeling of machining with a rounded-edge tool – Part II: analysis of the size effect and the shear strain-rate. *Journal of the Mechanics and Physics of Solids* 51, 743–762.
- [30] Wang, IS Jawahir, 2007. Recent advances in plasticity applications in metal machining: slip-line models for machining with rounded cutting edge restricted contact grooved tools. *International Journal of Machining and Machinability of Materials*, 2 (3), 347–360
- [31] T. Moriwaki, N. Sugimura, S. Luan, 1993. Combined stress material flow and heat analysis of orthogonal micromachining of copper. *Annals of CIRP*, 42, 75–78
- [32] K.W. Kim, W.Y. Lee, H.C. Sin, 1999. A finite-element analysis of machining with the tool edge considered, *Journal of Materials Processing Technology* 86, 45–55.
- [33] M.R. Movahhedy, Y. Altintas, M. Gadala, 2002. Numerical Analysis of Cutting with Chamfered and Blunt Tools. *Trans. ASME, J. Manufacturing Science and Engineering*, 124 (2), 178–188
- [34] Liu, K., Melkote, S., 2007. Finite element analysis of the influence of tool edge radius on size effect in orthogonal micro-cutting process. *International Journal of Mechanical Sciences* 49, 650–660.
- [35] Simoneau, A., Ng, E., Elbestawi, M.A., 2007. Grain size and orientation effects when microcutting AISI 1045 steel. *Annals of the CIRP* 56 (1), 57–60.

- [36] Vogler, M. P., DeVor, R. E., and Kapoor, S. G., 2004, On the Modeling and Analysis of Machining Performance in Micro-Endmilling, Part II: Cutting Force Prediction, *ASME Journal of Manufacturing Science and Engineering*, 126, 695-705.
- [37] K.S. Woon, M. Rahman, K.S. Neo, K. Liu, 2008. The effect of tool edge radius on the contact phenomenon of tool-based micromachining. *International Journal of Machine Tools and Manufacturing*, 48, 1395–1407.
- [38] Dhanorker, A. and Özel, T., 2008. Meso/micro scale milling for micro-manufacturing, *International Journal Mechatronics and Manufacturing Systems*, Vol. 1, No. 1, 23–42.
- [39] Childs, T.H.C., 2010. Surface energy, cutting edge radius and material flow stress size effects in continuous chip formation of metals. *CIRP Journal of Manufacturing Science and Technology* 3, 27–39.
- [40] Afazov, S.M., Ratchev, S.M., Segal, J., 2010. Modelling and simulation of micro-milling cutting forces. *Journal of Materials Processing Technology* 210, 2154–2162.
- [41] Filiz, S., Ozdoganlar, O.B., 2008, Microendmill Dynamics Including the Actual Fluted Geometry and Setup Errors. Part I: Model Development and Numerical Solution. *ASME Journal of Manufacturing Science and Engineering* 130, 031119–1-10.
- [42] Filiz, S., Ozdoganlar, O.B., 2008, Microendmill dynamics including the actual fluted geometry and setup errors. Part II: Model validation and application. *ASME Journal of Manufacturing Science and Engineering* 130/031120–1-13.
- [43] Mascardelli, B. A., Park, S. S., and Freiheit, T., 2008, Substructure Coupling of Microend Mills to Aid in the Suppression of Chatter, *ASME Journal of Manufacturing Science and Engineering* 130(1)/ 011010.
- [44] M.B.G. Jun, X. Liu, R.E. DeVor, S.G. Kapoor, 2006. Investigation of the dynamics of micro end milling, part 1: model development. *ASME Journal of Manufacturing Science and Engineering*, 128 (4), 893–900.
- [45] M.B.G. Jun, R.E. DeVor, S.G. Kapoor, 2006. Investigation of the dynamics of micro end milling, part 2: model validation and interpretation. *ASME Journal of Manufacturing Science and Engineering*, 128 (4), 901–912.

- [46] Wallace, P. W., Andrew, C., 1965, Machining Forces: Some Effects of Tool Vibration, *Journal of mechanical Engineering science*, vol.7, 152-162.
- [47] Sisson, T. R. and R.L. Kegg, 1969, An Explanation of Low Speed Chatter Effects, *Transactions of ASME, Journal of Engineering for Industry*, vol.91(4), 951-955.
- [48] Chiou, R. Y., Liang, S.Y., 1998, Chatter Stability of a Slender Cutting Tool in Turning with Wear Effect, *International Journal of Machine Tools and Manufacture*, vol. 38(4), 315-327.
- [49] Altintas, Y., Eynian, M., Onozuka, H., 2008, Identification of Dynamic Cutting Force Coefficients and Chatter Stability with Process Damping; In: *Annals of the CIRP, Manufacturing Technology*, vol.57 (1), 371-374.
- [50] Eynian, M., Altintas, Y., 2009, Chatter Stability of General Turning Operations with Process Damping, *ASME Journal of Manufacturing Science and Engineering* 131, 041005.
- [51] Eynian, M., Altintas, Y., 2010, Analytical Chatter Stability of Milling with Rotating Cutter Dynamics at Process Damping Speeds, *ASME Journal of Manufacturing Science and Engineering* 132, 021012.
- [52] Budak, E., Tunc, L. T., 2009, A New Method for Identification and Modeling of Process Damping in Machining, *ASME Journal of Manufacturing Science and Engineering* 131, 051019-1.
- [53] Rahnama, R., Sajjadi, M., S.S. Park,S.S., 2009, Suppression of Chatter in Micro Milling with Process Damping. *Journal of Materials Processing Technology*, vol.209, 5766–5776.
- [54] S.S. Park, R. Rahnama, 2010. Robust chatter stability in micro-milling operations. *CIRP Annals - Manufacturing Technology*, 59 (1), 391–394.
- [55] Y. Shi, F. Mahr, U. Wagner, E. Uhlmann, 2012, Chatter frequencies of micro milling processes: Influencing factors and online detection via piezo actuators. *International Journal of Machine Tools and Manufacture*, vol. 56, 10-16.
- [56] Afazov, S.M.,Ratchev,S.M., Segal, J., Popov, A.A., 2012, Chatter modelling in micro-milling by considering process nonlinearities, *International Journal of Machine Tools & Manufacture* 56, 28–38.
- [57] Armarego, E.J.A., Brown, R.H., 1969. *The Machining of Metals*. Prentice-Hall, Englewood

- Cliffs, NJ.
- [58] Green, A.P., 1954. On the use of hodographs in problems of plane plastic strain. *Journal of the Mechanics and Physics of Solids* 2, 73–80.
- [59] Zorev, N.N., 1963. Interrelationship between shear processes occurring along tool face and on shear plane in metal cutting. *Proceedings of International Research in Production Engineering Research Conference*, pp. 42–49.
- [60] Dewhurst, P., 1985. A general matrix operator for linear boundary value problems in slip-line field theory. *International Journal for Numerical Methods in Engineering* 21, 169–182.
- [61] Johnson, G.J., Cook, W.H., 1983. A constitutive model and data for metals subjected to large strains high strain rates and high temperatures. *Proceedings of the 7th International Symposium on Ballistics*, pp. 541–547.
- [62] Kushnir, V.S., 1982. *Thermo mechanical Approach in Metal Cutting* (in Russian). Irkutsk University Publ., Irkutsk.
- [63] Astakhov, V.P., 1998. *Metal Cutting Mechanics*. CRC Press, Boca Raton, FL.
- [64] Hill, R., 1954. The mechanics of machining: a new approach. *Journal of the Mechanics and Physics of Solids* 3, 47–53.
- [65] Coleman, T.F. and Y. Li. *Optimization toolbox user's guide*. Matlab Version 2007. The Mathworks Inc.
- [66] H. Chandrasekaran, R. M'Saoubi, H. Chazal, 2005. Modelling of material flow stress in chip formation process from orthogonal milling and split Hopkinson bar tests. *Machining Science and Technology*, 9, pp. 131–145.
- [67] Altintas Y., Engin S., 2001. Generalized Modeling of Mechanics and Dynamics of Milling Cutters. *Annals of the CIRP* 50(1), 25–30.
- [68] Montgomery D., Altintas Y., 1991. Mechanism of Cutting Force and Surface Generation in Dynamic Milling. *ASME Journal of Engineering for Industry* 113:160–168.
- [69] CUTPROTM Advanced Milling Process Simulation System, [www.malinc.com](http://www.malinc.com).
- [70] Altintas Y., Park S.S., 2004. Dynamic Compensation of Spindle-Integrated Force Sensors. *Annals of the CIRP* 53(1): 305–308.

- [71] Park, S.S., Malekian, M., 2009. Mechanistic modeling and accurate measurement of micro end milling forces. *Annals of the CIRP* 58 (1), 49–52.
- [72] ABAQUS, 2008. *Theory and Analysis User's Manual*. Version 6.8-3.
- [73] Nasr, M., Ng, E., Elbestawi, M.A., 2007. Modelling the effects of tool-edge radius on residual stresses when orthogonal cutting AISI 316L. *International Journal of Machine Tools and Manufacture* 47 (2), 401–411.
- [74] Filice, L., Micari, F., Rizzuti, S., Umbrello, D., 2007. A critical analysis on the friction modelling in orthogonal machining. *International Journal of Machine Tools and Manufacture* 47, 709–714.
- [75] Rech, J., Yen, Y.-C., Schaff, M.J., Hamdi, H., Altan, T., Bouzakis, K.D., 2005. Influence of cutting edge radius on the wear resistance of PM-HSS milling inserts. *Wear* 259, 1168–1176.
- [76] Vollertsen, F., Biermann, D., Hansen, H.N., Jawahir, I.S., Kuzman, K., 2009. Size effects in manufacturing of metallic components. *Annals of the CIRP* 58 (2), 566–587.
- [77] M. Umemoto, Z.G. Liu, S. Sugimoto, K. Tsuchiya, 2000. Tensile stress–strain analysis of single-structure steels. *Metallurgical and Materials Transactions A – Physical Metallurgy and Materials Science*, 31 (7) , 1785–1794.
- [78] Jaspers, S.P.F.C and Dautzenberg, J.H., 2002, Material behavior in conditions similar to metal cutting: flow stress in the primary shear zone, *Journal of Materials Processing Technology*, vol.122, 322-330.
- [79] A.Simoneau, E. Ng, M.A.Elbestawi, 2006, Modeling the effects of microstructure in metal cutting, *International Journal of Machine Tools and Manufacture*, vol. 47 (2), 368-375.
- [80] Tobias, S.A. and W. Fishwick, 1958, *A theory of regenerative chatter*, The engineer- London.
- [81] Altintas, Y., and Budak, E., 1995, Analytical Prediction of Stability Lobes in Milling, *CIRP Ann.*, vol.44/1, 357–362.
- [82] Ahmadi, K., Ismail, F., 2012. Stability lobes in milling including process damping and utilizing Multi-Frequency and Semi-Discretization Methods. *International Journal of Machine Tools & Manufacture*, vol.54-55, 46-54.
- [83] Landers, R.G., Ulsoy, A.G., 2008, Nonlinear feed effect in machining chatter analysis. *Journal*

- of Manufacturing Science and Engineering, vol. 130, 1–8.
- [84] Jin, X., Altintas, Y., 2011, Slip-line Field Model of Micro-cutting Process with Round Tool Edge Effect, *Journal of Materials Processing Technology*, vol.211, 339–355.
- [85] Altintas, Y., Jin, X., 2011, Mechanics of micro-milling with round edge tools, *Annals of CIRP*, 60/1, 77-80.
- [86] Jin, X., Altintas, Y., 2011. Prediction of Micro-milling Forces with Finite Element Method. *Journal of Materials Processing Technology*, vol.212, 542-552.
- [87] Jin, X., Altintas, Y., 2012. Chatter Stability Model of Micro-Milling with Process Damping. Submitted for Review.

# Appendix A: Determination of Slip-line Geometries

(1) The procedure to calculate the position of point U in Figure 3.3:

From Figure 3.3 line UA is perpendicular to line US, and the inclination angle of line UA with respect to the x-axis is  $\eta$ , therefore it is obtained that:

$$\begin{cases} \frac{A_y - U_y}{A_x - U_x} = \tan \eta \\ \frac{S_y - U_y}{S_x - U_x} = \tan\left(\frac{\pi}{2} + \eta\right) \end{cases} \quad (C1)$$

From (C1) it is calculated that the position of U is:

$$\begin{cases} U_x = \frac{A_x \tan \eta + S_x \cot \eta - A_y + S_y}{\tan \eta + \cot \eta} \\ U_y = \frac{A_y \cot \eta + S_y \tan \eta - A_x + S_x}{\tan \eta + \cot \eta} \end{cases} \quad (C2)$$

(2) The procedure to calculate the radius of EN in Figure 3.3:

Since line QE is tangential to EN at point E, the inclination angle of line QE with respect to the x-axis is  $-\phi_1$ , therefore the y-coordinate of point E is calculated as:

$$E_y = Q_y - l \sin \phi_1 \quad (C3)$$

From circular arc EN and the position of center  $O_1$ , it can be derived that:

$$\begin{cases} E_y = O_{1y} + R_1 \cos \phi_1 \\ N_y = O_{1y} + R_1 \cos \phi_3 \end{cases} \quad (C4)$$

From (C4) it is calculated that:

$$E_y - N_y = R_1 (\cos \phi_1 - \cos \phi_3) \quad (C5)$$

Combining (C3) and (C5), the radius of EN is calculated as:

$$R_1 = \frac{Q_y - N_y - l \sin \phi_1}{\cos \phi_1 - \cos \phi_3} \quad (C6)$$

# Appendix B: Derivation of Stress Distribution in Slip-line Field Model

(1) Derivation of shear flow stress along the radial direction ( $\partial k / \partial r$ ) in the convex region:

In Equations (3-27) and (3-28), the effective strain and strain-rate are expressed as:

$$\varepsilon = \frac{1}{\sqrt{3}} \cdot \frac{V_t}{V \cdot \sin \phi} \cdot \left( \frac{s - R_1}{l} \right)^q \quad (C7)$$

$$\dot{\varepsilon} = \frac{V_t \cdot q}{\sqrt{3}l} \cdot \left( \frac{s - R_1}{l} \right)^{q-1} \quad (C8)$$

The derivative of strain and strain-rate could be obtained that:

$$\frac{\partial \varepsilon}{\partial s} = \frac{1}{\sqrt{3}} \cdot \frac{V_t}{V \cdot \sin \phi} \cdot \frac{q(s - R_1)^{q-1}}{l^q} = \frac{q}{s - R_1} \varepsilon \quad (C9)$$

$$\frac{\partial \dot{\varepsilon}}{\partial s} = \frac{V_t \cdot q}{\sqrt{3}l} \cdot \frac{(q-1)(s - R_1)^{q-2}}{l^{q-1}} = \frac{q-1}{s - R_1} \dot{\varepsilon} \quad (C10)$$

Based on the Johnson-Cook model, the reference value of effective strain-rate is  $1.0 \text{ s}^{-1}$ , then from Equation (3-30), it could be obtained that:

$$\frac{\partial T}{\partial s} = \beta_T [A + B\varepsilon^n] \cdot [1 + C \cdot \ln \dot{\varepsilon}] \cdot \left[ 1 - \left( \frac{T - T_r}{T_m - T_r} \right)^m \right] \cdot \frac{1}{\rho \cdot c_s} \cdot \frac{\partial \varepsilon}{\partial s} \quad (C11)$$

The derivative of temperature could be expressed as the strain derivative. Based on Equation (3-15), the derivative of effective stress along the radial direction is:

$$\begin{aligned} \frac{\partial \sigma}{\partial s} = nB\varepsilon^{n-1} [1 + C \ln \dot{\varepsilon}] & \left[ 1 - \left( \frac{T - T_r}{T_m - T_r} \right)^m \right] \frac{\partial \varepsilon}{\partial s} + \frac{C}{\dot{\varepsilon}} [A + B\varepsilon^n] \left[ 1 - \left( \frac{T - T_r}{T_m - T_r} \right)^m \right] \frac{\partial \dot{\varepsilon}}{\partial s} \\ & + [A + B\varepsilon^n] [1 + C \ln \dot{\varepsilon}] \left[ -m \cdot \left( \frac{T - T_r}{T_m - T_r} \right)^{m-1} \cdot \frac{1}{T_m - T_r} \right] \frac{\partial T}{\partial s} \end{aligned} \quad (C12)$$

By replacing the elements  $\frac{\partial \varepsilon}{\partial s}$ ,  $\frac{\partial \dot{\varepsilon}}{\partial s}$  and  $\frac{\partial T}{\partial s}$  in Equation (C12) with (C9), (C10) and (C11), the derivative of shear flow stress is expressed as the function of strain, strain-rate and temperature:

$$\begin{aligned} \frac{\partial k}{\partial s} = & \frac{q}{\sqrt{3}(s-R_1)} \varepsilon \left[ 1 - \left( \frac{T-T_r}{T_m-T_r} \right)^m \right] \left[ nB\varepsilon^{n-1} [1+C \ln \dot{\varepsilon}] - \frac{\beta_T m}{\rho c_s} (A+B\varepsilon^n)^2 (1+C \ln \dot{\varepsilon})^2 \frac{(T-T_r)^{m-1}}{(T_m-T_r)^m} \right] \\ & + \frac{C(q-1)}{\sqrt{3}(s-R_1)} [A+B\varepsilon^n] \left[ 1 - \left( \frac{T-T_r}{T_m-T_r} \right)^m \right] \end{aligned} \quad (C13)$$

(2) Derivation of shear flow stress along the angular direction ( $\partial k / \partial \phi$ ) in the convex region:

From Equation (C7), it is obtained that:

$$\frac{\partial \varepsilon}{\partial \phi} = \frac{1}{\sqrt{3}} \cdot \frac{V_t}{V} \cdot \frac{(s-R_1)^q}{l^q} \cdot \left( -\frac{1}{\sin^2 \phi} \right) \cdot \cos \phi = -\frac{1}{\tan \phi} \varepsilon \quad (C14)$$

From Equation (C8), it is obtained that:

$$\frac{\partial \dot{\varepsilon}}{\partial \phi} = 0 \quad (C15)$$

From Equation (3-30):

$$\frac{\partial T}{\partial \phi} = \beta_T [A+B\varepsilon^n] \cdot [1+C \cdot \ln \dot{\varepsilon}] \cdot \left[ 1 - \left( \frac{T-T_r}{T_m-T_r} \right)^m \right] \cdot \frac{1}{\rho \cdot c_s} \cdot \frac{\partial \varepsilon}{\partial \phi} \quad (C16)$$

Based on Equation (3-15), the derivative of effective stress along angular direction is:

$$\begin{aligned} \frac{\partial \sigma}{\partial \phi} = & nB\varepsilon^{n-1} [1+C \ln \dot{\varepsilon}] \left[ 1 - \left( \frac{T-T_r}{T_m-T_r} \right)^m \right] \frac{\partial \varepsilon}{\partial \phi} + \frac{C}{\dot{\varepsilon}} [A+B\varepsilon^n] \left[ 1 - \left( \frac{T-T_r}{T_m-T_r} \right)^m \right] \frac{\partial \dot{\varepsilon}}{\partial \phi} \\ & + [A+B\varepsilon^n] [1+C \ln \dot{\varepsilon}] \left[ -m \cdot \left( \frac{T-T_r}{T_m-T_r} \right)^{m-1} \cdot \frac{1}{T_m-T_r} \right] \frac{\partial T}{\partial \phi} \end{aligned} \quad (C17)$$

By replacing the elements  $\frac{\partial \varepsilon}{\partial \phi}$ ,  $\frac{\partial \dot{\varepsilon}}{\partial \phi}$  and  $\frac{\partial T}{\partial \phi}$  in Equation (C17) with (C14), (C15)

and (C16), the derivative of shear flow stress is expressed as the function of strain, strain-rate and temperature:

$$\frac{\partial k}{\partial \phi} = \frac{\varepsilon}{\sqrt{3}} [1+C \ln \dot{\varepsilon}] \left[ 1 - \left( \frac{T-T_r}{T_m-T_r} \right)^m \right] \left( \frac{-1}{\tan \phi} \right) \left[ nB\varepsilon^{n-1} - \frac{\beta_T m}{\rho c_s} (A+B\varepsilon^n)^2 (1+C \ln \dot{\varepsilon}) \frac{(T-T_r)^{m-1}}{(T_m-T_r)^m} \right] \quad (C18)$$